12-2020

Selective Electrocatalytic Reduction of Co2 To CO with Iron Nheterocyclic Carbene Complexes and Near-Infrared Absorbance of Ruthenium(II) Photosensitizers Containing a Merocyanine π-Acceptor

Peter Andrew Catsoulis

SELECTIVE ELECTROCATALYTIC REDUCTION OF CO_2 TO CO WITH IRON N-HETEROCYCLIC CARBENE COMPLEXES AND NEAR-INFRARED ABSORBANCE OF RUTHENIUM(II) PHOTOSENSITIZERS CONTAINING A MEROCYANINE π-ACCEPTOR

A Thesis Presented

by

PETER ANDREW CATSOULIS

Submitted to the Office of Graduate Studies,
University of Massachusetts Boston,
in partial fulfillment of the requirements for the degree of

MASTER OF SCIENCE

December 2020

Chemistry Program

SELECTIVE ELECTROCATALYTIC REDUCTION OF CO_2 TO CO WITH IRON N-HETEROCYCLIC CARBENE COMPLEXES AND NEAR-INFRARED ABSORBANCE OF RUTHENIUM(II) PHOTOSENSITIZERS CONTAINING A MEROCYANINE π-ACCEPTOR

A Thesis Presented

by

PETER ANDREW CATSOULIS

Approved as to style and content by:

_____
Jonathan Rochford, Assistant Professor
Chairperson of Committee

_____
Michelle Foster, Associate Professor
Member

_____
Jason Evans, Associate Professor
Member

_____
Jonathan Rochford, Co Graduate Program Director
Chemistry Program

_____
Jason Evans, Co Graduate Program Director
Chemistry Program

_____
Michelle Foster, Chair
Department of Chemistry

ACKNOWLEDGEMENTS

While this thesis was written by me, I could not have achieved this accomplishment without the support of several individuals.

First and foremost, I would like to thank Dr. Jonathan Rochford for giving me the opportunity to attend graduate school. Through him I was able to not only prove myself as someone capable of a graduate degree but learn the various ins and outs of synthesizing and studying inorganic complexes capable of a variety of photochemical and catalytic applications. The time in the lab and in class has greatly improved my ability to work independently and has given me the tools to design and conduct my own research. For that I cannot thank you enough.

Additionally, I would like to thank my committee members Dr. Michelle Foster and Dr. Jason Evans for their insight and assistance along the way. Dr. Foster's door was always open for me to discuss and help understand the fundamentals of spectroscopy. Dr. Evans gave me the opportunity to characterize my inorganic complexes on the high resolution mass spectrometer and provided excellent help working towards understanding my data.

Thank you to all the graduate students and undergraduates who I have had the chance to work with. Fellow graduate students Tue Ngo, Meaghan McKinnon, Gerald Gilligan, Raymond Borg, and Alana Murphy promoted a great work environment and fostered discussion between projects. Andrew Gnann and Steven Couture have also been excellent

fellow graduate students and friends and deserve thanks for the time I have spent getting to know them and the support they have given me. And thank you to Siti Aishah Abdul Razak, Matthew Tracy and Christopher Ghastin who worked under me and often helped me keep up with deadlines on all of my lab work.

Lastly, I would like to thank the administrative staff at UMB who allowed me to focus more on research rather than on paperwork and finances. And of course, thank you to my family and close friends who encouraged and supported me throughout this entire program.

ABSTRACT

SELECTIVE ELECTROCATALYTIC REDUCTION OF CO_2 TO CO WITH IRON N-HETEROCYCLIC CARBENE COMPLEXES AND NEAR-INFRARED ABSORBANCE OF RUTHENIUM(II) PHOTOSENSITIZERS CONTAINING A MEROCYANINE π-ACCEPTOR

December 2020

Peter A. Catsoulis, B.S., Rutgers University Newark
M.S., University of Massachusetts Boston

Directed by Professor Jonathan Rochford

The catalytic proton-coupled reduction of carbon dioxide into C-1 or "common engine" liquid fuels is currently a highly desirable and green approach to removing anthropogenic CO_2 from the atmosphere. The most common approach to this is through electrocatalytic homogeneous reductions utilizing inorganic complexes as catalysts. Current research has moved towards the use of first-row transition metals in catalysts due to their high natural

abundances and cheap cost. Iron porphyrin complexes have been vastly studied due to their high product selectivity and turnover frequencies. However, these complexes exhibit short lived activity because of competing reactions in their catalytic cycles, rendering them inactive. This project seeks to improve on existing iron CO_2 reduction catalysts by constructing them with novel tridentate N-heterocyclic carbene ligands. The possibility exists that the strongly σ-donating and π-accepting character of the NHC functional group will drastically lower the thermodynamic barrier associated with carbon CO dissociation via the trans-effect, enhancing the number of catalytic turnovers capable under electrochemical conditions for Fe-based catalysts. A class of these catalysts will be synthesized and studied extensively through infrared spectroscopy, UV-vis spectroscopy, electrochemistry and electrocatalysis to test this hypothesis and attempt to tune it to maximize catalytic efficiency.

The development of transition metal complexes with a strong visible to near infrared (vis-NIR) absorption has been a long-term goal among inorganic chemists for their potential applications as photosensitizers and medical imaging contrast agents. The electronic and photophysical properties for a series of ruthenium(II) photosensitizers is here presented where a series of five π-accepting ligands based upon a 5-(vinyl-cyanine)-8-oxyquinolate scaffold have been investigated. A combination of computational, UV-Vis-NIR absorption, phosphorescence emission and cyclic voltammetry studies are used to assess the influence of these ligands on complex electronic and photophysical properties and to assess their potential as vis-NIR photoacoustic contrast agents.

TABLE OF CONTENTS

LIST OF TABLES

LIST OF SCHEMES

LIST OF FIGURES

LIST OF ABBREVIATIONS

LIST OF ABBREVIATIONS

η	Overpotential
BIN	benzoindoline
Bpy	2,2’-bipyridine
C-1	Common Engine Fuel
CF_3	Trifluoromethyl
CH_3	Methyl
CH_3OH	Methanol
Cl	Chloro
CO	Carbon Monoxide
CO_2	Carbon Dioxide
CV	Cyclic Voltammetry
DFT	Density Functional Theory
ESI-MS	Electrospay Ionization Mass Spectrometry
Fe	Iron
FE	Faradaic Efficiency
FT-IR	Fourier Transform Infrared Spectroscopy
HCO_2H	Formic Acid
HOMO	Highest Occupied Molecular Orbital
IND	indoline
IR-SEC	Infrared Spectroelectrochemisty

K_Q	Binding Constant
LUMO	Lowest Unocupied Molecular Orbital
MLCT	Metal-to-ligand Charge Transfer
MLLCT	Metal-ligand-to-ligand Charge Transfer
$N(CH_3)_2$	Dimethylamino
NCN	1,3-bis(6-phenylpyridin-2-yl)-benzo[d]imidazol-3-ium-2-ide
NHC	N-heterocyclic Carbene
NIL	Non-innocent Ligand
NIR	Near Infrared
NMR	Nuclear Magnetic Resonance Spectroscopy
NO_2	Nitro
OCH_3	Methoxy
P-PY	para pyridine
P-QN	para quinoline
PCET	Proton-coupled Electron Transfer
PCET-BC	Proton-coupled Electron Transfer Bond Cleavage Reaction
Qpy	quaterpyridine
SCE	Standard Calomel Electrode
SHE	Standard Hydrogen Electrode
TDDFT	Time Dependent Density Functional Theory
TOF	Turnover Frequency
TON	Turnover Number

TPP	Tetraphenylporphyrin
UV-vis	Ultraviolet-visible Spectrum

CHAPTER 1

SELECTIVE ELECTROCATALYTIC REDUCTION OF CO_2 TO CO WITH IRON N-HETEROCYCLIC CARBENE COMPLEXES

1.1 Background and Motivation

The increase in atmospheric carbon dioxide (CO_2) concentration above that of 400 ppm due to anthropogenic emissions has generated scientific concern as this increase is a primary driving force of climate change.[1] To reduce the concentration of atmospheric CO_2 a variety of approaches have been studied to capture or repurpose CO_2. A prominent part of this research is the proton-coupled reduction of CO_2 to generate C-1 liquid fuels, such as methanol (CH_3OH) and formic acid (HCO_2H), or precursors to liquid fuels, such as carbon monoxide (CO).[2,3] Currently, CO is prepared on an industrial scale using the Boudouard disproportionation of CO_2 over "coke" at 800 °C [4], or the steam reforming of low molecular weight hydrocarbons at ~1000 °C into synthesis gas (H_2:CO, 3:1).[5] As a component of synthesis gas, CO is an important raw material for the production of long-chain hydrocarbons (C_nH_{2n+2}, n = 10–20) via the Fischer-Tropsch process.[6]

The one-electron reduction of free CO_2 to generate the CO_2 radical anion, $CO_2^{\bullet-}$ is a thermodynamically demanding reaction, which occurs at a potential of -1.90 V vs. the standard hydrogen electrode (SHE) in water at pH 7. The demanding thermodynamic requirements of this reaction are due, primarily, to the large reorganization energy associated the linear to bent geometry transformation of reactant to product, respectively.[7] However, through the application of bio-inspired proton-coupled electron transfer (PCET) catalysis, the thermodynamic requirements for CO_2 reduction can be reduced significantly. For example, utilizing PCET, CO_2 can be reduced by two-electrons to generate CO and one equivalent of H_2O at just -0.52V vs SHE. To illustrate the diversity and proton dependency of CO_2 reduction half-reactions, a summary of aqueous equilibrium potentials is provided in Table 1.1.

Table 1.1. Equilibrium Potentials for Various CO_2 Reduction Reactions vs SHE[a]

$CO_{2(g)} + e^- \rightleftharpoons CO_2^{\cdot-}{}_{aq}$	-1.99V[b]	(1)
$CO_{2(aq)} + e^- \rightleftharpoons CO_2^{\cdot-}{}_{(aq)}$	-1.90V	(2)
$CO_{2(g)} + 2H^+_{(aq)} + 2e^- \rightleftharpoons HCO_2H_{(aq)}$	-0.61V	(3)
$CO_{2(g)} + 2H^+_{(aq)} + 2e^- \rightleftharpoons CO_{(g)} + H_2O_{(l)}$	-0.52V	(4)
$3CO_{2(g)} + H_2O_{(l)} + 2e^- \rightleftharpoons CO_{(g)} + 2HCO_3^-{}_{(aq)}$	-0.56V	(5)
$CO_{2(g)} + 4H^+_{(aq)} + 4e^- \rightleftharpoons H_2C(OH)_{2(aq)} + H_2O_{(l)}$	-0.49V[c]	(6)

$$CO_{2(g)} + 6H^{+}_{(aq)} + 6e^{-} \rightleftharpoons CH_3OH_{(aq)} + H_2O_{(l)} \qquad \text{-0.38V} \qquad (7)$$

$$CO_{2(g)} + 8H^{+}_{(aq)} + 8e^{-} \rightleftharpoons CH_{4(g)} + 2H_2O_{(l)} \qquad \text{-0.24V} \qquad (8)$$

[a]Standard potentials were taken from or calculated using thermodynamic data tabulated by Matsubara et Al.[8] Conditions: pH 7, 25 °C, 1 atm of gases (g), 1 M solutes (aq), in water as a solvent (l). [b]Calculated using the Nernst equation, with solubility data.[8] [c]Formaldehyde exists in the hydrated form (i.e., the diol).[8]

While the electrocatalytic proton-coupled reduction of CO_2 represents a promising approach,[9-11] efficiency and selectivity are not easily controlled due to the many competing reaction pathways.[12,13] One approach to address the efficiency and selectivity for CO_2 reduction is to employ a homogeneous redox catalyst to lower kinetic barriers and favor a designated pathway for improved selectivity.[14,15] Such catalysts are characterized by their overpotential (η), turnover frequency (TOF), turnover number (TON) and Faradaic efficiency (FE), each of which are defined below.

Catalyst overpotential, η, is defined as the difference between the applied catalytic potential at an electrode and the equilibrium potential ($E_{CO_2/CO}$) for the electrochemical reaction of interest. In the case of a homogeneous catalyst, to standardize overpotentials for ease of comparison, it has been recommended to use the half-wave potential of the observed catalytic wave ($E_{cat/2}$) as the applied electrocatalytic potential[16]

$$\eta = \left| E_{CO_2/CO} - E_{cat/2} \right| \qquad (9)$$

The turnover number (TON) of a catalyst defines the number catalytic cycles completed under specific conditions and thus defines a catalyst's stability. As a function of substrate and catalyst concentration, the amount of product formed will often taper off asymptotically with time. The repeatability of this behavior can suggest stability of a catalyst (with decreased activity then attributable to substrate consumption) while a decrease in reproducible behavior upon replenishing substrate implies catalyst degeneration. Quantitatively the TON is defined by Eq. 10.

$$\mathrm{TON} = \frac{\text{moles desired product formed}}{\text{moles catalyst}} \tag{10}$$

A catalyst's TOF is the rate at which a catalyst completes a turnover of its cycle and generates a desired product from a substrate, i.e. TON per unit time. The TOF value is often dictated by the *rate-determining step* (rds) of the catalytic cycle. TOF is traditionally determined using controlled potential electrolysis combined with, for example, gas chromatography quantification of CO production in the electrochemical cell headspace over a specified time period. A complimentary approach is to determine the TOF of an electrocatalyst directly from a simply time-dependent linear sweep voltammetry experiment using Eq. 11,

$$\mathrm{TOF} = 0.1992\left(\frac{\mathrm{F}\upsilon}{\mathrm{RT}}\right)\left(\frac{n_{\mathrm{p}}^3}{n_{\mathrm{cat}}^2}\right)\left(\frac{i_{\mathrm{cat}}}{i_{\mathrm{p}}}\right)^2 \tag{11}$$

where F is Faraday's constant (F = 96,485 C mol^{-1}), υ (V s^{-1}) is the scan rate, R is the gas constant (8.314 J K^{-1} mol^{-1}), T (K) is the temperature, n_{cat} is the number of electrons required to complete a single catalytic turnover (two-electrons for Eqs. 4 and 5), n_{p} is the number of

electrons involved in the stoichiometric noncatalytic Faradaic response to activate the precatalyst, i_{cat} is the peak catalytic current, and i_p is the non-catalytic Faradaic current response of the reference pre-catalyst reduction wave, often recorded under an inert atmosphere in the absence of CO_2 substrate.[17,18] When studied under optimal steady-state conditions – zero-order with respect to $[H^+]$ and only $[CO_2]$ is rate-limiting; where i_{cat} has reached its maximum obtainable value, typically identified by a characteristic S-shaped current response in cyclic voltammetry - the turnover frequency is defined as TOF_{max} from which the intrinsic rate constant of the catalyst (k_{cat}) can be extracted using Eq. 12.

$$\mathrm{TOF}_{\max} = k_{\mathrm{cat}}[\mathrm{CO}_2] \qquad (12)$$

Ideally, an efficient catalyst will exhibit a low overpotential and a high turnover frequency. Electrocatalysts should also be tested to determine the total number of catalytic turnovers prior to ceasing catalytic activity within a closed cell saturated with substrate (CO_2).

Lastly, faradaic efficiency (FE), often reported as a percentage, is defined as the percent of charge transferred to a catalyst in solution that facilitates a catalyst turnover. During a typical controlled potential electrolysis experiment, the faradaic efficiency of a catalyst is calculated by determining the stoichiometric ratio of 'moles of catalyst vs moles of electrons'. This calculation uses the recorded 'Coulomb count' to determine the moles of electrons transferred at the working electrode. Using the known Faraday unit of charge (F = 96,485 C mol^{-1}) the number of moles of electrons, n, transferred at the working electrode are easily calculated using Eq. 13.

$$n = \frac{\text{Coulomb count}}{F} \quad (13)$$

Subsequently, the %FE is calculated using Eq. 14

$$\%\text{FE} = \frac{\text{moles desired product formed}}{\text{n}_{cat}\text{ x moles electrons } (n)}\text{ x } 100 \quad (14)$$

Where, again, n_{cat} is the stoichiometric coefficient of electrons required to complete a single catalytic turnover. The greater the current associated with side reactions the greater faradaic loss is observed. An efficient catalyst should exhibit a high faradaic efficiency under optimized reaction conditions.

Homogeneous complexes containing a variety of transition metals including chromium (Cr), manganese (Mn), iron (Fe), cobalt (Co), rhenium (Re), ruthenium (Ru) and iridium (Ir) have been studied for electrocatalytic CO_2 reduction.[19] In more recent years, the use of first-row transition metals has been increasingly studied due to their large natural abundance.[20] Of these metals, Fe has garnered significant interest, inspired by its biological role of binding and transporting dioxygen (O_2) and CO_2 in blood cells.[21] Pioneered by Savéant and co-workers, who studied the tetraphenylporphyrin Fe(III) chloride pre-catalyst [Fe(TPP)Cl] in depth,[22-26] it was shown that under neutral conditions, these complexes behaved poorly but upon the addition of a Lewis or Brønsted acid, their catalytic properties improved dramatically. An established catalytic cycle using the [Fe(TPP)Cl] pre-catalyst is provided below (Scheme 1.1):

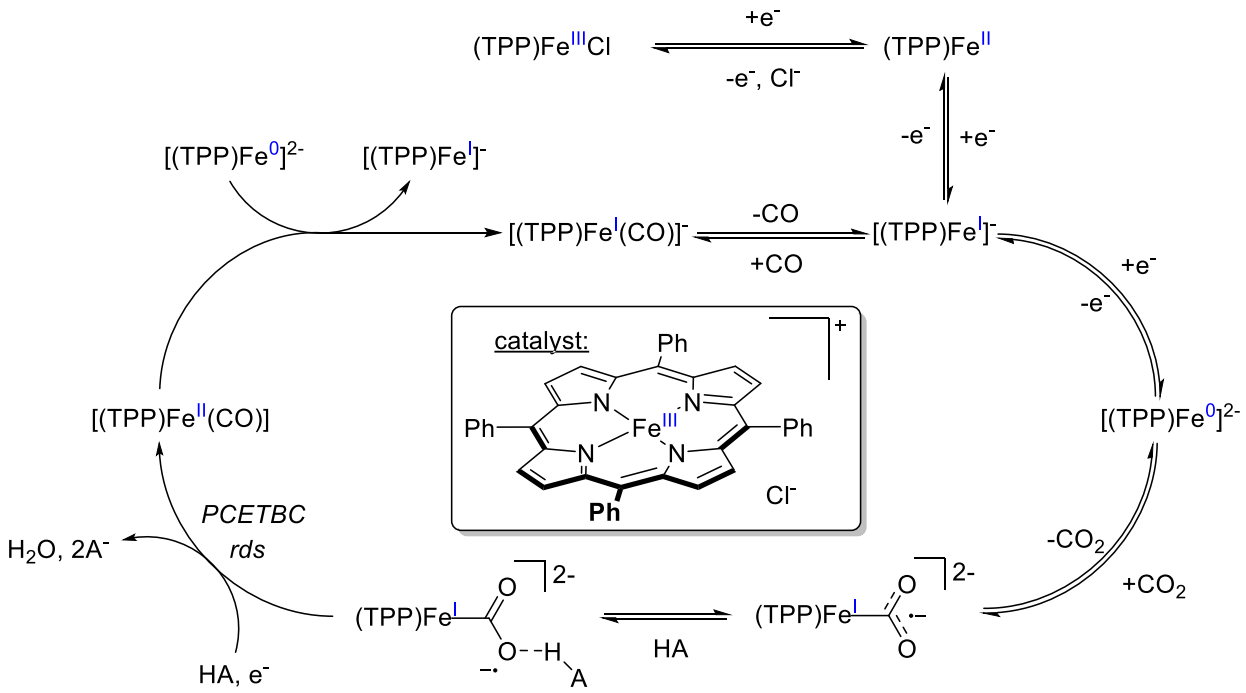

Scheme 1.1. Mechanism of CO_2 reduction using (TPP)Fe^{III}Cl in the presence of Brønsted Acids as reported by Savéant and co-workers.[24]

This catalytic cycle illustrates that an active Fe(0) porphyrin catalyst is generated in-situ following three sequential one-electron reduction events from the Fe(III) precatalyst. CO_2 binding then occurs at the metal center generating an Fe(II) metallocarboxylate with an overall charge of 2^-. In the presence of a Brønsted acid, a species in which one equivalent of acid forms a hydrogen-bond to one side of the metallocarboxylate CO_2 ligand. This intermediate is not fully protonated but remains hydrogen-bonded with the acid.[27] Next, an Fe(II) carbonyl complex, and its associated H_2O and conjugate base (A^-) by-products, are generated via a concerted proton-coupled electron transfer bond cleavage reaction (PCET-BC). This step has been established as the rate determining step, supported by

electrochemical kinetic analysis compared against several proposed kinetic pathways.[27] Lastly a comproportionation reaction with a second equivalent of activated Fe(0) catalyst generates an Fe(I) carbonyl from which the desired CO product dissociates. It is important to mention that the [Fe^{I}(TPP)(CO)] intermediate is in equilibrium with the active catalyst and as a result, CO concentration may compete with catalyst regeneration. Additionally, a related catalytic pathway was proposed by Savéant for [Fe(TPP)Cl] precatalysts with *o*-hydroxyl groups in the second coordination sphere[28], which was then later supported by experimental and computational data.[29]

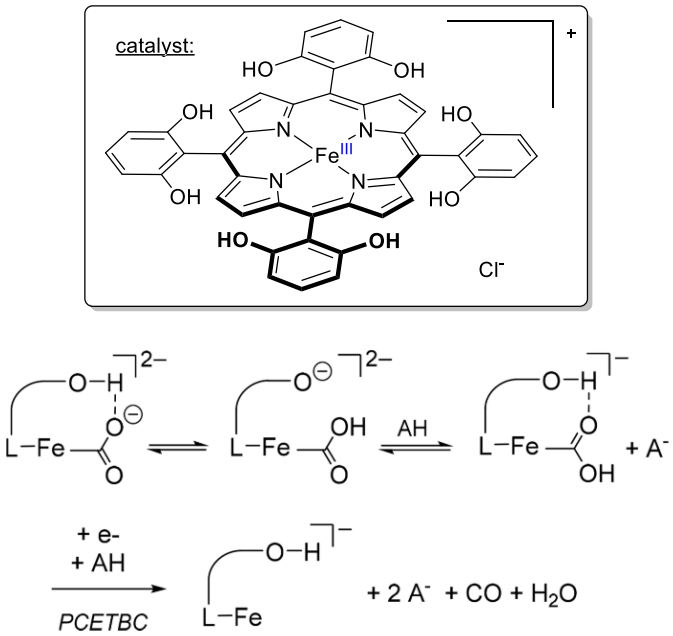

Scheme 1.2. Mechanism of CO_2 reduction with (TDHPP)Fe^{III}Cl by Savéant et al.[29]

In more recent literature, Robert et al. have reported an Fe(II) quaterpyridine (qpy) pre-catalyst system as an alternative to the porphyrin macrocycle.[30] The Fe-based $[Fe(qpy)]^{2+}$ pre-

catalyst exhibits a small overpotential (240 mV) and a faradaic efficiency of ≈ 70%. The remaining 30% is contributed to a side reaction that is discussed in more depth below in Scheme 1.3.

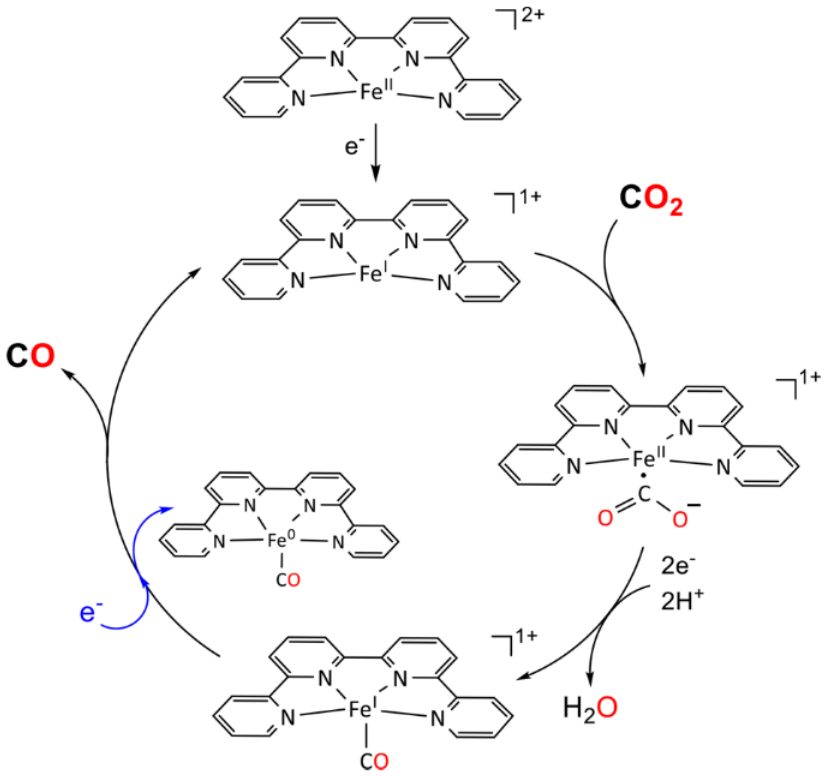

Scheme 1.3. Mechanism of CO_2 reduction by the $[Fe^{II}(qpy)]^{2+}$ catalyst reported by Robert et al.[30]

Robert's Fe(II) precatalyst undergoes an initial one-electron reduction to generate the active Fe(I) species. Addition of CO_2 generates the metallocarboxylate radical species $[Fe^{II}(qpy)(CO)^{\cdot -}]^{+}$ which, through a currently undetermined pathway, acquires two-protons and two-electrons to generate the Fe(I) carbonyl species $[Fe^{I}(qpy)(CO)]^{+}$ and one equivalent of water. The cycle closes by the dissociation of CO from $[Fe^{I}(qpy)(CO)]^{+}$ to regenerate the active

catalyst. The possibility does exist however, that upon generation of $[Fe^{I}(qpy)\ (CO)]^{+}$, that a one-electron reduction may occur at a sufficiently negative potential, generating the neutral $[Fe^{0}(qpy)\ (CO)]$ species, which is stable and catalytically inactive.

Fe porphyrins have exhibited some of the highest efficiencies in electrocatalytic CO_2 reduction, achieving high product selectivities (%Fe ~ 100% for CO production) and TOF's of 3.2×10^{4} to 1.6×10^{6} s^{-1}. The $[Fe^{II}(qpy)]^{2+}$ complex however, exhibited only moderate TOF's and TON's because of the competing reaction generating inactive $[Fe^{0}(qpy)(CO)]$. Thus, beyond porphyrin based Fe catalysts for CO_2 reduction, it still remains a challenge to overcome the thermodynamic barrier to Fe–CO bond cleavage to promote efficiency CO evolution. The following research plan details the proposed used of *N*-heterocyclic carbene (NHC) ligands at Fe-based pre-catalysts to overcome this thermodynamic barrier, promoting efficient electrocatalytic CO production.

1.2 Research Plan

Under controlled potentials, small TON's are often observed amongst non-porphyrinoid Fe-based catalysts because of poor dissociation of CO and catalyst deactivation. This is typically caused by a thermodynamic barrier associated with the dissociation of CO in the final step of the catalytic cycle, disfavoring catalyst regeneration.[30] As a result, overcoming this barrier is an area of significant importance.

The goal of this proposal is to investigate the influence of N-heterocyclic carbenes (NHC's) in the inner coordination sphere of Fe-based CO_2 reduction electrocatalysts. It is my

hypothesis that the strongly σ-donating and π-accepting character of the NHC functional group will drastically lower the thermodynamic barrier associated with CO dissociation via the trans-effect, enhancing the number of catalytic turnovers capable under electrochemical conditions for Fe-based catalysts.

To clarify, strong σ-donating NHC's will weaken the σ-donating character of a *trans*-CO ligand at the Fe catalyst center. Additionally, π back-bonding of the NHC ligand will weaken the π accepting bond character of the CO ligand by competing with the Fe(*d*) electron density (Fig. 1.1).

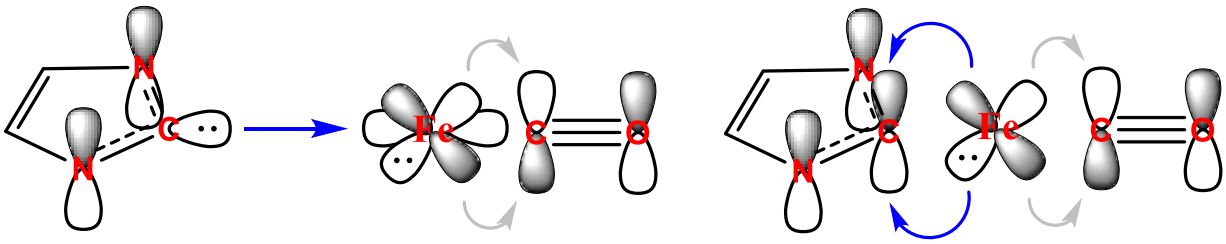

Figure 1.1. Molecular orbital representation of σ-donating (left) and π-accepting (right) character of NHC ligands and their influence on the *trans* Fe-CO bond strength.

My plan is to develop a new multidentate ligand containing a chelating NHC functional group, investigate its catalytic CO_2 reduction behavior in Fe-based complexes and maximize its electrocatalytic activity based upon proven catalyst modifications (e.g. manipulation of the second coordination sphere). The research aims of this proposal are summarized as follows:

I) *Engineering of Fe complexes containing a novel ligand with an NHC component.* Synthesis and characterization a unique Fe(II) complex that utilizes the electron donating character of NHC ligands to promote CO dissociation.

II) *Investigate the associated CO_2 reduction mechanism.* Utilize a combination of spectroelectrochemical and computational analyses to determine the optimized catalytic cycle and lay the groundwork for potential future ligand design.

III) *Expanding second coordination sphere effects to promote catalytic behavior.* Manipulate functionality of the second coordination sphere to investigate product selectivity, TOF and overpotential. Optimize experimental conditions and benchmark these new systems against existing catalysts (e.g. Tafel plot).

A detailed description of each aim is provided below:

1.2.1 Engineering of Fe complexes containing a novel ligand with an NHC component.

In recent literature, Mn(I) tricarbonyl complexes containing a pyridyl-2-NHC ligand have been studied for their influence on catalytic behavior.[31,32] In comparison to bipyridine, replacement of a pyridine ring with a NHC-based ligand generates a negative shift in the pre-catalyst reduction potential. It was observed however, that catalytic current is generated from the one-electron activated catalyst versus the two-electron activated catalyst for the bpy derivative. The observed electrochemical shift is experimentally consistent with the strong electron donating character associated with NHC's. The strong σ-donating character here evident at Mn may be favorable in Fe-based catalysts to overcome the competing, cycle ending reactions observed for $[Fe^{II}(qpy)]^{2+}$ by lowering the Fe–CO bond dissociation energy. The

thermodynamic barrier often associated with the slow dissociation of CO from Fe, preventing catalyst regeneration, is a common feature amongst iron catalysts that is observed electrochemically in the reverse CV scans performed under CO_2, usually as a weak oxidation potential around –0.70 V vs SCE.[30] It can be argued, that by adding the strong σ-donating and π-accepting electronic character of a NHC ligand, the thermodynamic barrier to CO dissociation can be significantly lowered. This argument can also be backed by the study of the more electron rich $[Co^{I}(qpy)]^{+}$ analogue as having a more electron rich metal center. Cobalt based electrocatalysts do not exhibit the same Co–CO bond cleavage issues. Based on the provided information, a pre-catalyst of structure **1** is proposed (Fig. 1.2).

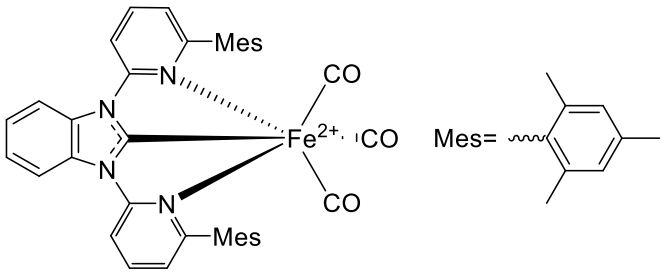

(**1**)

Figure 1.2. Structure of the proposed pre-catalyst $[Fe^{II}(NCN)\ (CO)_3]^{2+}$ (**1**).

This complex employs a unique 1,3-bis(6-phenylpyridin-2-yl)-benzo[d]imidazol-3-ium-2-ide (NCN) ligand which has not been published prior. This proposed ligand provides the ascribed NHC character as well as two electron deficient pyridine components allowing for directed electron reduction into the ligand π* orbital for electrocatalytic activation of the pre-catalyst. An added degree of tuning is also proposed here where electron donating or withdrawing groups will be added to the peripheral benzene ring of the NHC ligand to fine-

tune the σ-donating and π back-bonding character of the NHC ligand. The following series of complexes have been chosen due to their established Hammett/Taft parameters[33,34] as strongly electron donating or withdrawing groups (Figure 1.3).

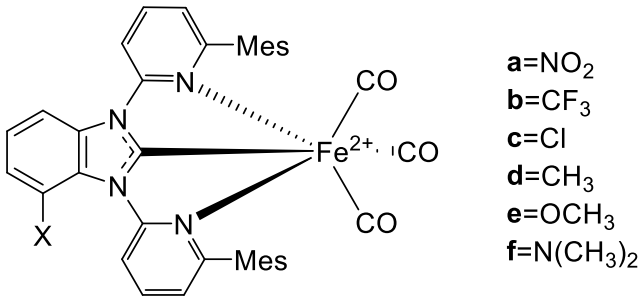

(**1a-f**)

Figure 1.3. Structures of complexes **1a-f**. X is either an electron withdrawing group or electron donating group added to the NHC component.

The addition of electron withdrawing groups such as NO_2, CF_3, and Cl will weaken the σ-donating character of the NHC ligand and invoke a positive shift in reduction potential of the pre-catalyst. Such electron-withdrawing substituents are anticipated to mitigate any desired *trans*-effect hindering Fe–CO bond cleavage. In contrast, electron donating groups such as $N(CH_3)_2$, OCH_3, and CH_3 are anticipated to behave in an opposite fashion promoting σ-donation of the NHC ligand. Investigation of this series of complexes will allow the electronic character of the NHC ligand to be optimized with respect to its influence on the Fe–CO bond cleavage reaction during the final step of electrocatalytic CO_2 reduction. In summary, the first aim of this proposal is to synthesize a series of Fe-NHC based pre-catalysts and complete their structural characterization. ^{1}H NMR, high-resolution mass spectrometry will be used for

confirmation of structures and the pseudo “vacant” coordination site (written in as occupied by CO) will be characterized via FTIR spectroscopy of the complex in various solvents, both coordinating and non-coordinating. X-ray crystallography will also be conducted in order to identify bond lengths and angles associated with the complex. FTIR spectroscopy will be particularly informative by identifying the *trans*-*v*(CO) stretching frequency to indirectly assess the σ-donating and π back-bonding character of each NHC ligand. Further investigation will involve an in-depth electrochemical study via cyclic voltammetry, in order to determine the influence of the NHC component of the ligand.

1.2.2 Investigation of the CO_2 reduction mechanism

The second aim of this project is to identify the mechanism(s) involved in CO_2 reduction by the proposed $[Fe^{II}(NCN)(CO)_3]^{2+}$ catalyst and identify the products generated. Based upon the literature associated with Fe catalysis[22-26,30] as well as the literature on Mn-NHC complexes,[31,32] the following competing catalytic cycles are anticipated for this new Fe-NHC based catalysts:

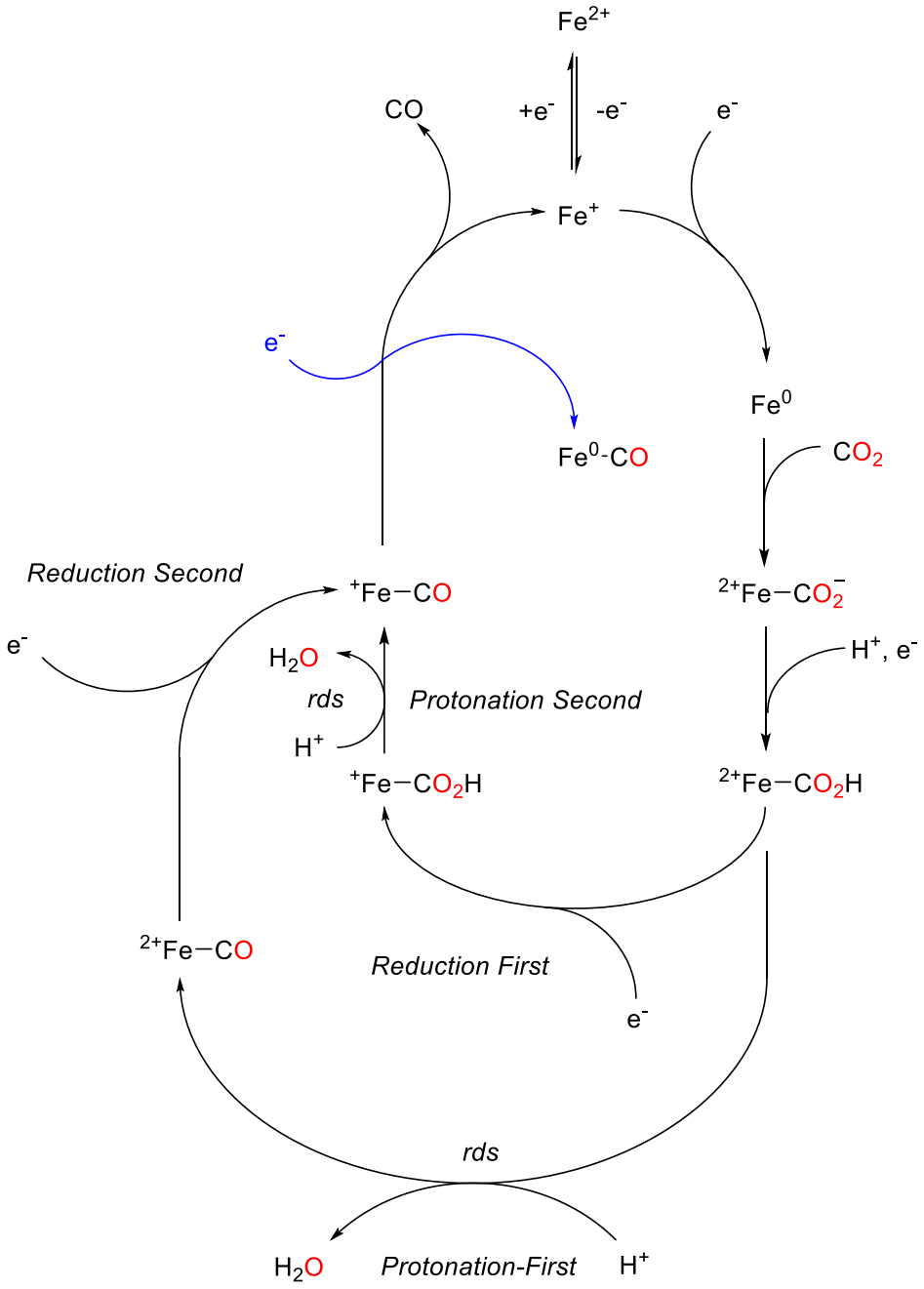

Scheme 1.4. Anticipated competing mechanisms of CO_2 reduction with Fe-NHC complexes.

A secondary "protonation-first" pathway is included in this scheme as a potential alternative lower overpotential pathway previously observed in Mn bpy and NHC electrocatalyst

literature.[32,35] This pathway is observed by lowering the transition state energy associated with C–OH bond cleavage of the metallocarboxylic acid. The σ-donating and π-accepting character of the NHC ligand inductively contributes to the lowering of the transition state energy, increasing the possibility of cycling through the protonation first pathway. To what extent these characteristics influence the catalysts synthesized and the overall mechanistic nature of the catalysts will be determined experimentally.

All complexes will first be studied electrochemically under Ar, CO_2 and CO. Studying the catalyst's reduction events under CO_2 allows us to determine at what reduction event CO_2 binds and at what overpotential catalytic activity grows in. The possibility of an oxidative potential in the reverse scan related to CO dissociation from the Fe center may be observed and it can be determined whether binding strength has weakened based on the position and current of the oxidation as well as calculation of the CO binding constant K_Q using Eq. 15.

$$E = E^o + \left(\frac{RT}{nF}\right) \ln (1 + [CO]K_Q) \qquad (15)$$

It is presumed however, that the binding strength of CO to the Fe center may be significantly weakened by the strongly donating character of the NHC component of the ligand. Therefore, an Fe–CO based oxidation potential appearing in the reverse scan may not occur. In the event this oxidation event is present, a second set of CV experiments may be performed under CO to confirm that the oxidation potential in the reverse wave is truly indication of CO dissociation from the complex. If the oxidative potential in the reverse scan that matches the potential under CO_2, it would be evident that the original potential is of the oxidation of the complex and

dissociation of CO. Electrochemical experiments will be performed in acetonitrile with ~5% (2.78 M) H_2O added to be used as a proton source with a known pH, allowing η to be calculated for the catalysts. Additional experiments will be performed with varying concentrations of added phenol (PhOH) as a strong acid to measure the enhancement of catalyst TOF and the protonation first pathway albeit without the capability of to measure pH and η. All redox potentials will be reported versus the ferrocenium/ferrocence ($Fc^{+/0}$) pseudo reference as recommended by Appel and Helm.[16] If steady state conditions cannot be identified Saveant's foot-of-the-wave method will be employed (Eq. 16) to estimate TOF_{max}.[36,37]

$$\frac{i_{cat}}{i_p} = \frac{2.24\sqrt{\left(\frac{RT}{Fv}\right)TOF_{max}}}{1+\exp\left[\left(\frac{F}{RT}\right)\left(E-E^0_{\frac{P}{Q}}\right)\right]}\left(\frac{n_{cat}}{n_p^{\frac{3}{2}}}\right) \qquad (16)$$

Infrared spectroelectrochemisty (IR-SEC) experiments under CO_2 and CO will be performed to observe the binding of CO_2 and CO to the Fe center based on CO stretches forming. Under CO_2, the binding of the gas to the complex can be monitored by looking for a change in CO stretches under varying constant potentials. Upon applying the potential necessary for CO_2 reduction, disproportionation may occur with another equivalent of CO_2 and the IR bands associated with CO may grow in in place of the bound CO_2 molecule. To confirm the *ν*(CO) assignments collected from these IR-SEC experiments, geometry optimized DFT frequency calculations will be performed to try and mimic the vibrational bands observed and assign a structure with a step in the catalytic cycle. Additionally, a UV-vis SEC experiment under CO_2 will also be conducted and the spectra will be overlaid atop TDDFT spectra of potential intermediates in the catalytic cycle to further confirm the binding of CO_2. Lastly, an entire DFT

study of all potential intermediates and transition states will be done to determine the likely catalytic pathway(s) and a cycle will be assigned using these complexes. All DFT calculations will be done using the B3PW91 functional. H, C, N, and O atoms will use the 6-31G(d,p) and Fe will use the SDD basis sets respectively.[38] Structures of complexes **1**-**4** will be optimized along with all potential intermediates. Transition-states will additionally be calculated, and a map of energy barriers will be constructed for all potential catalytic pathways.

1.2.3 Effects of functional groups in the second coordination sphere

The use of the second coordination sphere is a regularly employed strategy that is used to lower transition state energies,[28,39] open alternate catalytic pathways,[40] and improve the overall performance of a catalyst. Thus, it is a logical step here that a variety of second coordination sphere functional groups be employed to further optimize the proposed Fe-NHC based catalyst. The following R-groups are proposed as second coordination sphere functional groups, defined by their character as a Brønsted Acid, a Lewis base or as a species that affords coulombic stabilization.

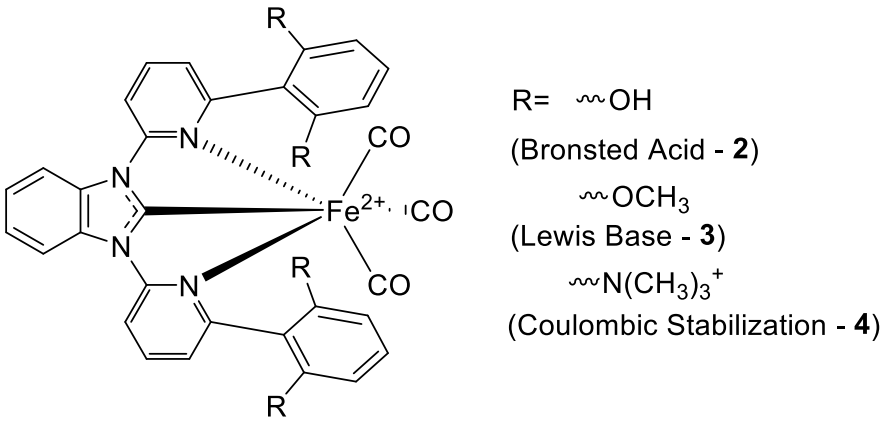

Figure 1.4. Structures of complexes with second coordination sphere functionalities and their natures.

Brønsted Acid. Having a Brønsted acid in the second coordination sphere works as near space functional group that helps shuttle protons to the metal bound CO_2 ligand or metallocarboxylate/metallocarboxylic acid intermediates.[28] Using the hydroxy functional group permits easy generation of the metallocarboxylic acid and subsequent formation of water by lowering the transition state energies of both protonation steps. This is done via stabilization through hydrogen bonding between the acidic proton of the hydroxyl groups and an oxygen on CO_2, which weakens the C=O and C-OH bond energies in each step respectively (Fig. 1.5).

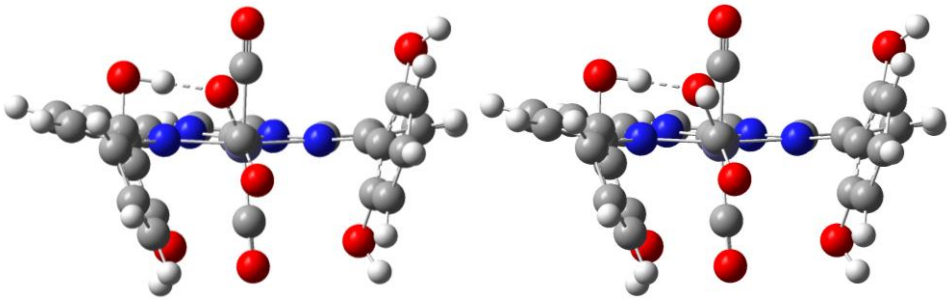

Figure 1.5. Estimated transition state analysis of the (left) Fe carboxylate complex intermediate and (right) Fe metallocarboxylic acid complex intermediate with an intermolecular Brønsted acid. Both exhibit the aforementioned hydrogen bonding between an oxygen of the substrate and the acidic proton in the second coordination sphere.

Lewis Bases. The influence of adding a pendant Lewis base into the second coordination sphere of a Mn 2,2'-bipyridine (bpy) tricarbonyl catalyst has recently been reported by Ngo et al.[40] By taking advantage of second-coordination sphere hydrogen-bonding to promote PCET

and reduce the activation energy of the rate-determining step of C-OH bond cleavage, the protonation first pathway was activated. This alternate pathway is the first of its kind to be experimentally identified for Mn bpy catalysts beyond first being proposed computationally by Riplinger and Carter[41].

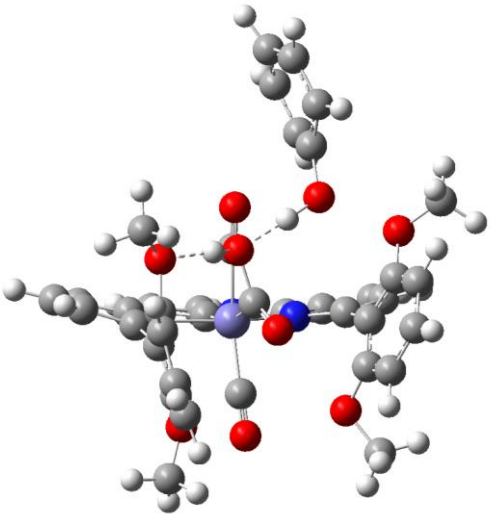

Figure 1.6. Estimated transition state of the Fe metallocarboxylic acid complex intermediate with a Lewis base in the second coordination sphere. The base exhibits hydrogen bonding to the carboxylic acid proton and the acid's O atom exhibits hydrogen bonding with an additional proton source, phenol.

It is likely that the respective Fe catalyst can mimic the transition state associated with activating the protonation first pathway constructed by Ngo et al (Fig. 1.6).[40] Considering this information, it is plausible that the addition of methoxy groups in the second coordination sphere can activate or enhance the kinetics of the protonation first pathway for the respective Fe-catalyst.

Coulombic Stabilization. In recent literature, the addition of trimethylammonium groups to the second coordination sphere near the reacting center have been reported to improve TOF and η.[39] These observed changes have been attributed to a through-space inductive charge interaction that stabilizes the addition of negative charge at the CO_2 substrate/ligand. By adding trimethylammonium groups in a similar fashion to the proposed Fe-NHC pre-catalysts, a consistent effect should exist and improve the proposed catalyst characteristics similarly.

Using modified synthetic procedures from existing literature,[42] the ligands for Fe complexes **1**-**4** can be synthesized. The mesityl (**1**) and methoxy (**3**) functional groups can be introduced initially and maintained throughout the steps from generating **5**-**8**. A simple hydrolysis of the methoxy groups as a last step will generate the ligand necessary to generate complex **2**. To generate the ligand for complex **4**, dimethylamine functional groups are used through the last step and then the ligand is refluxed with methyl trifluoromethanesulfonate for 24 hours.[39]

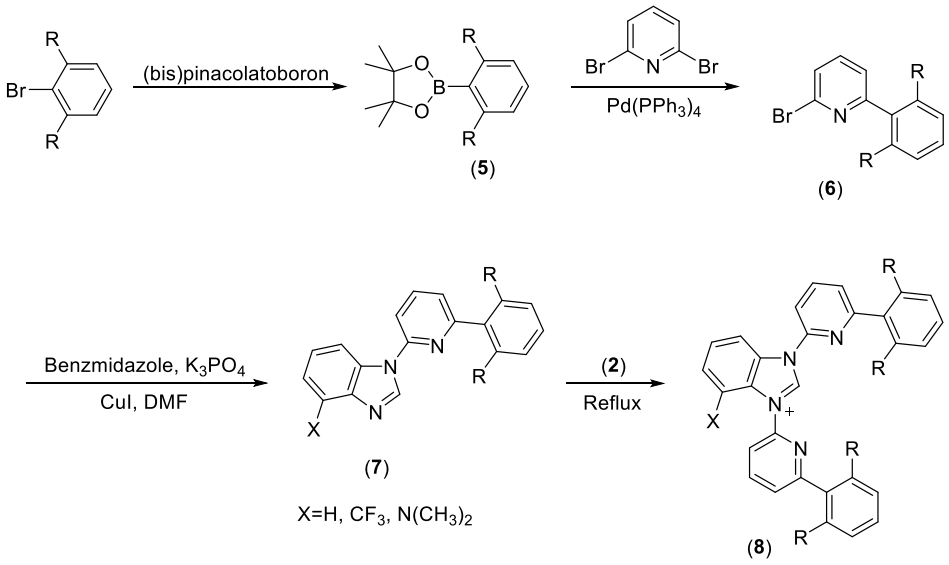

Scheme 1.5. Proposed synthesis of NHC ligand precursors.

Synthesis of the Fe catalysts is relatively simple and will be conducted per Scheme 6:

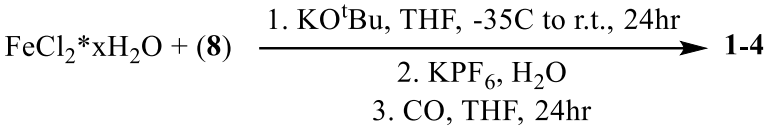

Scheme 1.6. Proposed synthesis of Fe-NHC complexes.

In a one pot synthesis consistent with the generating Mn-NHC complexes,[31,32] the ligand precursor (**8**) is oxidized into an NHC with potassium tert-butoxide and subsequently complexed to Fe at room temperature. Following this the complex undergoes a metathesis to exchange the chloride counterions with hexafluorophosphates and lastly, the remaining coordination sites are exchanged with CO by stirring in an airtight cell purged with CO.

1.3 Experimental Methods

All catalysts (**1-4**) will be studied to determine TOF_{max}, and η so that they can be benchmarked against other existing catalysts in a catalytic Tafel plot relating the two values to one another. Following this, controlled potential electrolysis (CPE) experiments will be completed with each catalyst to assess the degree to which the *trans*-effect of the NHC components weaken the Fe–CO bond and evaluate TON's under purely electrocatalytic conditions. Catalyst overpotential (η) will only be reported using a buffered electrolyte with a known pH. For non-aqueous electrolytes this requires knowledge of the CO_2 to CO equilibrium potential ($E_{CO_2/CO}$) at an identical pH. η is defined by Eq. 9. $E_{CO_2/CO}$ is pH-dependent (Eq. 17).

$$\mathrm{E_{CO_2/CO}} = \mathrm{E^{o}_{CO_2/CO}} - \left(\frac{2.303\mathrm{RT}}{2\mathrm{F}}\right) \cdot 2\mathrm{pH} \qquad (17)$$

The non-aqueous equilibrium potential of $E^{o}_{CO_2/CO}$ = –0.13 V vs $Fc^{+/0}$ for the reduction of CO_2 to CO in dry acetonitrile, represents a very specific reaction condition.[43] Using a buffered Brønsted acid with a known pK_a in acetonitrile it is possible to correct $E^{o}_{CO_2/CO}$ using the pH-dependent Nernst equation (Eq. 15) allowing accurate calculation of the true overpotential. Bulk electrolysis is conducted to confirm computationally derived structures (via spectroelectrochemistry) and product distribution of catalytic reactions by quantifying both the Faradaic yield and the TON of each product. Experimental conditions are informed by optimized voltammetric analysis. A 25 mL (5 mL electrolyte + 20 mL headspace) custom made airtight Adams & Chittenden bulk electrolysis cell is used, with a porous vitreous carbon working electrode, Pt-gauze counter electrode (separated by a vycor glass tube + frit assembly) and an acetonitrile-based $Ag^{+/0}$ reference electrode (calibrated with $Fc^{+/0}$). Ferrocene is added to the counter electrode compartment as a sacrificial reductant. CO and H_2 are monitored by GC analysis.

1.4 References

(1) Anderson, T.; Hawkins, E.; Jones, P. CO_2, the greenhouse effect and global warming: from the pioneering work of Arrhenius and Callendar to today's Earth System Models. Endeavour Vol. 40 No.3, 178-187.

(2) Benson, E. E.; Kubiak, C. P.; Sathrum, A. J.; Smieja, J. M. Electrocatalytic and homogeneous approaches to conversion of CO_2 to liquid fuels. Chem. Soc. Rev. 2009, 38 (1), 89−99.

(3) Senftle, T. P.; Carter, E. A. The Holy Grail: Chemistry Enabling an Economically Viable CO_2 Capture, Utilization, and Storage Strategy. Acc. Chem. Res. 2017, 50 (3), 472−475.

(4) P. Lahijani, Z.A. Zainal, M. Mohammadi, A.R. Mohamed. Conversion of the greenhouse gas CO_2 to the fuel gas CO via the Boudouard reaction: A review. Renew. Sus. Energ. Rev., 41 (2015), pp. 615-632.

(5) K. Aasberg-Petersen, I. Dybkjaer, C.V. Ovesen, N.C. Schjodt, J. Sehested, S.G. Thomsen. Natural gas to synthesis gas - Catalysts and catalytic processes. J. Nat. Gas Sci. Eng., 3 (2011), pp. 423-459.

(6) Q.H. Zhang, J.C. Kang, Y. Wang. Development of Novel Catalysts for Fischer-Tropsch Synthesis: Tuning the Product Selectivity. Chem. Cat. Chem., 2 (2010), pp. 1030-1058.

(7) H.A. Schwarz, R.W. Dodson. Reduction potentials of CO_2^- and the alcohol radicals. J. Phys. Chem., 93 (1989), pp. 409-414.

(8) Matsubara, Y.; Grills, D.; Kuwahara Y. Thermodynamic Aspects of Electrocatalytic CO_2 Reduction in Acetonitrile and with an Ionic Liquid as Solvent or Electrolyte. ACS Catal. 2015, 5, 6440−6452.

(9) Whipple, D. T.; Kenis, P. J. A. Prospects of CO_2 Utilization via Direct Heterogeneous Electrochemical Reduction. J. Phys. Chem. Lett. 2010, 1, 3451−3458.

(10) Li, Y.; Chan, S. H.; Sun, Q. Heterogeneous catalytic conversion of CO_2: a comprehensive theoretical review. Nanoscale 2015, 7, 8663− 8683.

(11) Genovese, C.; Ampelli, C.; Perathoner, S.; Centi, G. Electro- catalytic conversion of CO_2 to liquid fuels using nanocarbon-based electrodes. J. Energy Chem. 2013, 22, 202−213.

(12) Qiao, J.; Liu, Y.; Hong, F.; Zhang, J. A review of catalysts for the electroreduction of carbon dioxide to produce low-carbon fuels. Chem. Soc. Rev. 2014, 43, 631−675.

(13) Benson, E. E.; Kubiak, C. P.; Sathrum, A. J.; Smieja, J. M. Electrocatalytic and homogeneous approaches to conversion of CO2 to liquid fuels. Chem. Soc. Rev. 2009, 38,89−99.

(14) Rountree, E. S.; McCarthy, B. D.; Eisenhart, T. T.; Dempsey, J. L. Evaluation of homogeneous electrocatalysts by cyclic voltammetry. Inorg. Chem. 2014, 53, 9983−10002.

(15) Francke, R.; Little, R. D. Redox catalysis in organic electrosynthesis: basic principles and recent developments. Chem. Soc. Rev. 2014, 43, 2492−2521.

(16) Appel, A.; Helm, M. Determining the Overpotential for a Molecular Electrocatalyst, Acs Catalysis 2014, 4 (2), 630-633.

(17) Andrieux, C. P.; Blocman, C.; Dumas-Bouchiat, J. M.; M'Halla, F.; Saveant, J. M. Homogeneous redox catalysis of electrochemical reactions: Part V. Cyclic voltammetry. J. Electroanal. Chem. Interfacial Electrochem. 1980, 113, 19−40.

(18) Grills, D. C.; Matsubara, Y.; Kuwahara, Y.; Golisz, S. R.; Kurtz, D. A.; Mello, B. A. Electrocatalytic CO_2 Reduction with a Homogeneous Catalyst in Ionic Liquid: High Catalytic Activity at Low Overpotential. J. Phys. Chem. Lett. 2014, 5, 2033−2038.

(19) Francke, R.; Schille, B.; Roemelt, M. Homogeneously Catalyzed Electroreduction of Carbon Dioxide: Methods, Mechanisms, and Catalysts. Chem. Rev. 2018, 118, 4631−4701.

(20) Collman, J.; Brauman, J.; Halbert, T.; Suslick, K. Nature of O_2 and CO binding to metalloporphyrins and heme proteins. Proc Natl Acad Sci U S A. 1976 Oct; 73(10): 3333–3337.

(21) Daskalakis, V.; Varotsis, C. Binding and Docking Interactions of NO, CO and O_2 in Heme Proteins as Probed by Density Functional Theory. Int J Mol Sci. 2009 Sep; 10(9): 4137–4156. Published online 2009 Sep 22.

(22) Hammouche, M.; Lexa, D.; Savéant, J. M.; Momenteau, M. Catalysis of the electrochemical reduction of carbon dioxide by iron("0") porphyrins. J. Electroanal. Chem. Interfacial Electrochem. 1988, 249, 347−351.

(23) Hammouche, M.; Lexa, D.; Momenteau, M.; Savéant, J. M. Chemical catalysis of electrochemical reactions. Homogeneous catalysis of the electrochemical reduction of carbon dioxide by iron(″0″) porphyrins. Role of the addition of magnesium cations. J. Am. Chem. Soc. 1991, 113, 8455−8466.

(24) Bhugun, I.; Lexa, D.; Savéant, J.-M. Ultraefficient selective homogeneous catalysis of the electrochemical reduction of carbon dioxide by an iron(0) porphyrin associated with a weak Brønsted acid cocatalyst. J. Am. Chem. Soc. 1994, 116, 5015−5016.

(25) Bhugun, I.; Lexa, D.; Savéant, J.-M. Catalysis of the Electrochemical Reduction of Carbon Dioxide by Iron(0) Porphyrins. Synergistic Effect of Lewis Acid Cations. J. Phys. Chem. 1996, 100, 19981−19985.

(26) Bhugun, I.; Lexa, D.; Savéant, J.-M. Catalysis of the Electrochemical Reduction of Carbon Dioxide by Iron(0) Porphyrins: Synergystic Effect of Weak Brønsted Acids. J. Am. Chem. Soc. 1996, 118, 1769−1776.

(27) Costentin, C.; Drouet, S.; Passard, G.; Robert, M.; Savéant, J. Proton-Coupled Electron Transfer Cleavage of Heavy-Atom Bonds in Electrocatalytic Processes. Cleavage of a C−O Bond in the Catalyzed Electrochemical Reduction of CO_2. J. Am. Chem. Soc. 2013, 135, 9023−9031.

(28) Costentin, C.; Drouet, S.; Robert, M.; Savéant, J.-M. A local proton source enhances CO_2 electroreduction to CO by a molecular Fe catalyst. Science 2012, 338,90−94.

(29) Costentin, C.; Passard, G.; Robert, M.; Savéant, J.-M. Pendant acid-base groups in molecular catalysts: H-bond promoters or proton relays? Mechanisms of the conversion of CO2 to CO by electro- generated iron(0)porphyrins bearing prepositioned phenol function- alities. J. Am. Chem. Soc. 2014, 136, 11821−11829.

(30) Cometto, C.; Chen, L.; Lo, P.; Guo, Z.; Lau, K.; Anxolabéhère-Mallart, E.; Fave, C.; Lau, T.; Robert, M. Highly Selective Molecular Catalysts for the CO2-to-CO Electrochemical Conversion at Very Low Overpotential. Contrasting Fe vs Co Quaterpyridine Complexes upon Mechanistic Studies. ACS Catal. 2018, 8, 3411−3417.

(31) Agarwal, J.; Shaw, T.; Stanton, C.; Majetich, G.; Bocarsly, A.; Schaefer, H. NHC-Containing Manganese(I) Electrocatalysts for the Two-Electron Reduction of CO_2. Angew. Chem. Int. Ed. 2014, 53, 5152 –5155.

(32) Stanton, C.; Vandezande, J.; Majetich, G.; Schaefer, H.; Agarwal, J. Mn-NHC Electrocatalysts: Increasing π Acidity Lowers the Reduction Potential and Increases the Turnover Frequency for CO_2 Reduction. Inorg. Chem. 2016, 55, 9509−9512.

(33) Hansch, C.; Leo, A.; Taft, W. A Survey of Hammett Substituent Constants and Resonance and Field Parameters. Chem. Rev. 1991 (2): 165–195.

(34) Anslyn, E.; Dougherty, D. A. Modern Physical Organic Chemistry; University Science Books, 2006, p 455.

(35) Sampson, M.; Nguyen, A.; Grice, K.; Moore, C.; Rheingold, A.; Kubiak, C. Manganese Catalysts with Bulky Bipyridine Ligands for the Electrocatalytic Reduction of Carbon Dioxide: Eliminating Dimerization and Altering Catalysis. J. Am. Chem. Soc. 2014, 136, 14, 5460-5471.

(36) Cyrille, Costentin; J.-M. Savéant. Multielectron, Multistep Molecular Catalysis of Electrochemical Reactions: Benchmarking of Homogeneous Catalysts, ChemElectroChem 2014, 1 (7), 1226-1236.

(37) E. S. Rountree; B. D. McCarthy; T. T. Eisenhart; J. L. Dempsey. Evaluation of Homogeneous Electrocatalysts by Cyclic Voltammetry, Inorganic Chemistry 2014, 53 (19), 9983-10002.

(38) Atkins, P.; De Paula, J. Atkin's Physical Chemistry. 2006, 8th edition.

(39) Azcarate, I.; Costentin, C.; Robert, M.; Savéant, J.; Through-Space Charge Interaction Substituent Effects in Molecular Catalysis Leading to the Design of the Most Efficient Catalyst of CO_2-to-CO Electrochemical Conversion. J. Am. Chem. Soc. 2016, 138, 16639−16644.

(40) Ngo, K.; McKinnon, M.; Mahanti, B.; Narayanan, R.; Grills, D.; Ertem, M.; Rochford, J. Turning on the Protonation-First Pathway for Electrocatalytic CO_2 Reduction by Manganese Bipyridyl Tricarbonyl Complexes. J. Am. Chem. Soc. 2017, 139, 2604−2618.

(41) Riplinger, C.; Carter, E. Influence of Weak Brønsted Acids on Electrocatalytic CO_2 Reduction by Manganese and Rhenium Bipyridine Catalysts. ACS Catal. 2015, 5, 2, 900-908.

(42) Deißler, C.; Rominger, F.; Kunz, D. Controlling the coordination modes of a new and highly flexible ligand bearing two N-heterocyclic carbene moieties at a bipyridine backbone. Dalton Trans., 2009, 7152–7167.

(43) Y. Matsubara; D. C. Grills; Y. Kuwahara. Thermodynamic Aspects of Electrocatalytic CO2 Reduction in Acetonitrile and with an Ionic Liquid as Solvent or Electrolyte, Acs Catalysis 2015, 6440-6452.

CHAPTER 2

NEAR-INFRARED ABSORBANCE OF RUTHENIUM(II) PHOTOSENSITIZERS CONTAINING A MEROCYANINE π-ACCEPTOR

2.1 Introduction

Ruthenium polypyridyl complexes incorporating non-innocent ligands (NILs) have become the focus of many recent studies due to their usefulness in engineering molecular redox properties.[1-5] A metal complex exhibits non-innocence as the result of metal(dπ)-ligand(π) bonding, generating hybrid molecular orbitals which preclude formal assignment of the metal center's oxidation state.[3,6] Considering this, NIL's can be understood as redox-active ligands that alter the electronic structure of the complex as opposed to simply displaying redox activity.[7] In this study, the non-innocent nature of complexes covalently bonded to the 5-(vinyl-cyanine)-8-oxyquinolate ligand system is studied at the d^6 Ru(II) metal center. It is well established that Ru(II) polypyridyl complexes provide an ideal platform for metal(dπ)-ligand(π) covalent mixing and have broad potential in photophysical and catalytic applications.[4,8-12] The motivation behind this ligand system comes from its potential to exhibit

exceptionally strong absorption (~4.8 x 10^4 M^{-1} cm^{-1}) tailing into the phototherapeutic window or near-infrared (NIR) region of the electronic spectrum, as reported in a recent publication.[13] This single example offers an attractive approach to developing photosensitizers capable of redox activity in range for biological imaging as well as the formation of low energy light absorbing photosensitizers for various photocatalytic reactions. A family of five bis-heteroleptic ruthenium(II) complexes containing a series of 5-(vinyl-cyanine)-8-oxyquinolate ligands (**RuL2**$^{2+}$-**RuL6**$^{2+}$) are presented here where varying cyanine π-acceptors are introduced to better understand how the effects they have on their photophysical and electrochemical properties (scheme 2.1). An in-depth spectroscopic and electrochemical analysis is presented and supported by computational studies to give a detailed picture of these properties.

2.2 Results and Discussion

2.2.1 Synthesis

The 8-hydroxyquinoline ligand **HL1** is commercially available, however each of the 5-(vinyl-cyanine)-8-hydroxyquinoline ligand precursors were prepared via a two-step synthesis using an efficient microwave-based procedure inspired by a previously reported method.[14] Briefly, iodomethane was superheated in the microwave for 15 minutes with one of the corresponding *N*-heterocyclic teratiary amine precursors **(P1** – **P5**, Scheme 2.1). After removal of the solvent ex vacuo, the *N*-methyl quarternized iodide salt intermediates (**I1**$^+$ – **I5**$^+$, scheme 2.1) were isolated via sonication of the crude solid residue in hexanes followed by vacuum filtration and rinsing with hexanes. Intermediates **I1**$^+$ – **I5**$^+$ were then subjected to condensation

with 8-hydroxyquinoline-5-carbaldehyde, again via 15 minutes microwave heating, in ethanol with 0.1 equivalents of piperidine as a weak base. Following isolation of the solid iodide salts by precipitation with excess diethyl ether, analytically pure protonated ligand precursors **HL2**$^{+}$ – **HL6**$^{+}$ were isolated as their PF_6^- salts by metathesis in an ethanol:water mixture (1:1) upon addition of an aqueous KPF_6 solution.[15-17] The zwitterionic merocyanine ligands were generated in-situ using triethylamine in methanol and reacted with *cis*-dichloridobis(2,2'-bipyridine)ruthenium(II) in the microwave for 15 minutes. Analytically pure $[RuL(bpy)_2]^{2+}$ complexes **RuL2**$^{2+}$ - **RuL6**$^{2+}$ were isolated as their bis-PF_6^- salts by metathesis of the ethanol reaction mixture with aqueous KPF_6 followed by removal of the bulk ethanol ex vacuo and recrystallization of the filtered solid from acetone with excess diethyl ether.

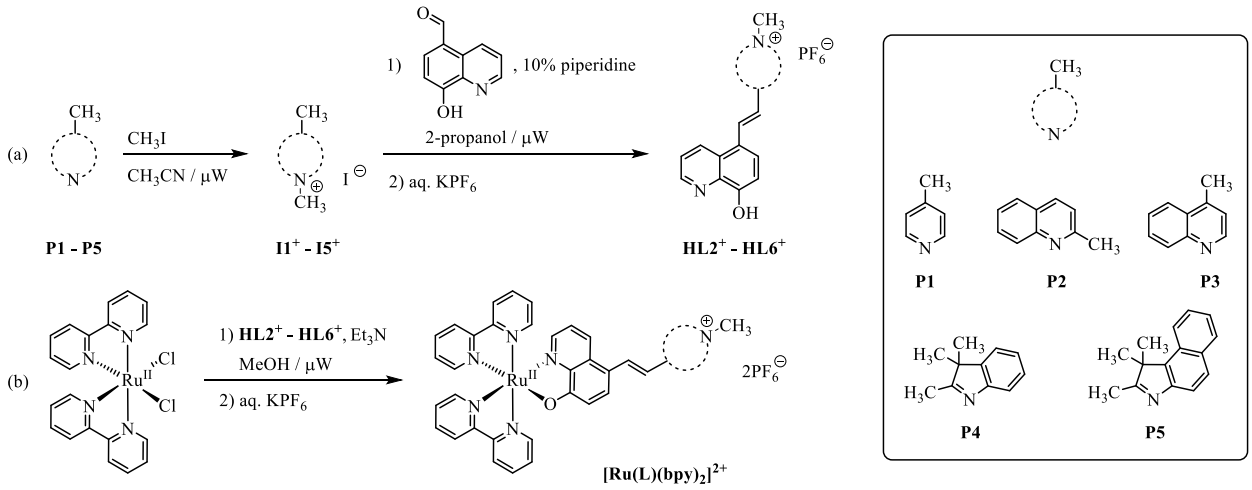

Scheme 2.1. Summary of synthetic pathways adapted for the preparation of (a) protonated ligand precursors **HL2** – **HL6** and (b) $[RuL((bpy)_2]^{2+}$ complexes **RuL2**$^{2+}$ - **RuL6**$^{2+}$.

2.2.2 Electronic Absorption Spectroscopy

The benchmark $[Ru(bpy)_3]^{2+}$ chromophore has been extensively investigated and employed for a wide variety of applications due to its strong visible absorption which peaks at 450 nm in acetonitrile (ε = 1.46 x 10^4 M^{-1} cm^{-1}), attributed to a combination of two singlet metal-to-ligand charge-transfer (^{1}MLCT) electronic transitions (see below for a full discussion of TDDFT computational analysis).[18-21] Replacement of a single bpy ligand with the 8-oxyquinolate anion in **RuL1**$^+$ generates a broader, red-shifted absorption profile enhancing its light harvesting capability with absorption maxima in acetonitrile occurring at 400 nm (ε = 0.77 x 10^4 M^{-1} cm^{-1}) and 496 nm (ε = 1.21 x 10^4 M^{-1} cm^{-1}).[5] The broad panchromatic absorption of **RuL1**$^+$ is the result of many ^{1}MLCT and (metal-ligand)-to-ligand charge-transfer (^{1}MLLCT) electronic transitions, due to the decreased C_1 symmetry, relative to D_3 for $[Ru(bpy)_3]^{2+}$. The ^{1}MLLCT transitions occur because of covalent mixing of the populated Ru $d(\pi)$ and OQN(π) orbitals (aka ligand non-innocence) which causes significant narrowing of the optical bandgap.

The high-energy UV absorption bands of **RuL2**$^{2+}$ - **RuL6**$^{2+}$ observed from 353 - 359 nm consist primarily of H-3→L+3 and HOMO→L+5 transitions which are [Ru(dπ)-mer(π)]→[Ru(d*)-mer(π*)] and [Ru(dπ)-mer(π)]→bpy(π*) in character, respectively. Minor contributions from Ru(dπ)→bpy(π*) transitions, similar to $[Ru(bpy)_3]^{2+}$, are present but of significantly lower intensity compared to the latter merocyanine based electronic transitions. The extinction coefficients of these absorption bands range from 1.14 x 10^4 M^{-1} cm^{-1} for **RuL5**$^+$ to 1.95 x 10^4 M^{-1} cm^{-1} for **RuL2**$^+$, significantly more intense than the weak band exhibited by

$[Ru(bpy)_3]^{2+}$ at 350 nm (ε = 0.60 x 10^4 M^{-1} cm^{-1}). The visible absorption bands of the quinolinium and imidazolium based merocyanine complexes **RuL3**$^+$ - **RuL6**$^+$ each exhibit characteristics similar to the simple $[Ru(OQN)(bpy)_2]^+$ complex in that there appears to be multiple overlapping visible absorption bands; again consistent with the reduction in symmetry relative to $[Ru(bpy)_3]^{2+}$ and the presence of many close lying ^{1}MLCT and ^{1}MLLCT electronic transitions.

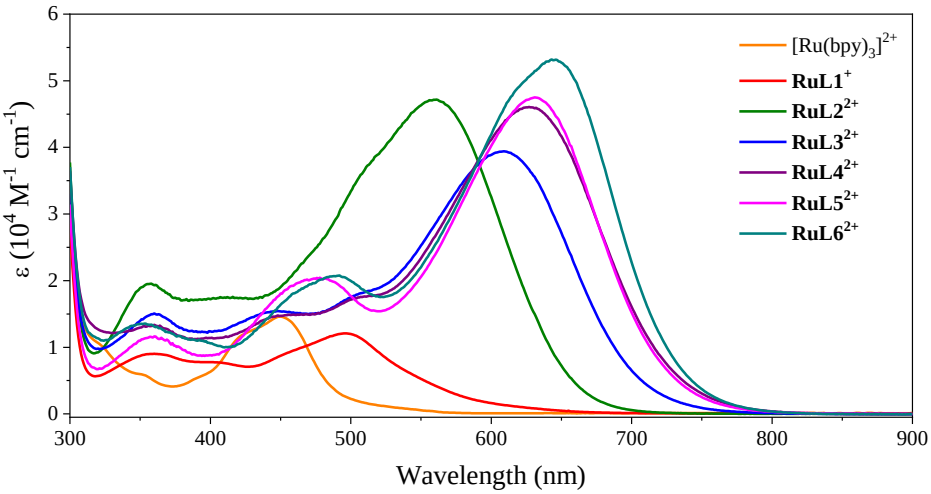

Figure 2.1. Overlay of UV-vis absorption spectra for complexes $[Ru(bpy)_3]^{2+}$-**RuL6**$^{2+}$.

This is less obvious for the pyridinium substituted merocyanine complex **RuL2**$^{2+}$ due to the occurrence of an intense and broad ^{1}MLCT absorption band at 561 nm (ε = 4.72 x 10^4 M^{-1} cm^{-1}), primarily HOMO→LUMO [Ru $d(\pi)$→merocyanine(π^*)] in character, which dominates the visible region of its spectrum. Indeed, in stark contrast to $[Ru(bpy)_3]^{2+}$ and **RuL1**$^+$, all merocyanine complexes exhibit intense and broad vis-NIR absorption bands with maxima ranging from 561 – 646 nm. As detailed in the TDDFT discussion below these are primarily ^{1}MLCT in nature derived from a single HOMO→LUMO electronic transition of Ru

$d(\pi)\rightarrow$merocyanine(π^*) character with λ_{max} shifting to lower energy with increasing conjugation of the terminal merocyanine acceptor group according to the trend; pyridinium (**L2**) < *o*-quinolinium (**L3**) < *p*-quinolinium (**L4**) < imidazolium (**L5**) < benzimidazolium (**L6**). These bands exhibit large molar extinction coefficients ranging from 39,500 for $\mathbf{RuL3^{2+}}$ to 53,200 M^{-1} cm^{-1} for $\mathbf{RuL6^{2+}}$, and due to the large full-width half-maxima (fwhm) of this vis-NIR band ranging from 3,279 cm^{-1} for $\mathbf{RuL5^{2+}}$ to 5,062 cm^{-1} for $\mathbf{RuL1^{2+}}$ these bands tail as far out as 800 nm.

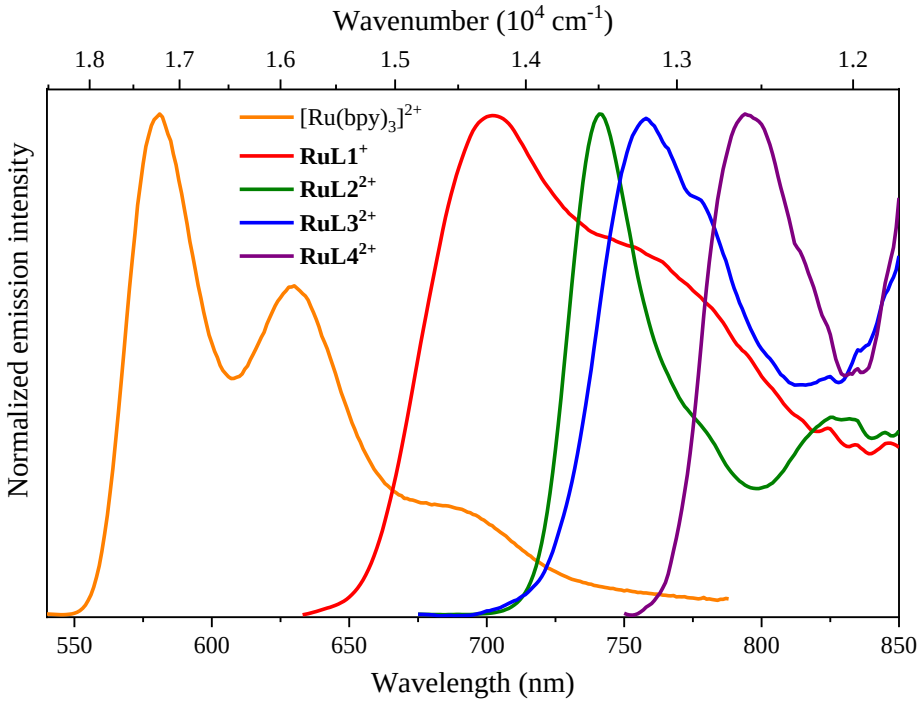

Figure 2.2 Overlay of corrected emission spectra for $\mathbf{Ru1^{2+}}$-$\mathbf{Ru5^{2+}}$ recorded in a frozen EtOH/MeOH (4:1) glass at 77 K.

Corrected low temperature ^{3}MLCT phosphorescence emission spectra of all ruthenium dyes were recorded in ethanol:methanol 4:1 frozen into a glass at 77 K and are presented in Figure

7. In comparison to $[Ru(bpy)_3]^{2+}$, oxyquinolate complexes **RuL1**$^{+}$-**RuL4**$^{2+}$ show very weak emission only observable far below room temperature. This behavior falls in line with the energy-gap law [$k_{nr} \propto \exp(-E_0)$] which dictates that the rate constant for nonradiative decay (k_{nr}) increases exponentially with a decreasing $T_1 \rightarrow S_0$ energy.[22] Consistent with absorbance, destabilization of the HOMO of **RuL1**$^{+}$ gives a broader emission profile compared to $[Ru(bpy)_3]^{2+}$ as well as a similar degree of red-shifting (581→701 nm). Complexes **RuL2**$^{2+}$-**RuL4**$^{2+}$ have emission spectra at 741, 758 and 794 nm respectively, similar in trend to their absorption maxima and exhibit poor vibrational fine structure. Due to the poorly emissive nature of these complexes, quantum yields could not be accurately obtained and radiative decay time constants were beyond the time resolution of the instrumentation used (~200 ps). The remaining complexes **RuL5**$^{2+}$-**RuL6**$^{2+}$ exhibit no emission even upon cooling to 77 K.

Table 2.1 UV-Vis Electronic Absorption and Phosphorescence Emission Data

	abs $\lambda_{max}{}^{a}$ (nm) (ε x 10^4 M^{-1} cm^{-1})	em $\lambda_{max}{}^{b}$ (nm)
$[Ru(bpy)_3]^{2+}$	243 (2.49), 286 (7.79), 430 (sh), 450 (1.46)	581, 630, 680 (sh)
RuL1^{+}	257 (4.20), 291 (4.31), 360 (0.90), 400 (0.77), 496 (1.21)	703, 761 (sh)
RuL2^{2+}	256 (4.64), 291 (6.05), 356 (1.95), 411 (1.76), 561 (4.72)	741
RuL3^{2+}	292 (4.92), 359 (1.50), 445 (1.54), 500 (sh), 609 (3.95)	758

RuL4^{2+}	293 (5.39), 359 (1.30), 456 (1.49), 504 (sh), 627 (4.61)	794
RuL5^{2+}	292 (5.15), 358 (1.14), 476 (2.02), 632 (4.76)	-
RuL6^{2+}	292 (5.72), 353 (1.33), 489 (2.09), 646 (5.32)	-

2.2.3 Computational Analysis

Density functional theory analysis was carried out on all ruthenium and iridium complexes to gain insight into their electronic structure and, via TDDFT, frontier orbital contributions to their electronic absorption spectra. It should be noted that quantitative data collected is subject to change based on the basis set(s) used in computations.[23] As such, all quantitative information derived from DFT MO analyses is not absolute and instead should be treated as an additional tool used in interpretation of the spectroscopic and electrochemical behavior of the complexes. As the $[Ru(bpy)_3]^{2+}$ system is a well-established benchmark for ruthenium polypyridyl complexes it is also included here reference alongside the $[Ru(OQN)(bpy)_2]^+$ **RuL1**$^+$ which has been previously investigated by Rochford and co-workers. The tris-bipyridyl $[Ru(bpy)_3]^{2+}$ chromophore possesses D_3 symmetry and is stabilized primarily by Ru–N σ-bonding with negligible π-bonding between the metal center and ligand set.[24] It exhibits a reasonably strong ($\varepsilon = 1.46 \times 10^4$ M^{-1} cm^{-1}) visible absorption maximum in acetonitrile at 450 nm attributed to a singlet metal-to-ligand charge-transfer (^{1}MLCT) electronic transition. The HOMO level of $[Ru(bpy)_3]^{2+}$ is computed to be primarily Ru *d*-based (82%) with limited contribution from the six bpy N-donor atoms (18%). In contrast, its LUMO level is equally distributed among the

three bpy lowest energy π* levels. The lowest energy HOMO→LUMO electronic transition however has a very weak oscillator strength (f = 0.002) and merely contributes to the lower energy tail of its visible absorption band (calc. λ_{max} = 479 nm). Its maximum visible absorption band is primarily derived from the near degenerate H-1→LUMO (calc. λ_{max} = 438 nm, f = 0.021) and H-2→LUMO (calc. λ_{max} = 437 nm, f = 0.021) electronic transitions (Fig. A33, Table A1). Introduction of the simple oxyquinolate ligand **L1**$^-$ in the $[Ru(OQN)(bpy)_2]^+$ complex (**RuL1**$^+$) has a dramatic impact on its electronic structure and absorption spectrum relative to $[Ru(bpy)_3]^{2+}$. Its lower C_1 symmetry results in a breakdown of degeneracy in its frontier orbitals while the oxyanion contributes not only as a σ-donor but is also heavily involved in π-bonding with the Ru d-manifold destabilizing the HOMO level by 1.11 eV relative to $[Ru(bpy)_3]^{2+}$ (Table 2.2). This Ru(dπ)−OQN(π) interaction is responsible for a strong non-innocent character of the oxyquinolate class of ligands at Ru(II) which can be visualized in the corresponding bonding (H-3) and antibonding (HOMO) pair of occupied frontier molecular orbitals of **RuL1**$^+$ (Figure 2.3). Covalent mixing of the Ru d(π)–OQN(π) frontier orbitals is confirmed by Mulliken population analysis with Ru:OQN contributions of 39%:54% at the HOMO level and 41%:49% at the HOMO-3 level. Even with a slight destabilization of the LUMO level in **RuL1**$^+$ relative to $[Ru(bpy)_3]^{2+}$ (+0.3 eV) the HOMO−LUMO energy gap is significantly narrowed (2.65 eV vs. 3.24 eV, respectively) although its contribution to the electronic absorption spectrum of **RuL1**$^+$ remains minimal, again at the tail end of the spectrum (calc. λ_{max} = 615 nm, f = 0.0041). In contrast to $[Ru(bpy)_3]^{2+}$, **RuL1**$^+$ exhibits two distinct broad visible absorption maxima of comparable

intensity in acetonitrile at 400 nm (ε = 0.77 x 10^4 M^{-1} cm^{-1}) and 496 nm (ε = 1.21 x 10^4 M^{-1} cm^{-1}). Due to the decreased symmetry of **RuL1**$^+$ its panchromatic visible absorption is derived from a wide range of contributing electronic transitions of varying oscillator strengths too lengthy to detail here, hence the reader is referred to Table A2 for reference. It is worth stating however that these broad visible absorption bands are each comprised of a mixture of both traditional ^{1}MLCT and electronic transitions (H-1/H-2 →LUMO/L+1/L+2), and also non-traditional singlet (metal-ligand)-to-ligand charge-transfer (^{1}MLLCT) electronic transitions originating from the hybrid Ru *d*(π)−OQN(π) HOMO or H-3 levels to both bpy(π*) (LUMO/L+1) and OQN(π*) (L+2) orbitals.

Table 2.2 Mulliken population analysis (%) and computed energies (eV) of frontier molecular orbitals for $[Ru(bpy)_3]^{2+}$ and complexes **RuL1**$^+$ **- RuL6**$^{2+}$.

Complex	orbital	Ru (%)	L1 – L6 (%)	bpy (total %)	Energy (eV)
$[Ru(bpy)_3]^{2+}$	LUMO	0	N/A	100	-2.90
	HOMO	82	N/A	18	-6.14
	H-1	74	N/A	26	-6.33
	H-2	74	N/A	26	-6.33
RuL1$^+$	L+2	4	91	5	-2.03
	L+1	8	1	91	-2.49
	LUMO	4	3	93	-2.60
	HOMO	39	54	7	-5.25
	H-1	75	8	17	-5.63

	H-2	73	9	18	-5.86
	H-3	41	49	10	-6.32
RuL2^{2+}	L+2	7	1	92	-2.45
	L+1	4	3	93	-2.53
	LUMO	1	97	2	-2.90
	HOMO	27	69	4	-5.41
	H-1	77	7	16	-5.80
	H-3	51	38	11	-6.25
RuL3^{2+}	LUMO	1	98	1	-3.09
	HOMO	30	66	4	-5.49
	H-3	48	41	11	-6.30
RuL4^{2+}	LUMO	1	98	1	-3.14
	HOMO	26	69	5	-5.44
	H-3	51	39	10	-6.26
RuL5^{2+}	LUMO	1	96	3	-3.12
	HOMO	22	74	4	-5.60
	H-1	76	7	17	-5.90
	H-3	52	38	10	-6.32
RuL6^{2+}	LUMO	1	97	2	-3.12
	HOMO	26	70	4	-5.55
	H-1	77	7	16	-5.89

H-3	41	51	8	-6.19

Complexes **RuL2**$^{2+}$ - **RuL6**$^{2+}$ exhibit similar non-innocent covalent bonding character at the HOMO and H-3 levels due to mixing of the Ru d(π) and OQN(π) orbitals. The LUMO levels of **RuL2**$^{2+}$ - **RuL6**$^{2+}$ however, are now situated on the low energy cationic electron-accepting merocyanine π* orbitals, further narrowing the HOMO-LUMO energy gap relative to **RuL1**$^{+}$.

High energy transitions in these complexes range from 410-490 nm and consist primarily of H-3→LUMO with contributions reaching upwards of ~70%. Calculated MO surfaces show significant Ru(dπ)→OQN(π) overlap for H-3 and is supported by Ru 41-53% and OQN 37-50% population analysis results. The increase in OQN percentages for the HOMO and H-3 is recognized as the result of an increase in size of the molecular orbitals as seen with their MO surfaces and independent of the increased withdrawing character generated from the merocyanine π acceptors. Such withdrawing character can be attributed to a decrease in splitting of the HOMO and H-3 from **RuL1**$^{+}$ (1.07 eV) to **RuL2**$^{2+}$-**RuL6**$^{2+}$ averaging ~0.77 eV between their orbitals. Unlike **RuL1**$^{+}$, there is a large overlap of electron density of both these orbitals with the LUMO (Ru 1%, OQN 96-98%), consistent with a donor-π-acceptor framework. Low energy transitions of these complexes are attributed to (ML)LCT electronic transitions based on the subsequent information. **RuL2**$^{2+}$-**RuL4**$^{2+}$ all exhibit a single transition from 568 - 605 nm which consist of >73% the HOMO→LUMO as contribution. MO surfaces show significant overlap of electron density between the Ru(dπ)-OQN(π) based HOMO's (Ru 21-25%, OQN 72-76%) and the mer(π*) dominated LUMO's (Ru 1%, OQN 97-98%). **RuL2**$^{2+}$

additionally has three more low energy transitions at 552 nm (HOMO→LUMO 11%, HOMO→L+1 19%, HOMO→L+2 55%), 535 nm (H-1→L+2 14%, HOMO→LUMO 20%, HOMO→L+1 27%, HOMO→L+2 24%) and 523 nm (H-1→LUMO 87%) respectively. These (ML)LCT transitions are primarily [Ru(dπ)-OQN(π)]→bpy(π*) in character resembling the HOMO→LUMO transition in **RuL1**$^{+}$. This is further corroborated by the L+1 and L+2 orbitals having 92-93% bpy and just 4-7% Ru character. **RuL5**$^{2+}$ and **RuL6**$^{2+}$ exhibit not one, but 2 low energy transitions in their TDDFT data. Transitions at 563-567 nm (H-1→LUMO 61-82%) and 581-588 nm (HOMO→LUMO 58-79%) exist within ~20 nm of one another and make up the low energy transitions of these complexes. The H-1 orbitals (Ru 76-77%, OQN 7%, bpy 16-17%) contain very little oxyquinolate character and as such, contributes a more metal-centered occupied orbital to these low energy transitions. The TDDFT data provided were found to be in good agreement with the experimental spectra.

The indole, **RuL5**$^{2+}$, and benzoindole, **RuL6**$^{2+}$, complexes while similar, do not exhibit the exact same makeup of their two low energy absorption bands. In the case of **RuL5**$^{2+}$, the first of these two absorptions is observed at 476 nm (20,200 M^{-1} cm^{-1}) and is composed of both H-3→LUMO and HOMO→L+3 electronic transitions. The HOMO→L+3 character is unique in that it is an observable example of a [Ru(dπ)-mer(π)]→[bpy(π*)-Ru(d*)-mer(π*)] electronic transition. For **RuL6**$^{2+}$, the absorption band at 489 nm (20,900 M-1 cm-1) is found to consist of character both from the H-3→LUMO (465 nm) ^{1}(ML)LCT and the H-2→L+1 (451 nm) ^{1}MLCT electronic transitions. Thus, it can be stated that **RuL6**$^{2+}$ is distinctive amongst the rest of the merocyanine complexes based on a considerable contribution to one of its absorption

bands from a Ru(d)→bpy(π*) transition similar to those in $[Ru(bpy)_3]^{2+}$. At 631 nm (47,500 M-1 cm-1) and 645 nm (53,200 M^{-1} cm^{-1}) respectively, **RuL5**$^{2+}$-**RuL6**$^{2+}$ exhibit the strongest and most red-shifted low energy absorption bands of the ruthenium complexes studied. Both absorption bands consist of HOMO→LUMO and uniquely, H-1→LUMO electronic transitions. As with the prior merocyanine complexes, absorption of **RuL5**$^{2+}$-**RuL6**$^{2+}$ tail out to ~800 nm. A detailed description of the emission of these complexes is given below.

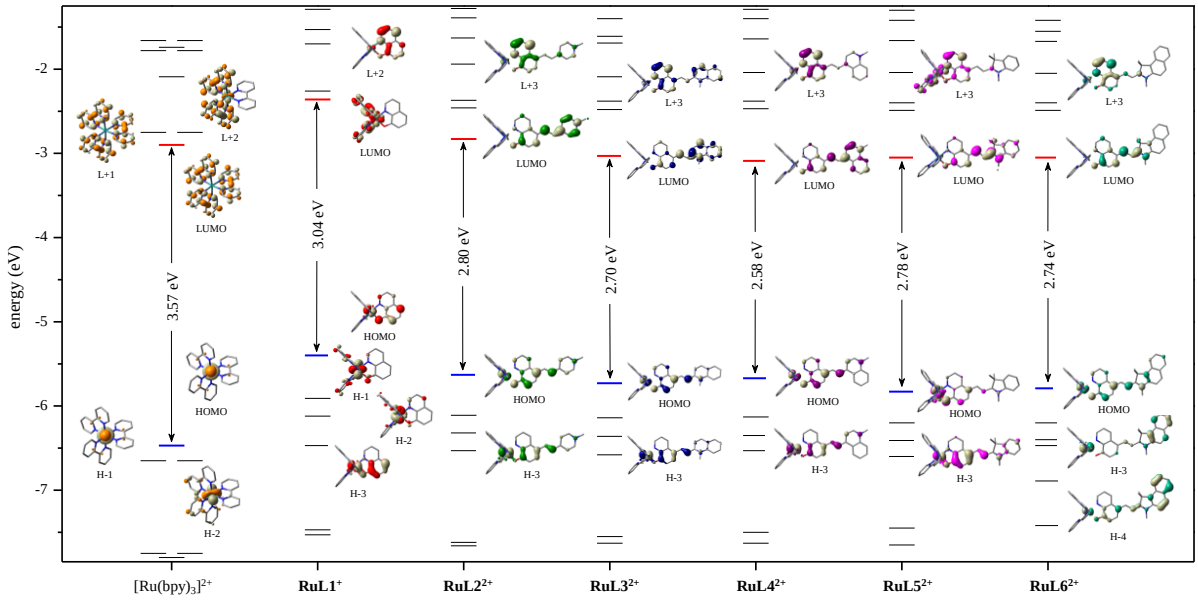

Figure 2.3. Plot of frontier molecular orbital energy levels (eV) for complexes $[Ru(bpy)_3]^{2+}$ - **RuL6**$^{2+}$ as calculated by DFT/B3PW91/6-31G(d,p) (H,C,N,O) and SDD (Ru) in an acetonitrile polarizable continuum model. Electron occupancy is removed for clarity, and HOMO-LUMO levels are highlighted in blue and red respectively. Select frontier molecular orbital surfaces (isofactor = 0.04) are included for comparison.

2.2.4 Electrochemistry

The electrochemical properties of all complexes were investigated by cyclic voltammetry in an acetonitrile electrolyte and their data are summarized in Table 2.3. Voltammograms of all complexes are additionally provided in Figure 2.4 to illustrate the redox properties of the merocyanine ligands and their effects on the ruthenium core. The reference complex $[Ru(bpy_3)]^{2+}$ has been extensively studied in previous literature and its electrochemical properties are well established.[R] In positive scans a reversible oxidation event occurs at 0.89 V vs $Fc^{+/0}$ indicative of the Ru(III/II) couple. Scanning in the negative direction exhibits three reversible reduction events at -1.65, -1.83 and -2.10 V vs $Fc^{+/0}$, consistent with reduction of the π* orbitals of each bpy ligand. It can be argued that the increase in potential for the reduction of each bpy ligand is a result of the coulombic effect of reducing the ruthenium complex from a charge of 2+ to 1+ and so on with each event. An irreversible potential at E^o = -2.71 V is also observed and attributed to a second electron reduction of one of the bpy ligands. The study of **RuL1**$^+$ exhibits a cathodic shift in the $Ru^{(III/II)}$ couple consistent with destabilization of the HOMO and its covalency to the HOMO-3 orbital. This complex differs however in that unlike the Ru(III/II) couple present in $[Ru(bpy_3)]^{2+}$, this couple is assigned to the oxidation/reduction of the Ru(dπ)-OQN(π) HOMO. Further confirmation of this trend can be exhibited by the red-shifted electronic spectra of these complexes. A second, irreversible anodic potential at E° = +1.02 V is observed and is most likely the oxidation of the singly occupied Ru(dπ)-OQN(π) orbital of the complex's dicationic derivative. Scanning with a negative potential bias, two reversible redox events at E° = -1.88 and -2.13 V are measured.

These couples are confirmed by DFT as the reduction/oxidations of the two bpy(π*) unoccupied molecular orbitals and can be considered isoelectronic to the $[Ru(bpy_3)]^{+1/0}$ and $[Ru(bpy_3)]^{0/-1}$ couples of the first reference complex. Third and fourth, irreversible reductions at E° = -2.79 and -2.92 V were recorded and believed to be similar second electron reduction of the π* orbital of one of the bpy ligands as with $[Ru(bpy_3)]^{-1/-2}$ and a reduction of the OQN(π*) orbital respectively.

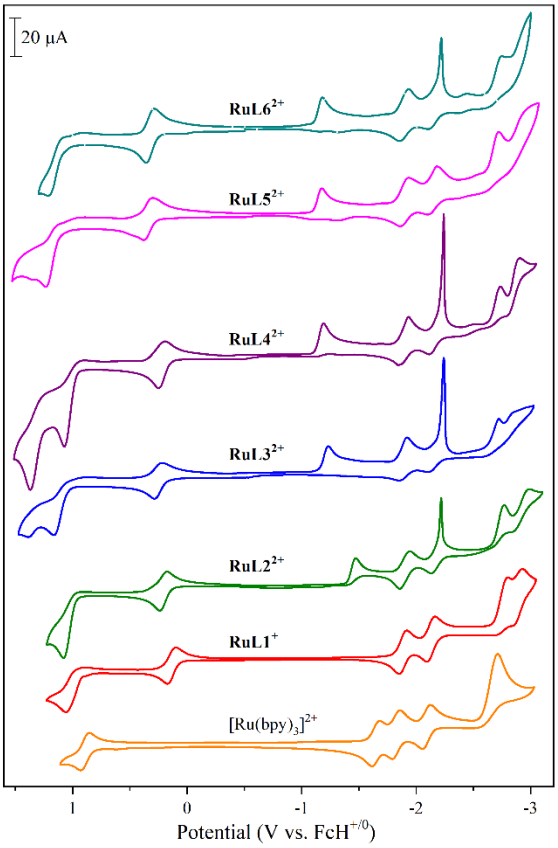

Figure 2.4. Cyclic voltammetry for complexes $[Ru(bpy)_3]^{2+}$ - **RuL6^{2+}** recorded in acetonitrile with 0.1 M $[Bu_4N][PF_6]$ supporting electrolyte at a glassy carbon electrode with a scan rate of υ = 0.1 V s^{-1}.

While complexes **RuL2**$^{2+}$-**RuL6**$^{2+}$ do not experience the same coulombic effect as **RuL1**$^{+}$ they still exhibit prominent cathodic shifts to their Ru-OQN$^{+3/+2}$ couples. This trend supports that this cathodic shift is independent of the complex's overall oxidation state and instead tied directly to the oxidation state of the Ru(dπ)-OQN(π) molecular orbital. A decrease in the magnitude of this shift is observed when compared to **RuL1**$^{+}$ and is likely a result of the withdrawing character of the merocyanine ligands. Abstraction of electron density away from the symmetry assisted ligand coupled (SALC) orbital, results in a weakening of the NIL effect. The destabilization/stabilization of the HOMO/HOMO-3 orbital pair is reduced and the HOMO orbitals of **Ru3**$^{2+}$-**Ru7**$^{2+}$ are more positive. Upon reduction of the merocyanine complexes, an irreversible potential between -1.17 and -1.46 eV was recorded and attributed to the reduction of the mer(π*) and is corroborated by TD-DFT surfaces of their LUMO orbitals. Variation in these potentials appears to be directly correlated to the strength of the π acceptors of each of the merocyanine complexes and follow a similar trend in cathodic shifts to their Ru-OQN$^{+3/+2}$ couples. As with **RuL2**$^{+}$, two sets of reversible potentials at -1.87 to -1.90 and -2.15 to -2.18 respectively, exhibiting the redox chemistry bpy π* orbitals. Uniquely, **RuL2**$^{2+}$-**RuL4**$^{2+}$ and **RuL6**$^{2+}$ exhibit sharp, non-gaussian peaks obfuscating the second bpy reductions, indicating the adsorption of an electrochemical product onto the surface of the working electrode. The same types of events are additionally observed in the reverse scan when setting the switching potential to just beyond the first reversible reduction event. Because of this, the product that adsorbs onto the surface of the electrode is believed to be generated during or after the irreversible reduction of the mer(π*). For reasons not yet understood, it should be noted that **RuL5**$^{+}$ does not exhibit an adsorption based potential in either the initial negative

or reverse scans. Beyond that, **RuL2^{2+}-RuL6^{2+}** exhibit either one or two more irreversible potentials from -2.72 to -2.99 V and are likely to coincide with additional bpy(π*) and OQN(π*) reduction events.

Table 2.3. Electrochemical data complexes $[Ru(bpy)_3]^{2+}$ - **RuL6^{2+}** and recorded in acetonitrile with 0.1 M $[Bu_4N][PF_6]$ supporting electrolyte.

	$E^{\circ\prime}$ (V vs $FcH^{+/0}$)							
$[Ru(bpy)_3]^{2+}$			0.89	-1.65	-1.83	-2.10	-2.71[a]	
RuL1^{+}		1.06[a]	0.14	-1.88	-2.13	-2.79[a]	-2.92[a]	
RuL2^{2+}		1.08[a]	0.21	-1.46[a]	-1.90[b]	-2.18[b]	-2.77[a]	-2.99[a]
RuL3^{2+}	1.39[a]	1.16[a]	0.26	-1.23[a]	-1.87[b]	-2.18[b]	-2.72[a]	
RuL4^{2+}	1.37[a]	1.08[a]	0.23	-1.19[a]	-1.88[b]	-2.18[b]	-2.73[a]	-2.91[a]
RuL5^{2+}	1.37[a]	1.23[a]	0.34	-1.17[a]	-1.90	-2.15	-2.72[a]	
RuL6^{2+}		1.20[a]	0.32	-1.18[a]	-1.90[b]	-2.16[b]	-2.75[a]	

[a] irreversible. [b] exhibits chemical adsorption on the working electrode.

2.3 Conclusions

A total of five ruthenium(II) complexes with different ligands built around the 5-(vinyl-cyanine)-8-oxyquinolate scaffold were successfully synthesized in appropriate yields and their photophysical and electrochemical properties were studied. Low energy absorption bands with strong extinction coefficients as high as 5.32 ε x 10^4 M^{-1} cm^{-1} were observed and reported to trail into the near infrared region of the electronic spectrum as far as ~800 nm. These absorption

bands were confirmed by TD-DFT to be primarily the result of the HOMO-LUMO electronic transitions from a Ru(dπ) based orbital into the low lying mer(π*) orbitals. The minimal emission of these complexes, even at 77 K was argued to be the result of freedom of rotation of their excited states, resulting in almost entirely vibration relaxation from these states. As it stands, these complexes offer attractive properties for future studies as photosensitizers in a variety of techniques across several disciplines of chemistry.

2.4 Experimental Section

2.4.1 Physical Measurements

UV−vis−NIR absorption spectra were recorded on an Agilent 8453 diode array spectrophotometer in spectrophotometric grade acetonitrile. NMR spectra were recorded on an Agilent spectrometer operated at 399.80 MHz for ^{1}H, and 100.54 MHz for ^{13}C. Deuterated solvents *d*-chloroform, d_6-acetone, and d_6-dimethyl sulfoxide were used as received from Aldrich and their residual ^{1}H solvent signals (δ = 7.26, 2.05, and 2.50 ppm respectively) used as internal references for reporting the ^{1}H chemical shift (δ).[26] Likewise, the ^{13}C signal of d_6-dimethyl sulfoxide (δ = 39.52 ppm) was used as an internal reference for reporting ^{13}C NMR spectra. ESI-MS was carried out on a Thermo Finnigan mass spectrometer. Cyclic voltammetry was carried out on a CH Instruments 620D potentiostat. A standard three electrode cell was used under an atmosphere of argon with 0.1 M Bu_4NPF_6 in spectrophotometric grade acetonitrile as supporting electrolyte. Glassy carbon (3 mm diameter) and Pt wire were used as working and counter electrodes, respectively. A nonaqueous reference electrode was used to minimize ohmic potential drop at the solvent

interface. This consisted of a Ag wire in 0.1 M Bu_4NPF_6 acetonitrile supporting electrolyte isolated by a vycor frit and was calibrated using the ferricenium/ferrocene redox couple as a pseudoreference (+0.45 V vs SCE).[citation] Redox potentials (E) were determined from cyclic voltammetry as $(E_{pa} + E_{pc})/2$, where E_{pa} and E_{pc} are the anodic and cathodic peak potentials, respectively. Where E could not be calculated due to irreversible behavior, E_{pc} or E_{pa} are reported accordingly.

2.4.2 Computational Details

All calculations were carried out using density functional theory (DFT) with the B3PW91 functional and acetonitrile polarizable continuum model (PCM)[27] as implemented in the Gaussian 09 B.01 program package.[28] The Stuttgart/Dresden relativistic effective core potential (SDD) basis set was used for Ru[29] and 6-31G(d,p)[30,31] for C, H, N, O, S. A vibrational frequency analysis was carried out in order to confirm the minimum-energy geometry and determine the zero-point energy for each species; i.e., geometry optimization and frequency calculations were performed for both the native **3**−**7**$^{2+}$ complexes and their one-electron oxidized derivatives **3**−**7**$^{3+}$. Electronic transitions (N = 60) were calculated in acetonitrile with the PCM optimized geometry using time-dependent density functional theory (TDDFT)[32] at the same level of theory. Successful implementation of these DFT/TDDFT parameters has proven successful in the past for ruthenium polypyridyl complexes.[33]

2.4.3 Synthetic Procedures

Materials. 4-Methylpyridine, 4-methylquinoline, 2-methylquinoline, 2,3,3-trimethyl-3H-indole, 1,2,2-trimethyl-1H-benzo[E]indole, iodomethane, piperidine, triethylamine and spectroscopic grade acetonitrile were purchased from Aldrich and used as received. 8-Hydroxyquinoline-5-carbaldehyde was purchased from OxChem and used as received. Potassium hexafluorophosphate was purchased from Strem and used as received. Reagent grade acetonitrile, hexanes, 2-propanol, diethyl ether, methanol and acetone were purchased from Pharmco Aaper and used as received. Tetrabutyl ammonium hexafluorophosphate (Sigma) was recrystallized thrice from hot ethanol and dried under vacuum prior to use. The complexes $Ru(bpy)_2Cl_2$,[34] $[Ru(bpy)_3](PF_6)_2$,[35] and $[Ru(bpy)_2(OQN)](PF_6)_2$,[34] were prepared according to the literature.

General Procedure for Synthesis of Cyanine Pi Acceptors. A 10 mL microwave vial was charged with the corresponding tertiary amine (1 mmol), iodomethane (1.2 mmol) and reagent grade acetonitrile (4 mL). The mixture was refluxed in the microwave at 102 °C for 15 minutes. Upon completion, the resulting mixture was transferred to a round bottom flask and acetonitrile was removed under reduced pressure and the remaining solid was sonicated and suspended in hexanes. Analytically pure compound was isolated by vacuum filtration, washing with hexanes and allowing to air dry. Yields typically ranged from 70-90%.

*1,4-Dimethylpyridin-1-ium iodide (**P3**)*. ^{1}H NMR $\delta[(CD_3)_2SO]$: 2.59 (s, 3H), 4.28 (s, 3H), 7.96 (d, 2H), 8.83 (d, 2H).

*1,2-Dimethylquinolin-1-ium iodide (**P4**)*. ^{1}H NMR δ[$(CD_3)_2SO$]: 3.08 (s, 3H), 4.45 (s, 3H), 7.99 (dd, 1H), 8.12 (d, 1H), 8.23 (m, 1H), 8.40 (dd, 1H), 8.59 (d, 1H), 9.1 (d, 1H).

*1,4-Dimethylquinolin-1-ium iodide (**P5**)*. ^{1}H NMR δ[$(CD_3)_2SO$]: 3.01 (s, 3H), 4.58 (s, 3H), 8.07 (m, 2H), 8.27 (m, 1H), 8.49 (d, 1H), 8.54 (dd, 1H), 9.36 (d, 1H).

*1,2,3,3-Tetramethyl-3H-indol-1-ium iodide (**P6**)*. ^{1}H NMR δ[$(CD_3)_2SO$]: 1.52 (s, 6H), 2.78 (s, 3H), 3.97 (s, 3H), 7.62 (m, 2H), 7.83 (m, 1H), 7.91 (m, 1H).

*1,1,2,3-Tetramethyl-1H-benzo[e]indol-3-ium iodide (**P7**)*. ^{1}H NMR δ[$(CD_3)_2SO$]: 1.75 (s, 6H), 2.88 (s, 3H), 4.10 (s, 3H), 7.75 (m, 2H), 8.11 (d, 1H), 8.22 (d, 1H), 8.29 (d, 1H), 8.37 (d, 1H).

General Procedure for Synthesis of Merocyanine Ligands. A 10 mL microwave vial was charged with 8-hydroxyquinoline-5-carbaldehyde (100 mg, 0.58 mmol), the corresponding pi acceptor (0.56 mmol), piperidine (0.57 mmol) and 2-propanol (4 mL). The mixture was refluxed in the microwave at 102 °C for 15 minutes. Upon completion, the resulting mixture was added to a flask charged with diethyl ether (30 mL) and the solid precipitate was collected by vacuum filtration. The solid was then dissolved in a 1:1 acetone: water mixture (15 mL) and to it was added KPF_6 (0.6 mmol in 10 mL water). Acetone was removed under reduced pressure and the resulting solid was collected by vacuum filtration. Analytically pure compounds were collected by recrystallization from acetone/diethyl ether.

*(E)-4-(2-(8-Hydroxyquinolin-5-yl)vinyl)-1-methylpyridin-1-ium hexafluorophosphate (**L3**)*. ^{1}H NMR δ[$(CD_3)_2SO$]: 4.25 (s, 3H), 7.24 (d, 1H), 7.52 (d, J = 16 Hz, 1H), 7.72 (m, 1H), 8.17 (d, 1H), 8.35 (d, 2H), 8.69 (d, J = 16 Hz, 1H), 8.84 (d, 2H), 8.95 (dd, 1H), 9.08 (dd, 1H). ^{13}C

NMR $\delta[(CD_3)_2SO]$: 46.76, 111.96, 122.34, 122.58, 123.38, 127.00, 127.54, 132.51, 135.69, 138.25, 144.85, 148.57, 152.78, 156.17.

General Procedure for Synthesis of Ruthenium Complexes. A 10 mL microwave vial was charged with $Ru(bpy)_2Cl_2$ (100 mg, 0.206 mmol), the corresponding merocyanine ligand (0.206 mmol), triethylamine (2.1 mmol) and methanol (4 mL). The reaction mixture was then refluxed in the microwave at 120 °C for 15 minutes. The resulting mixture was quantitatively transferred to an aqueous solution of KPF_6 (2.1 mmol in 15 mL) and methanol was removed under reduced pressure. The precipitate that formed was collected by vacuum filtration and analytically pure product was obtained by recrystallization from acetone/diethyl ether.

*$[Ru(bpy)_2(P\text{-}Py\text{-}OQN)][2PF_6]$ (**RuL2**$^{2+}$)*. ESI-MS $[M\text{-}PF_6^-]^+$: calcd 821.12; found 821.0260. $[M\text{-}2PF_6^-]^{+2}$: calcd 338.075; found 338.0764.

*$[Ru(bpy)_2(O\text{-}Qn\text{-}OQN)][2PF_6]$ (**RuL3**$^{2+}$)* (73% Yield). ^{1}H NMR $\delta[(CD_3)_2SO]$: 9.00-8.95 (m, 2H), 8.81-8.69 (m, 7H), 8.47 (dd, 2H), 8.26 (d, 2H, J = _ Hz), 8.19-8.02 (m, 7H), 7.97 (d, 1H), 7.89-7.76 (m, 3H), 7.70 (dd, 1H), 7.55-7.43 (m, 4H), 6.99 (d, 1H, J = _ Hz), 4.66 (s, 3H). ESI-MS $[M\text{-}PF_6^-]^+$: calcd 871.13; found 870.9586. $[M\text{-}2PF_6^-]^{+2}$: calcd 363.085; found 363.0822.

*$[Ru(bpy)_2(P\text{-}Qn\text{-}OQN)][2PF_6]$ (**RuL4**$^{2+}$)*. $\delta[(CD_3)_2SO]$: 4.63 (s, 3H), 6.99 (d, 1H, J = _ Hz), 7.46-7.42 (m, 3H), 7.51 (dd, 1H), 7.69 (dd, 1H), 7.74 (d, 1H), 7.94 (d, 1H), 7.99 (dd, 1H), 8.08-8.03 (m, 2H), 8.25-8.11 (m, 6H), 8.42 (d, 1H, J = _ Hz), 8.52 (dd, 2H), 8.72 (d, 2H), 8.81-8.75 (m, 3H), 8.97-8.90 (m, 2H), 9.02 (d, 2H). ESI-MS $[M\text{-}PF_6^-]^+$: calcd 871.13; found 870.9118. $[M\text{-}2PF_6^-]^{+2}$: calcd 363.085; found 363.0829.

*[Ru(bpy)$_2$(Ind-OQN)][2PF$_6$] (**RuL5**$^{2+}$)* (68% Yield). δ[(CD$_3$)$_2$SO]: 1.92 (d, 6H), 4.11 (s, 3H), 7.04 (d, 1H, *J* = _ Hz), 7.60-7.45 (m, 7H), 7.76-7.67 (m, 3H), 7.85 (d, 1H), 7.99 (d, 1H), 8.22-8.06 (m, 6H), 8.64 (d, 1H, *J* = _ Hz), 8.94-8.70 (m, 7H). ESI-MS [M-PF$_6^-$]$^+$: calcd 887.16; found 886.9918. [M+2H$^+$-mer-PF$_6^-$]$^+$: calcd 586.12; found 585.9591. [M-2PF$_6^-$]$^{+2}$: calcd 371.1; found 371.0977.

*[Ru(bpy)$_2$(Bin-Py-OQN)][2PF$_6$] (**RuL6**$^{2+}$)*. ESI-MS [M-PF$_6^-$]$^+$: calcd 937.18; found 937.1175. [M+2H$^+$-mer-PF$_6^-$]$^+$: calcd 586.12; found 585.9574. [M-2PF$_6^-$]$^{+2}$: calcd 396.11; found 396.1090.

2.6 References

(1) Broere, D. L. J.; Plessius, R.; van der Vlugt, J. I. *Chem. Soc. Rev.* **2015**, *44*, 6886-6915.

(2) Luca, O. R.; Crabtree, R. H. *Chem. Soc. Rev.* **2013**, *42*, 1440-1459.

(3) Boyer, J. L.; Rochford, J.; Tsai, M. K.; Muckerman, J. T.; Fujita, E. *Coord. Chem. Rev.* **2010**, *254*, 309-330.

(4) Bellinger-Buckley, S.; Chang, T.; Bag, S.; Schweinfurth, D.; Zhou, W.; Torok, B.; Sarkar, B.; Tsai, M.; Rochford, J. *Inorg. Chem.* **2014**, *53*, 5556-5567.

(5) Ngo, K. T.; Lee, N. A.; Pinnace, S. D.; Szalda, D. J.; Weber, R. T.; Rochford, J. *Inorg. Chem.* **2016**, *55*, 2460-2472.

(6) Kaim, W. *Inorg. Chem.* **2011**, *50*, 9752-9765.

(7) Kaim, W. *Eur. J. Inorg. Chem.* **2012**, *2012*, 343-348.

(8) Ingram, J. D.; Costa, P. J.; Adams, H.; Ward, M. D.; Felix, V.; Thomas, J. A. *Inorg. Chem.* **2012**, *51*, 10483-10494.

(9) Zhao, H. C.; Fu, B.-L.; Schweinfurth, D.; Harney, J. P.; Sarkar, B.; Tsai, M.-K.; Rochford, J. *Eur. J. Inorg. Chem.* **2013**, *2013*, 4410−4420.

(10) Mandal, A.; Grupp, A.; Schwederski, B.; Kaim, W.; Lahiri, G. K. *Inorg. Chem*. **2015**, *54*, 10049−10057.

(11) Laine, T. M.; Karkas, M. D.; Liao, R.-Z.; Siegbahn, P. E. M.; Akermark, B. *Chem. - Eur. J.* **2015**, *21*, 10039−10048.

(12) Weisser, F.; Plebst, S.; Hohloch, S.; van der Meer, M.; Manck, S.; Führer, F.; Radtke, V.; Leichnitz, D.; Sarkar, B. *Inorg. Chem*. **2015**, *54*, 4621−4635.

(13) Zhang, Y.; Zhou, Q.; Tian, N.; Li, C.; Wang, X. *Inorg. Chem.* **2017**, *56*, 4, 1865-1873.

(14) Tomasulo, M.; Sortino, S.; Raymo, M. *J. Org. Chem.* **2008**, *73*, 118-126.

(15) Ito, M.; Matsumura, K. *Notes* **1958**, *23*, 86-88.

(16) Faller, J. W.; Mueller, A.; Phillips, J. P. *Notes* **1964**, *29*, 3450-3452.

(17) Kovtun, Y. P.; Prostota, Y. O.; Tolmachev, A. I. *Dyes and Pigments* **2003**, *58*, 83-91.

(18) Juris, A.; Balzani, V.; Barigelletti, F.; Campagna, S.; Belser, P.; Vonzelewsky, A. *Coord. Chem. Rev.* **1988**, *84*, 85-277.

(19) Damrauer, N. H.; Cerullo, G.; Yeh, A.; Boussie, T. R.; Shank, C. V.; McCusker, J. K. *Science* **1997**, *275*, 54-57.

(20) O'Donnell, R. M.; Johannson, P. G.; Abrahamsson, M.; Meyer, G. J. *Inorg. Chem.* **2013**, *52*, 6839-6848.

(21) Kober, E. M.; Meyer, T. J. *Inorg. Chem.* **1982**, *21*, 3967-3977.

(22) Caspar, J. V.; Meyer, T. J. *J. Phys. Chem.* **1983**, *87*, 952-957.

(23) Philips, J. J.; Hudspeth, M. A.; Browne, P. M., Jr.; Peralta, J. E. *Chem. Phys. Lett.* **2010**, *495*, 146−150.

(24) Daul, C.; Baerends, E. J.; Vernooijs, P. *Inorg. Chem.* **1994**, *33*, 3538-3543.

(25) A. Juris, V. Balzani, F. Barigelletti, S. Campagna, P. Belser and A. von Zelewsky, Coord. Chem. Rev., 1988, 84, 85–277.

(26) Fulmer, G. R.; Miller, A. J. M.; Sherden, N. H.; Gottlieb, H. E.; Nudelman, A.; Stoltz, B. M.; Bercaw, J. E.; Goldberg, K. I. *Organometallics*, **2010**, *29*, 2176-2179.

(27) Tomasi, J.; Mennucci, B.; Cammi, R. *Chem. Rev*. **2005**, *105*, 2999−3093.

(28) Frisch, M. J.; et al. *Gaussian 09, Revision A.1*; Gaussian Inc.: Wallingford, CT, 2009.

(29) Fredin, L. A.; Allison, T. C. *J. Phys. Chem. A* 2016, 120, 13, 2135–2143.

(30) Harihara, Pc; Pople, J. A. *Theor. Chim. Acta* **1973**, *28*, 213−222.

(31) Francl, M. M.; Pietro, W. J.; Hehre, W. J.; Binkley, J. S.; Gordon, M. S.; Defrees, D. J.; Pople, J. A. *J. Chem. Phys.* **1982**, *77*, 3654−3665.

(32) Scalmani, G.; Frisch, M. J.; Mennucci, B.; Tomasi, J.; Cammi, R.; Barone, V. *J. Chem. Phys*. **2006**, *124*, 94107.

(33) Hu, K.; Severin, H. A.; Koivisto, B. D.; Robson, K. C. D.; Schott, E.; Arratia-Perez, R.; Meyer, G. J.; Berlinguette, C. P. *J. Phys. Chem. C* **2014**, *118*, 17079−17089.

(34) Sullivan, B. P.; Salmon, D. J.; Meyer, T. J. *Inorg. Chem.* **1978**, *17*, 3334−3341.

(35) Browne, W. R.; Passaniti, P.; Gandolfi, M. T.; Ballardini, R.; Henry, W.; Guckian, A.; O'Boyle, N.; McGarvey, J. J.; Vos, J. G. *Inorg. Chim. Acta* **2007**, *360*, 1183−1190.

APPENDIX

A. NMR AND MASS SPEC. DATA

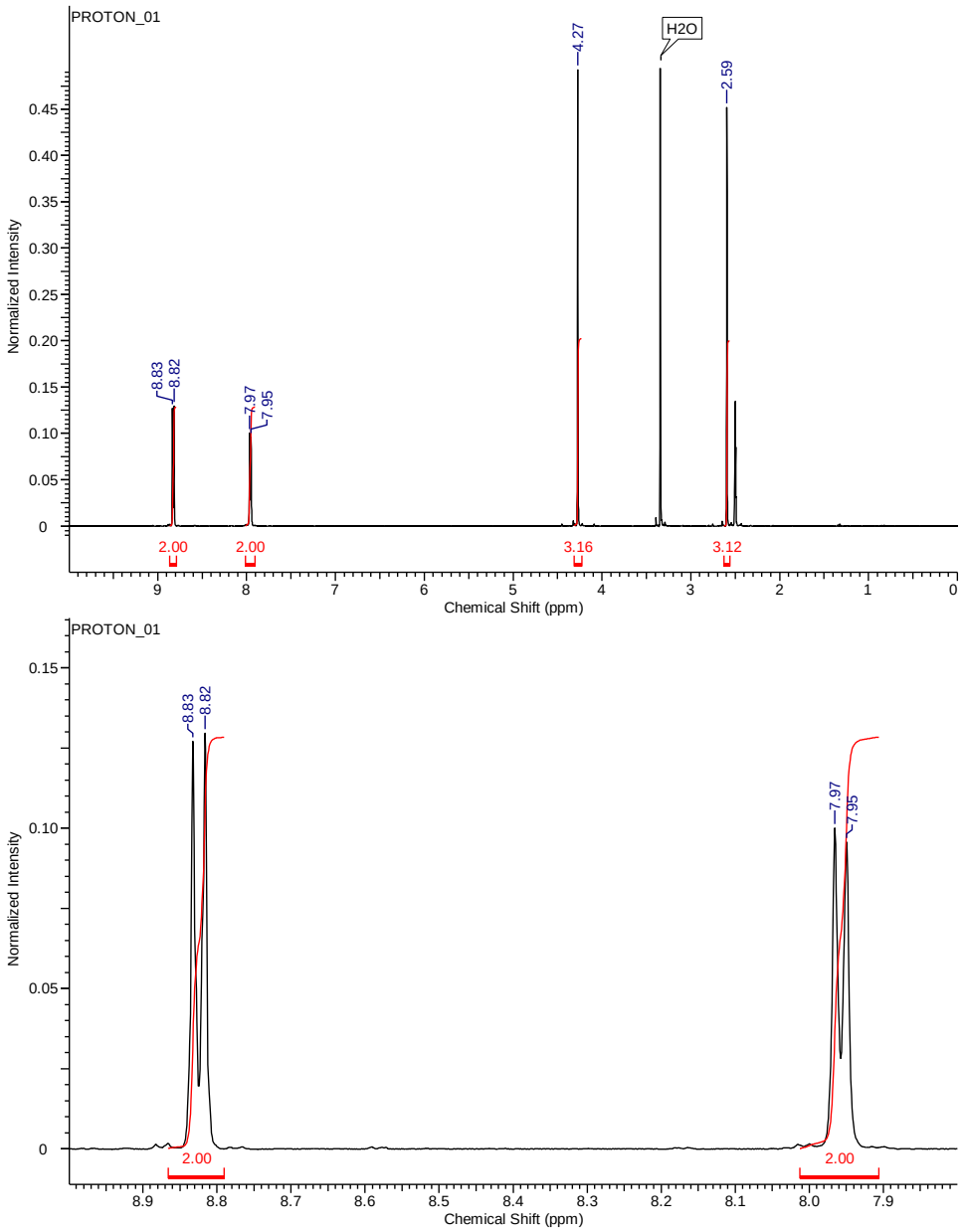

Figure A1. ^{1}H NMR spectrum of 1,4-dimethylpyridin-1-ium iodide (**I1**$^{+}$) recorded in and referenced versus d_6-dimethylsulfoxide (δ = 2.50 ppm).

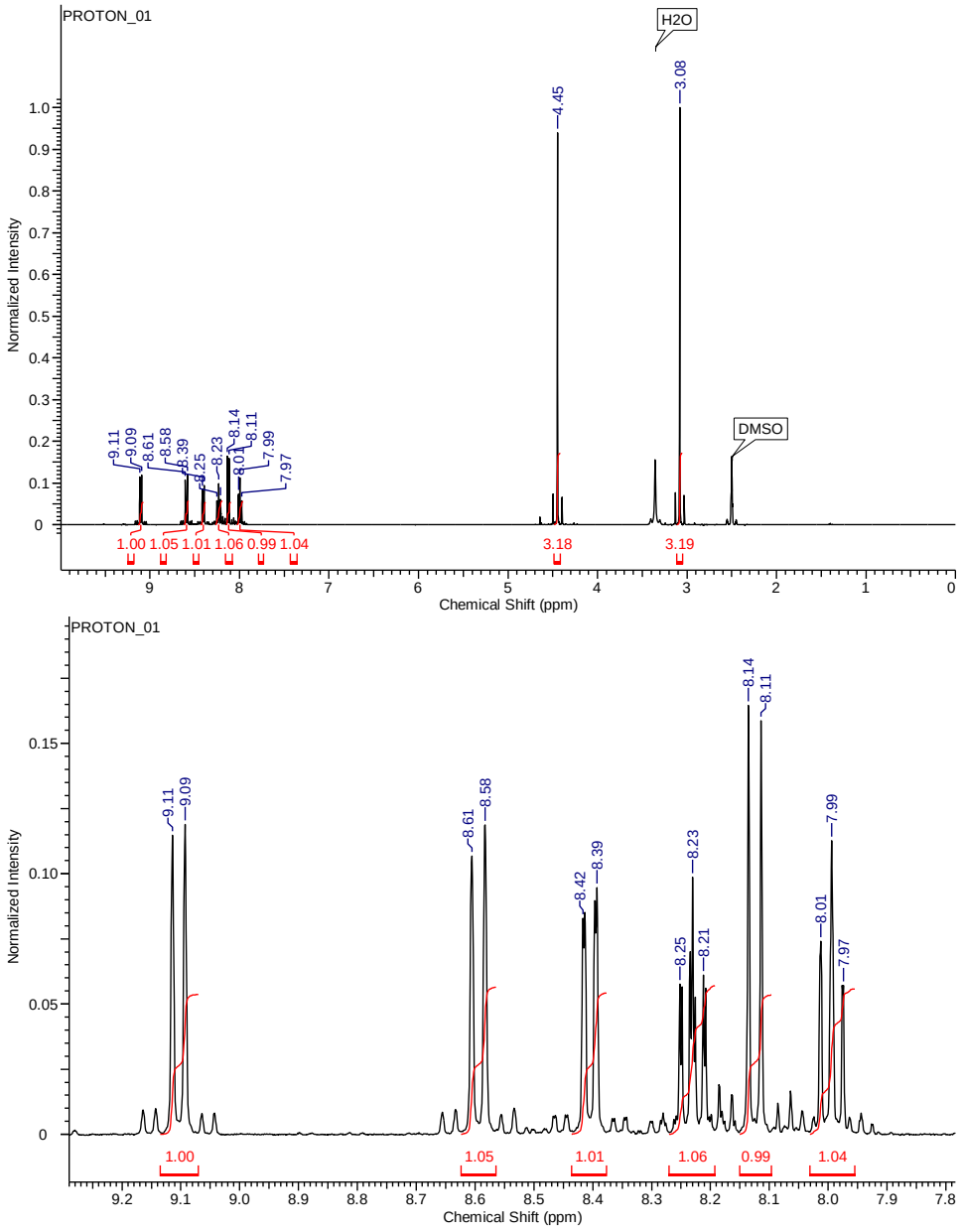

Figure A2. ^{1}H NMR spectrum of 1,2-dimethylquinolin-1-ium iodide (**I2**$^{+}$) recorded in and referenced versus d_6-dimethylsulfoxide (δ = 2.50 ppm).

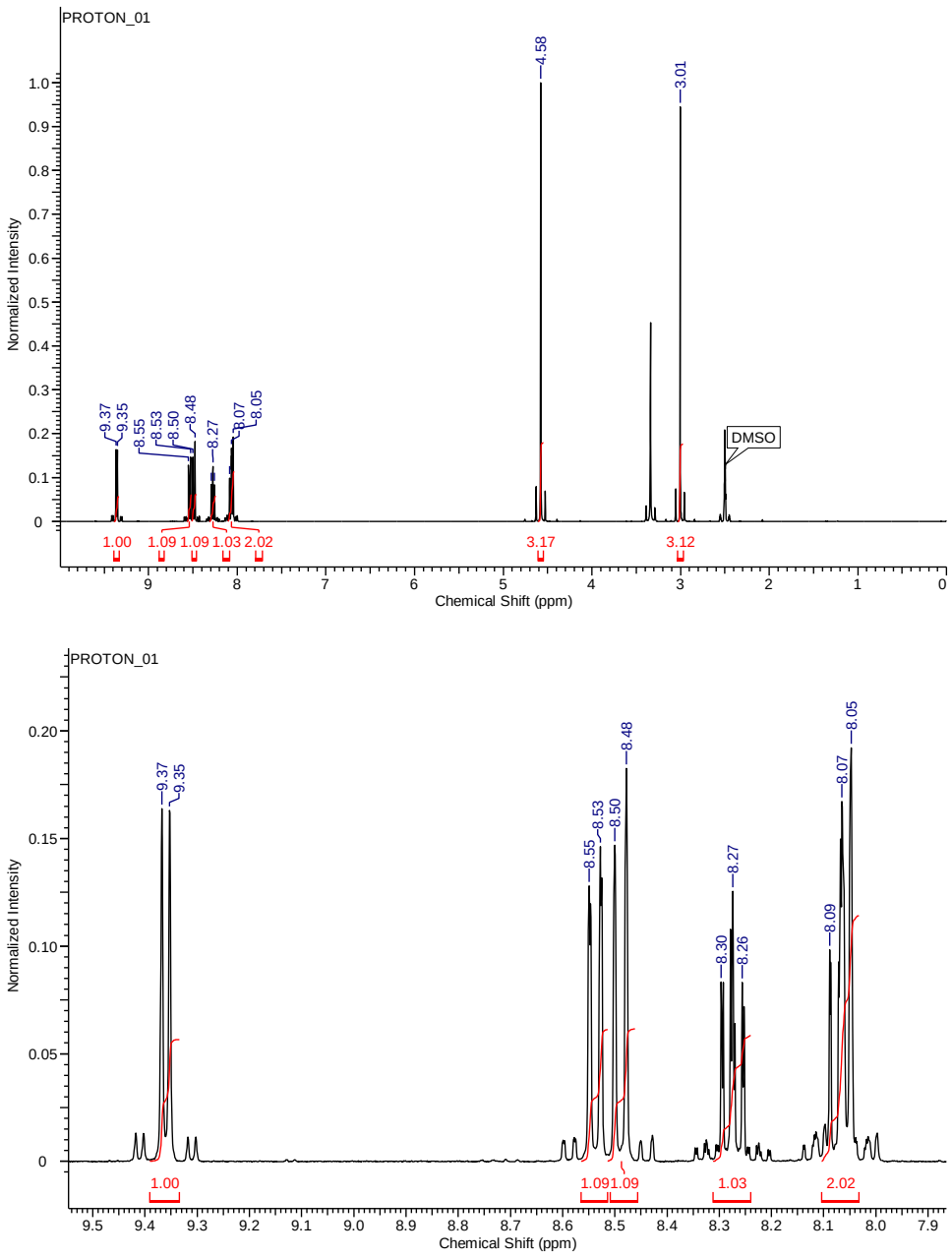

Figure A3. ^{1}H NMR spectrum of 1,4-dimethylquinolin-1-ium iodide (**I3**$^{+}$) recorded in and referenced versus d_6-dimethylsulfoxide (δ = 2.50 ppm).

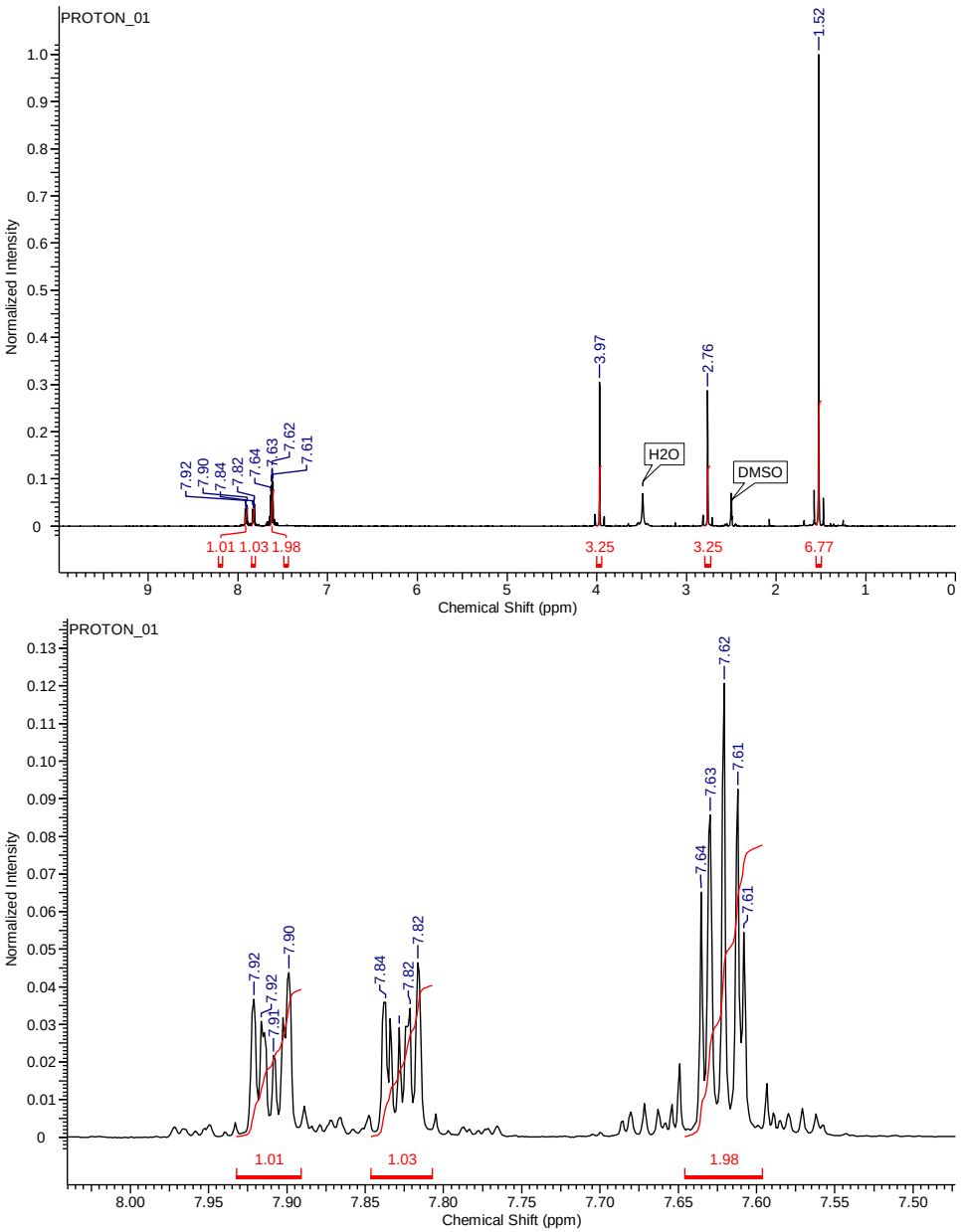

Figure A4. ^{1}H NMR spectrum of 1,2,3,3-tetramethyl-3H-indol-1-ium iodide (**I4**$^{+}$) recorded in and referenced versus d_6-dimethylsulfoxide (δ = 2.50 ppm).

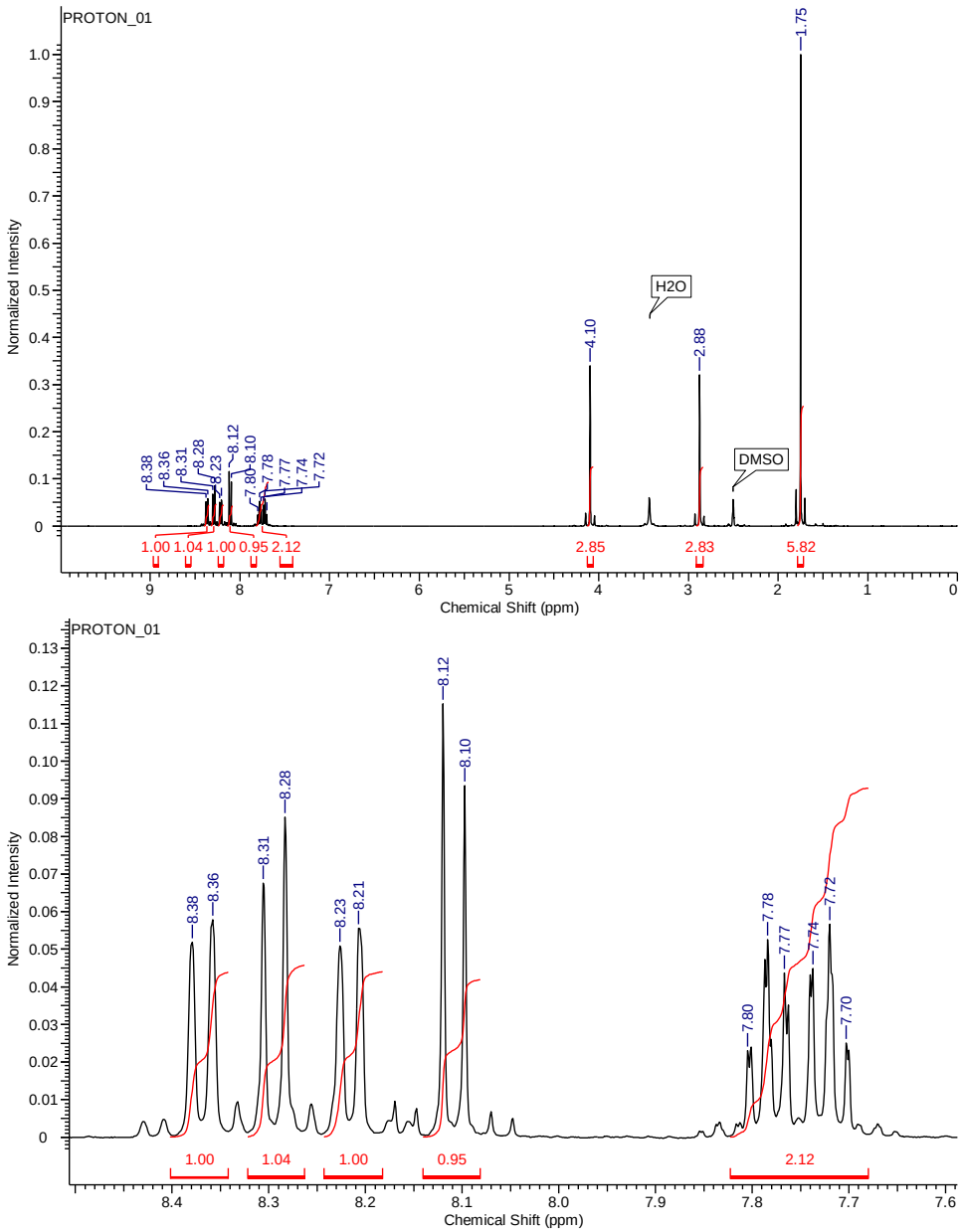

Figure A5. ^{1}H NMR spectrum of 1,1,2,3-tetramethyl-1H-benzo[e]indol-3-ium iodide (**I5**$^{+}$) recorded in and referenced versus d_6-dimethylsulfoxide (δ = 2.50 ppm).

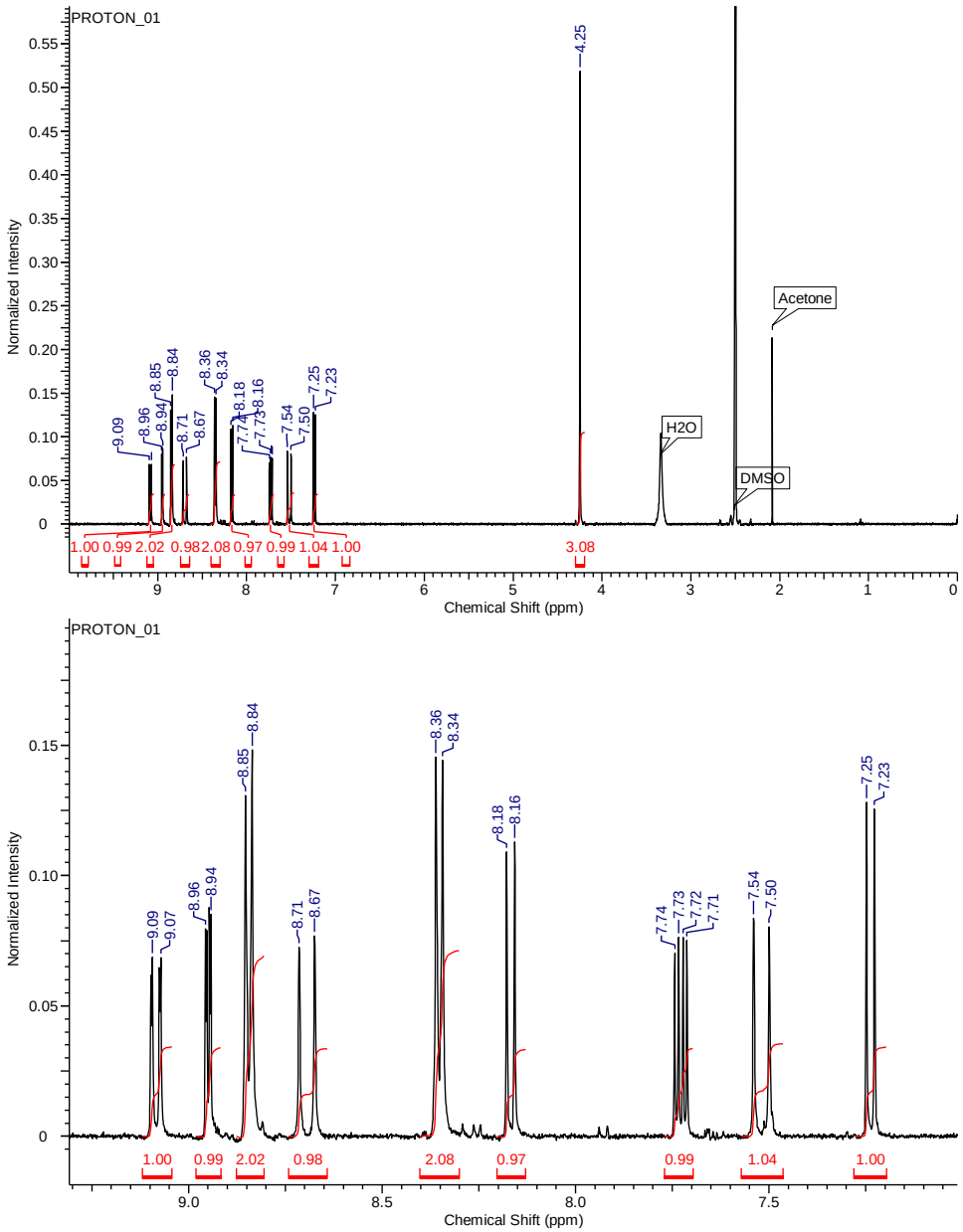

Figure A6. ^{1}H NMR spectrum of (E)-4-(2-(8-Hydroxyquinolin-5-yl)vinyl)-1-methylpyridin-1-ium hexafluorophosphate (**HL2**$^{+}$) recorded in and referenced versus d_6-dimethylsulfoxide (δ = 2.50 ppm).

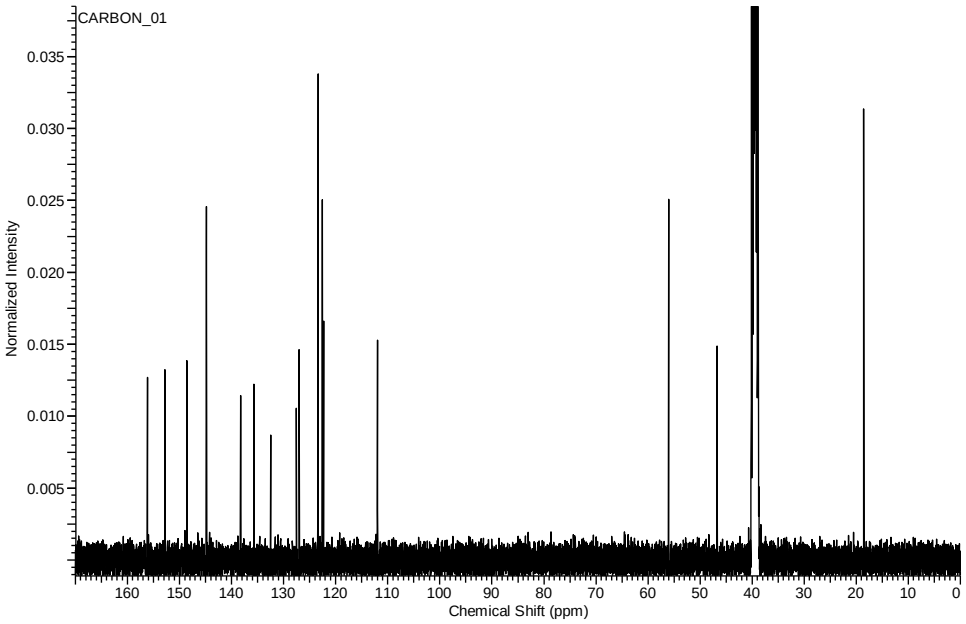

Figure A7. ^{13}C NMR spectrum of (E)-4-(2-(8-Hydroxyquinolin-5-yl)vinyl)-1-methylpyridin-1-ium hexafluorophosphate (**HL2**$^{+}$) recorded in and referenced versus d_6-dimethylsulfoxide (δ = 39.52 ppm).

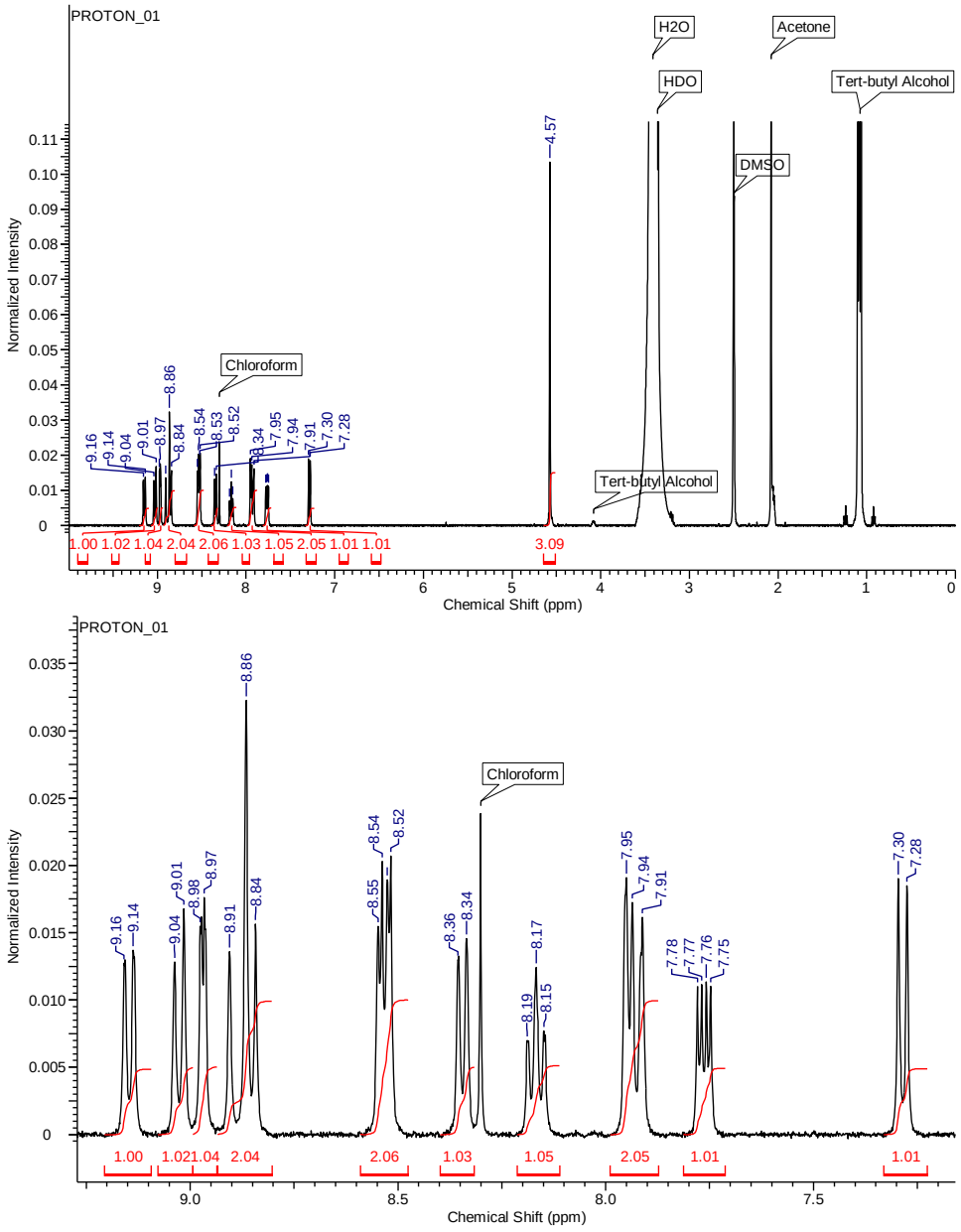

Figure A8. ^{1}H NMR spectrum of (E)-2-(2-(8-Hydroxyquinolin-5-yl)vinyl)-1-methylquinolin-1-ium hexafluorophosphate (**HL3**$^{+}$) recorded in and referenced versus d_6-dimethylsulfoxide (δ = 2.50 ppm).

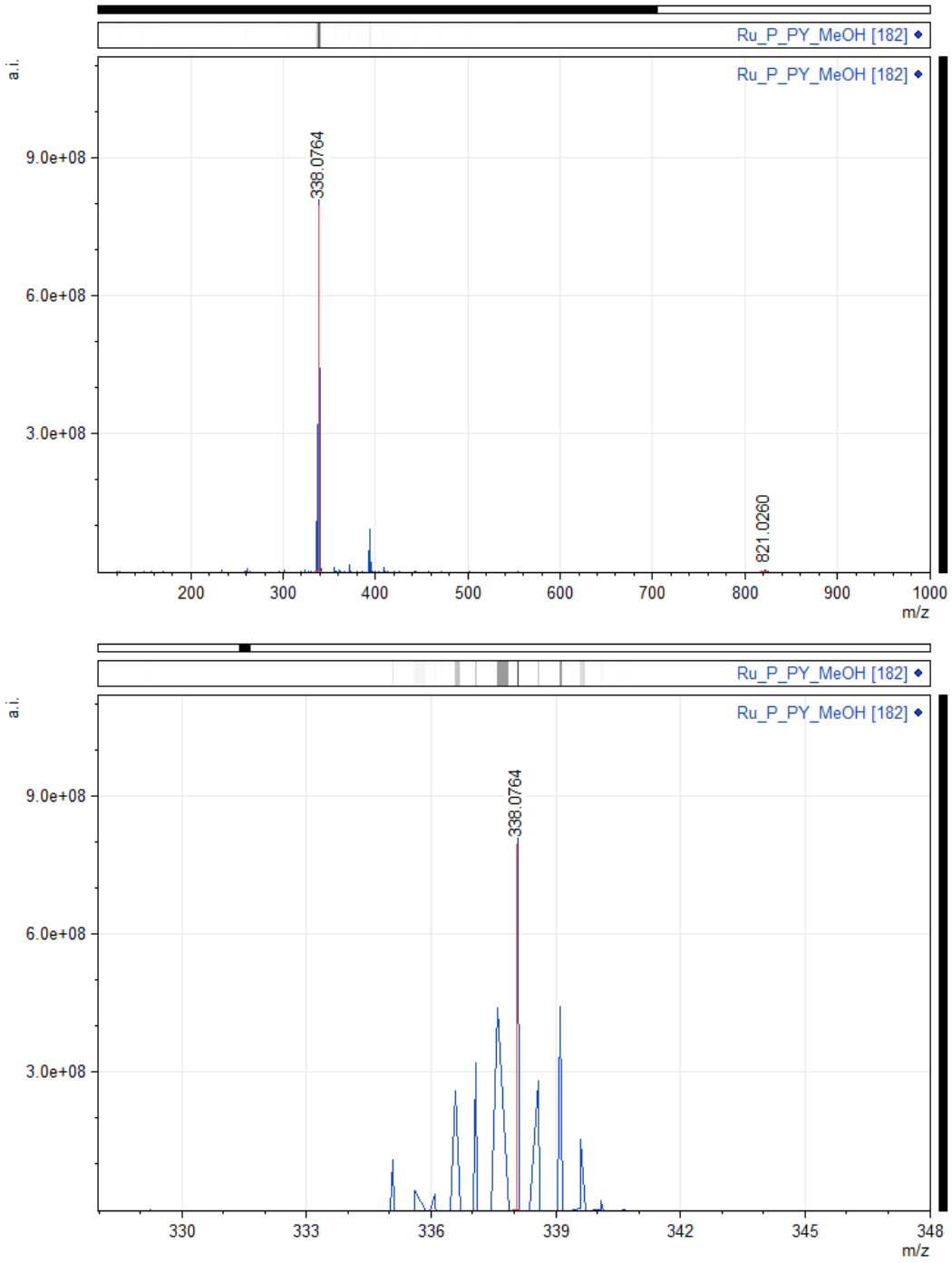

Figure A9. High resolution ESI-MS of **RuL2**$^{2+}$ recorded in neat methanol.

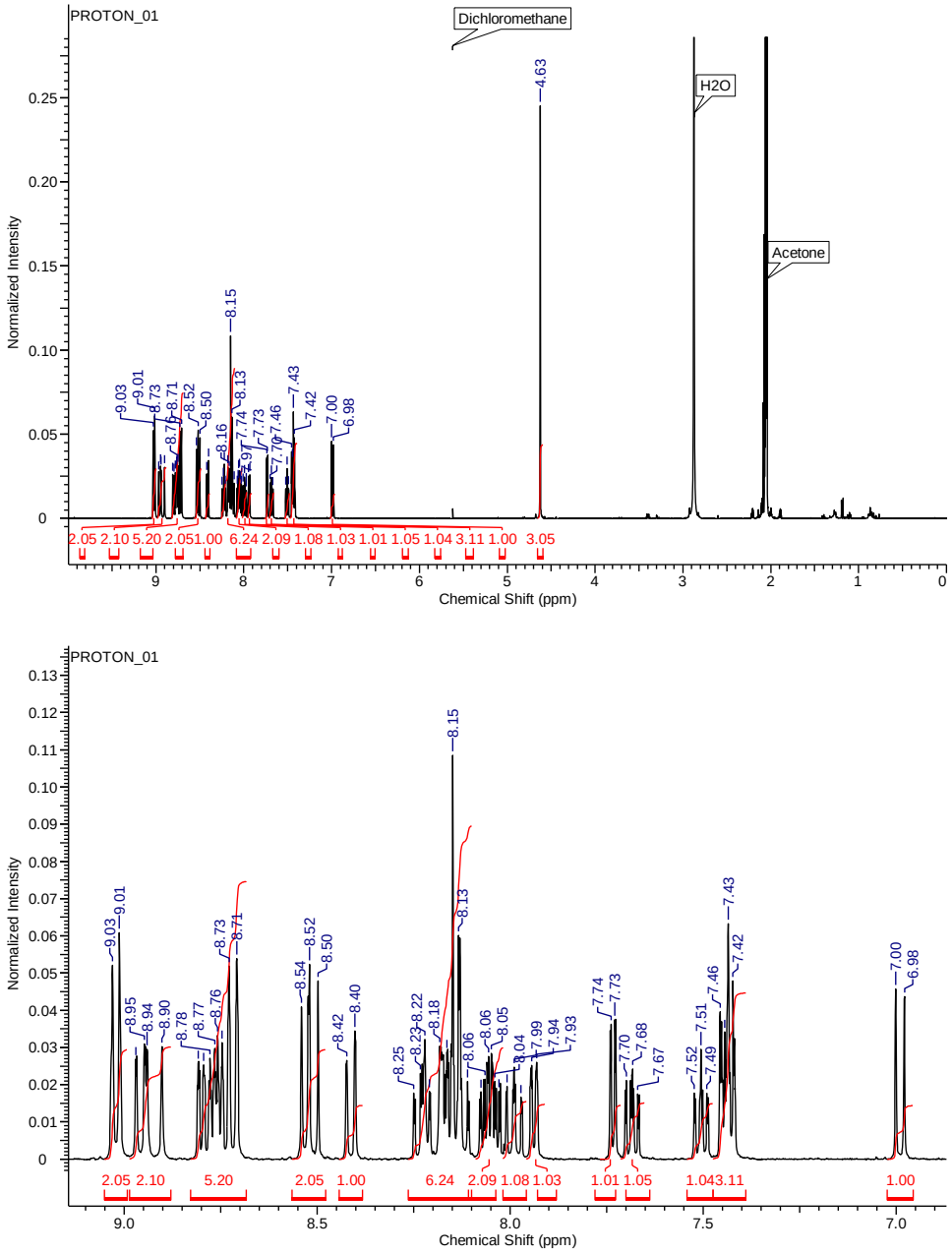

Figure A10. ^{1}H NMR spectrum of [Ru(bpy)$_2$(P-Qn-OQN)][2PF$_6$] (**RuL3^{2+}**) recorded in and referenced versus d_6-acetone (δ = 2.05 ppm).

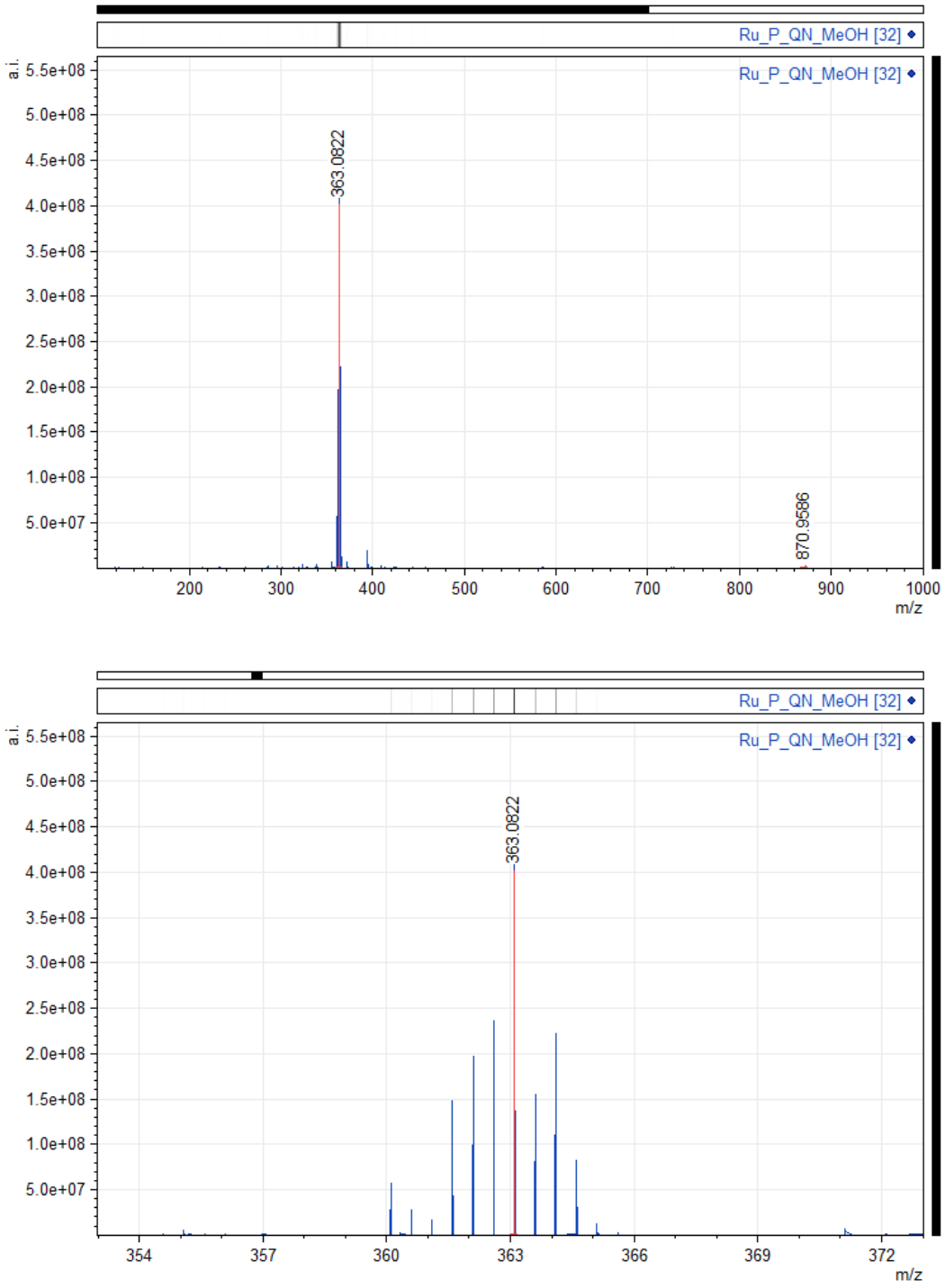

Figure A11. High resolution ESI-MS of **RuL3**$^{2+}$ recorded in neat methanol.

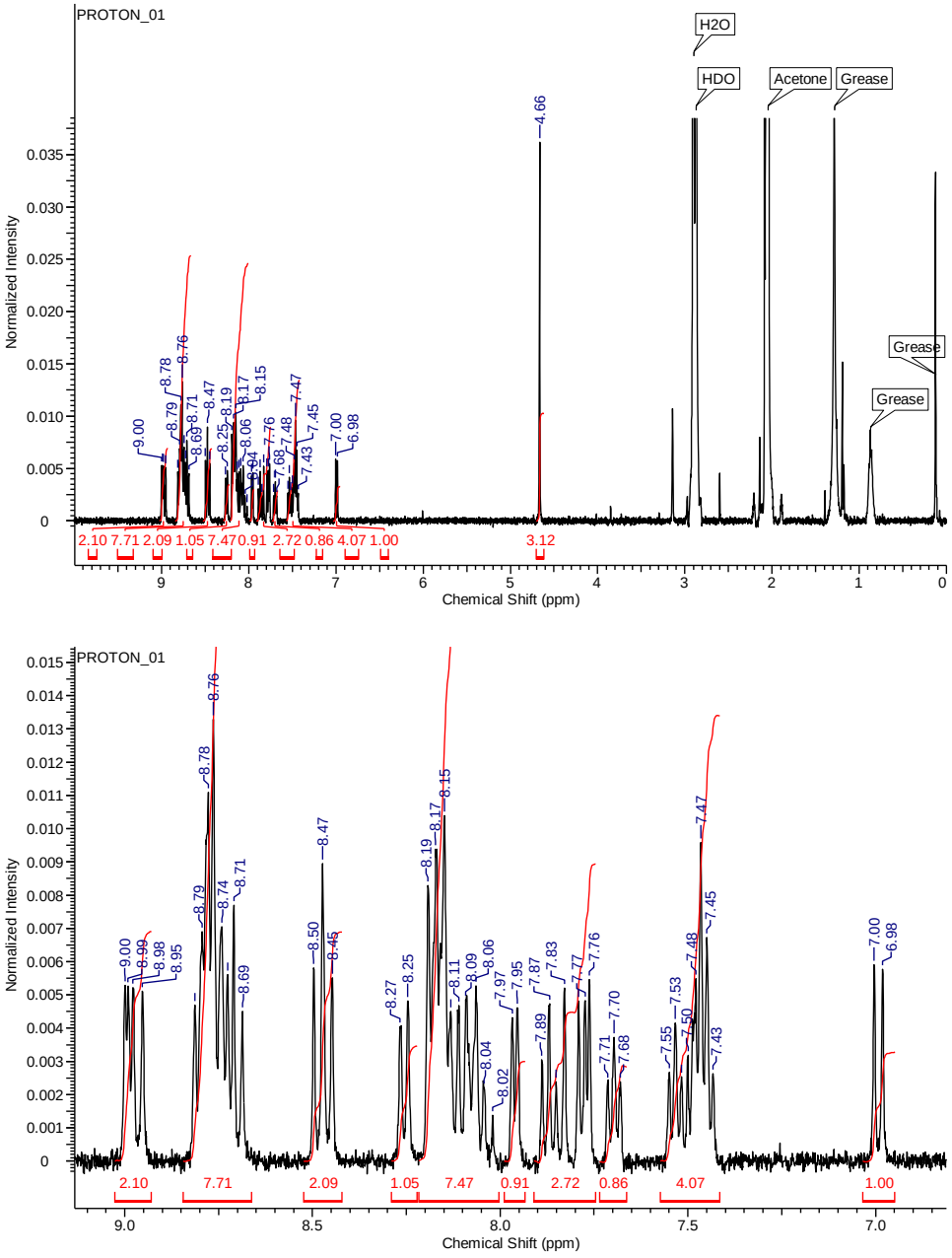

Figure A12. ^{1}H NMR spectrum of [Ru(bpy)$_2$(O-Qn-OQN)][2PF$_6$] (**RuL4^{2+}**) recorded in and referenced versus d_6-acetone (δ = 2.05 ppm).

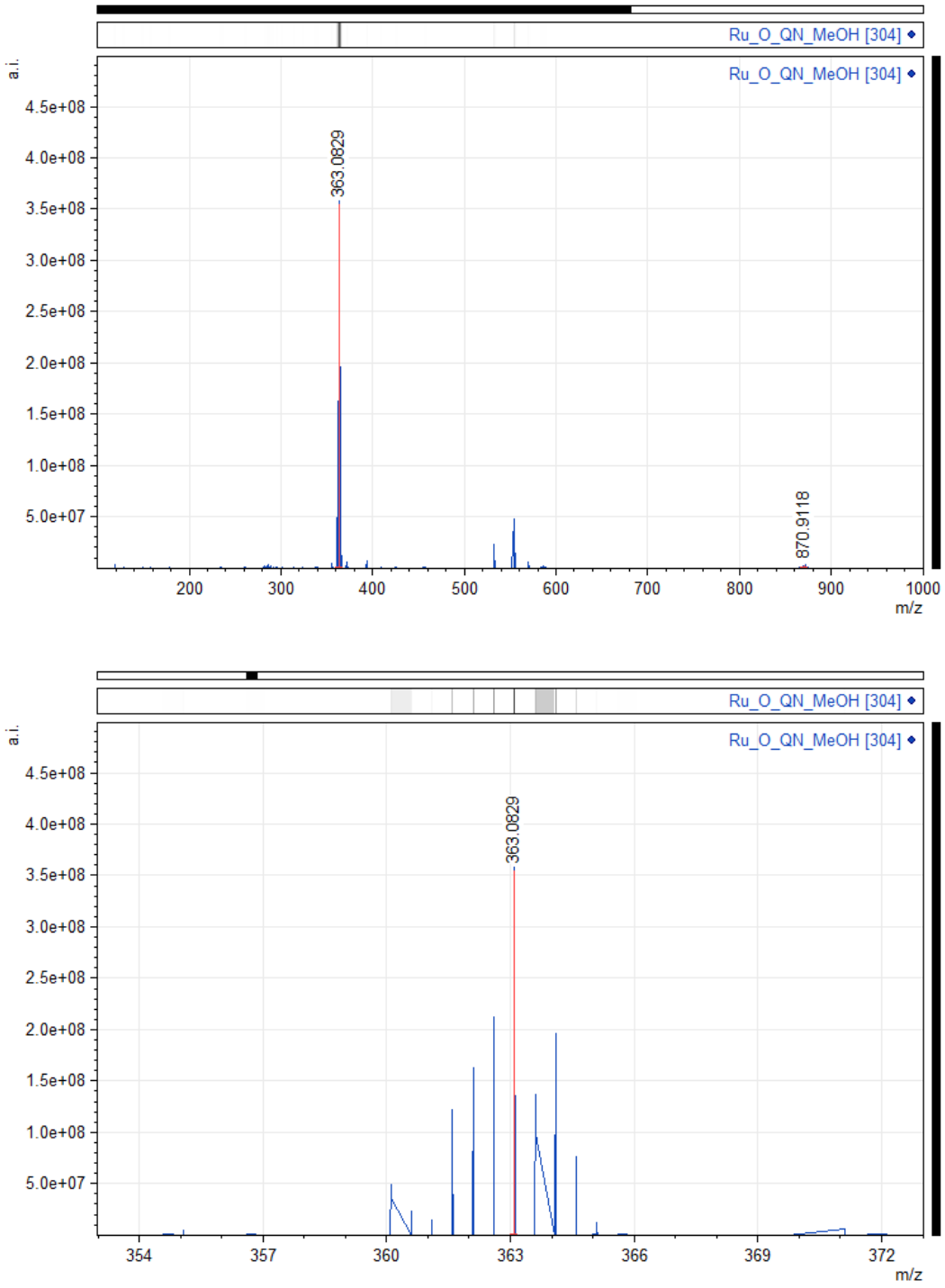

Figure A13. High resolution ESI-MS of **RuL4**$^{2+}$ recorded in neat methanol.

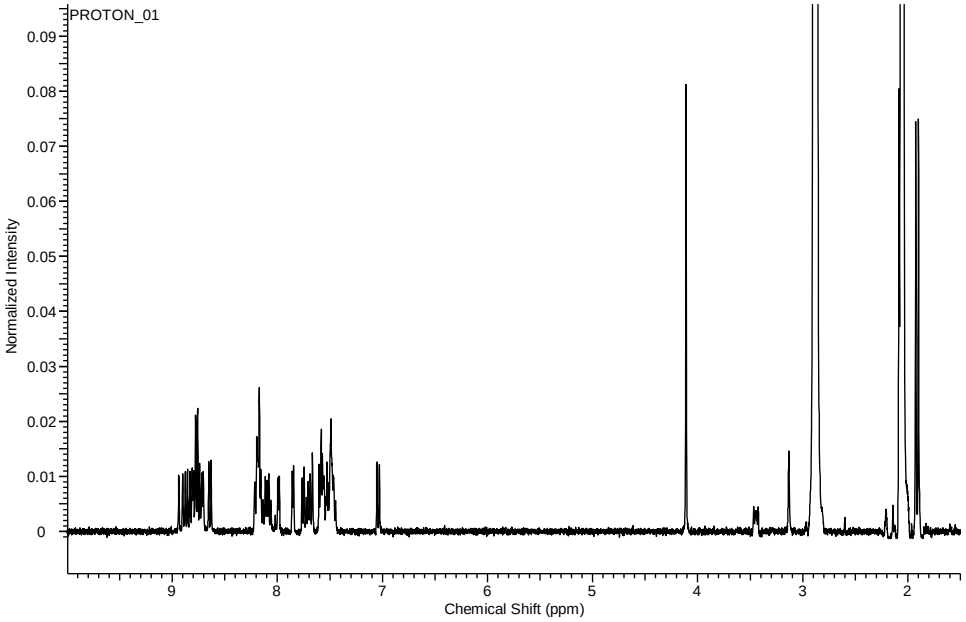

Figure A14. ^{1}H NMR spectrum of [Ru(bpy)$_2$(Ind-OQN)][2PF$_6$] (**RuL5^{2+}**) recorded in and referenced versus d_6-acetone (δ = 2.05 ppm).

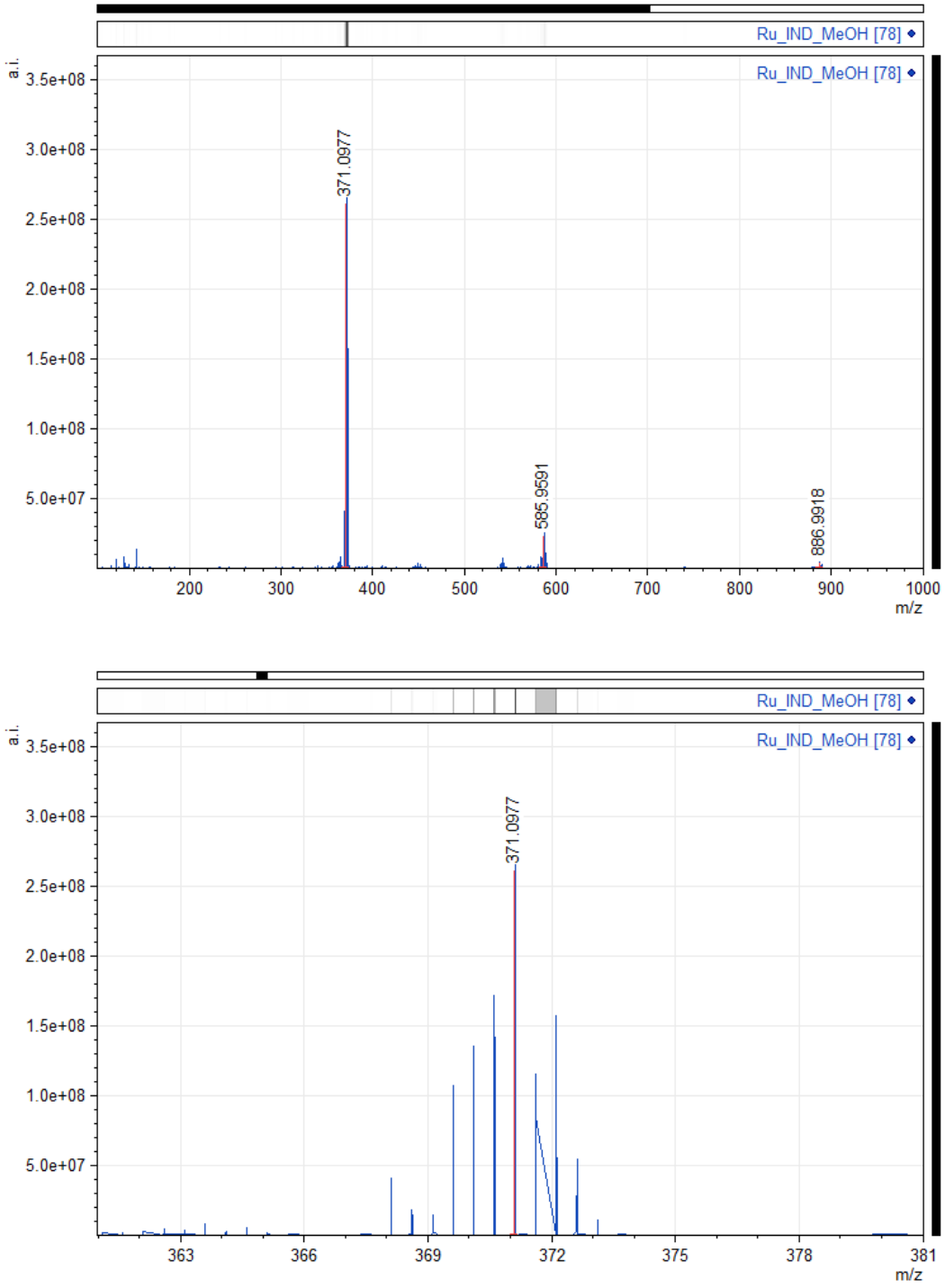

Figure A15. High resolution ESI-MS of **RuL5**$^{2+}$ recorded in neat methanol.

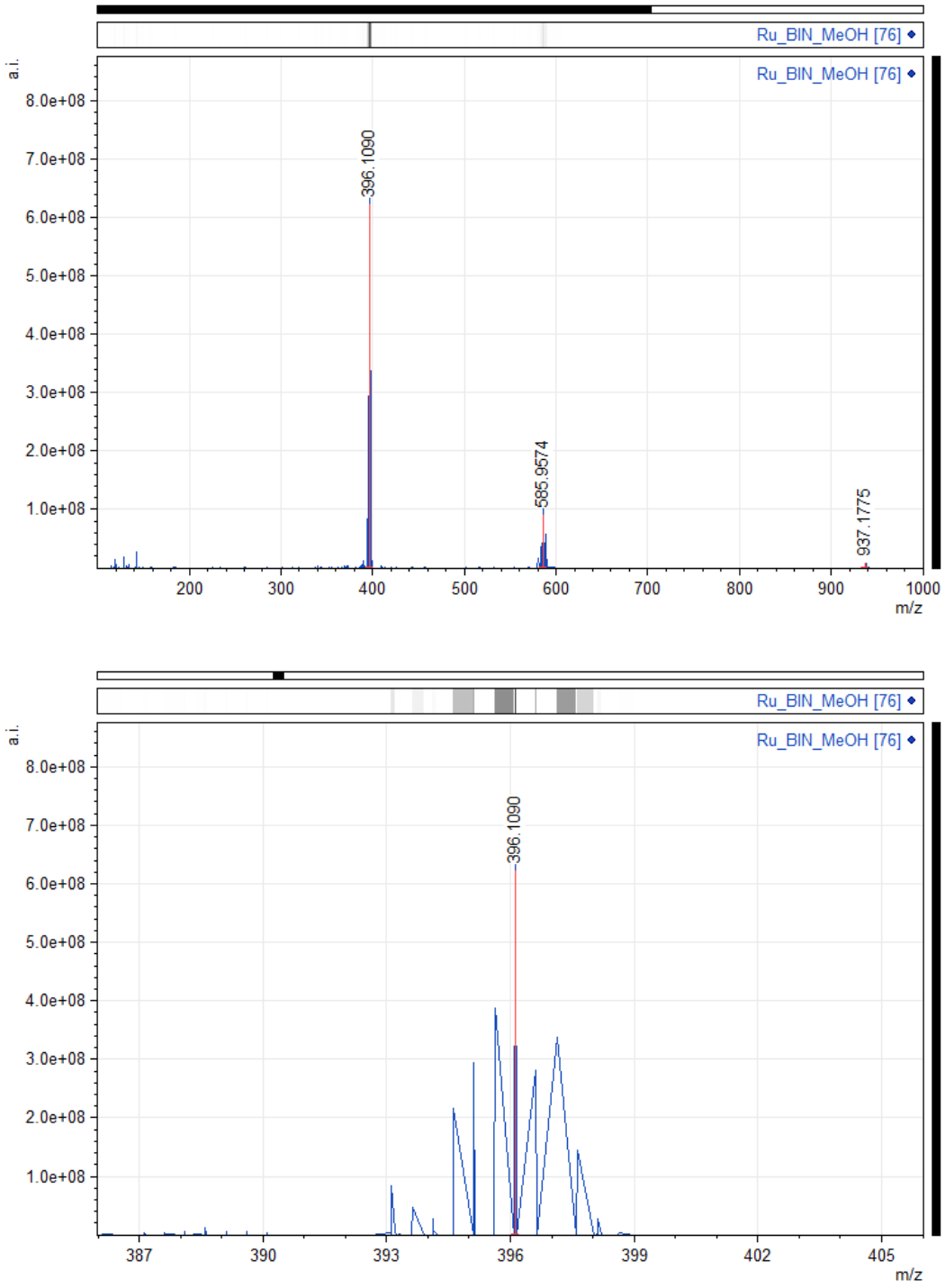

Figure A16. High resolution ESI-MS of **RuL6**$^{2+}$ recorded in neat methanol.

B. UV/VIS ELECTRONIC ABSORPTION DATA

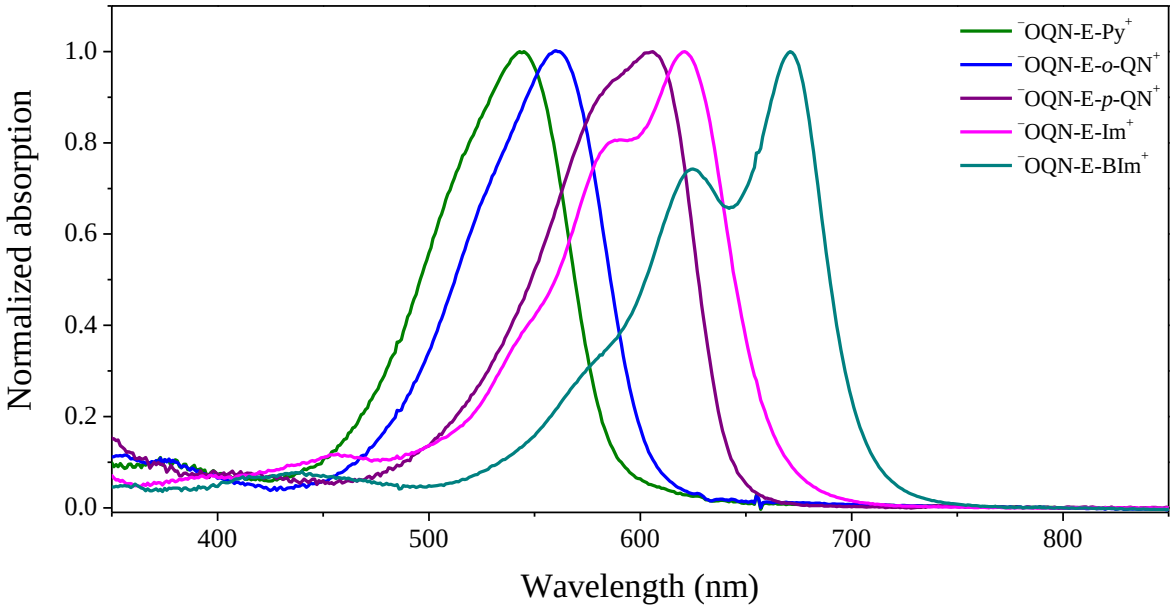

Figure A17. Normalized UV-vis of H**L2**$^{+}$-**HL6**$^{+}$ collected in acetonitrile with 10 equivalents of triethylamine added to isolate the deprotonated species.

C. MO DIAGRAM

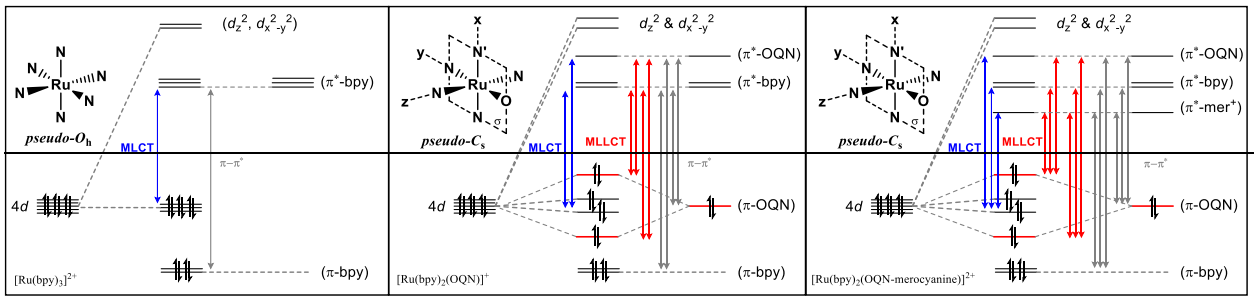

Figure A18. Molecular orbital correlation diagrams of [Ru(bpy)$_3$]$^{2+}$ (left), **RuL1**$^{+}$ (center) and **RuL2**$^{2+}$-**RuL6**$^{2+}$ (right).

D. COMPUTATIONAL ANALYSIS

$[Ru(bpy)_3]^{2+}$

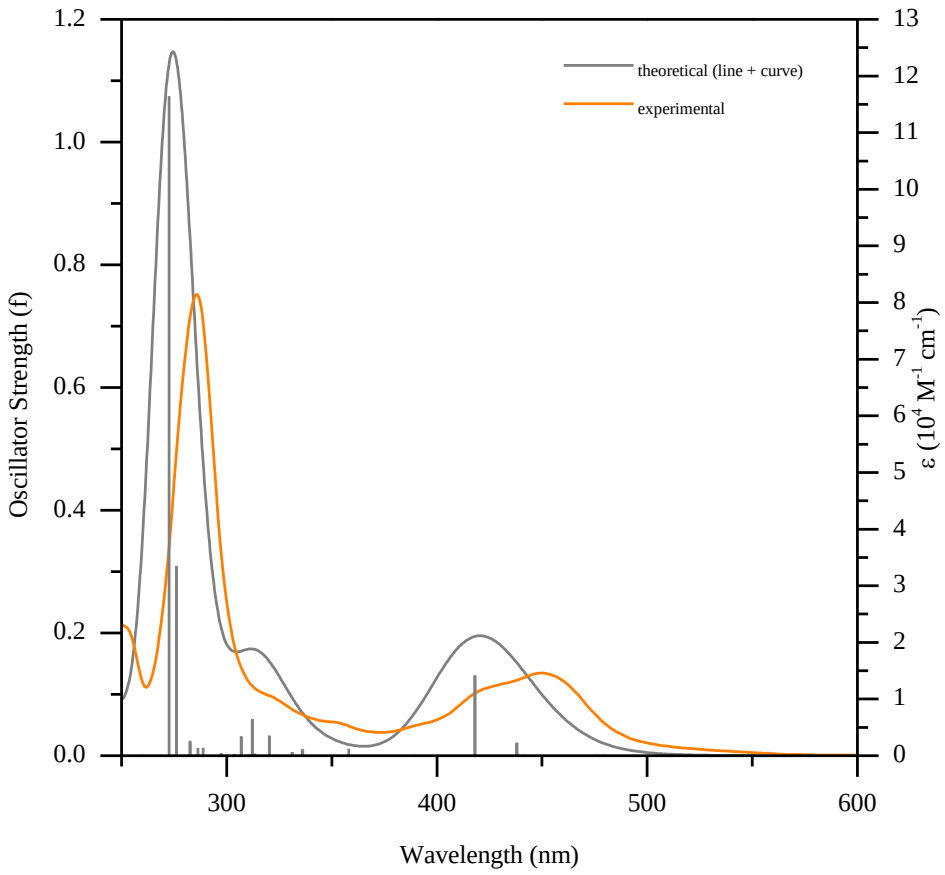

Figure A19. An overlay of experimental and theoretical spectra of $[Ru(bpy)_3]^{2+}$

.

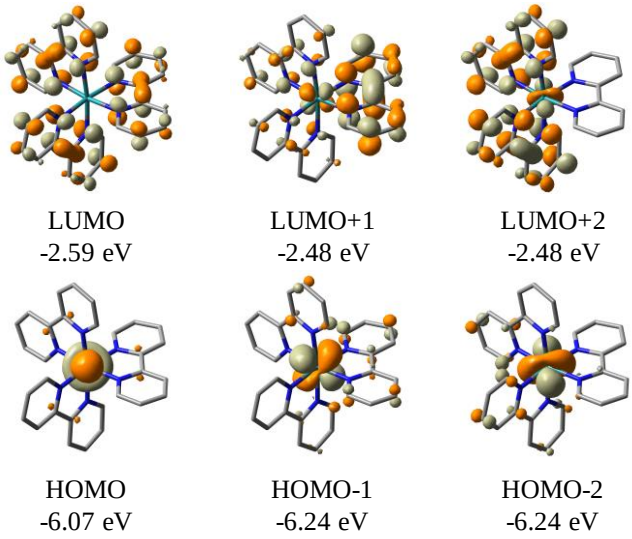

Figure A20. Selected molecular orbital surfaces (isofactor = 0.04) and energies for $[Ru(bpy)_3]^{2+}$

Electronic Transition (nm)	MO Contributions (%)	Oscillator Strength (f)
231.5065571	H-4->L+5 (23%), H-3->L+4 (22%), H-2->L+9 (22%)	0.0357
231.5238495	H-4->L+4 (21%), H-3->L+5 (22%), H-1->L+9 (23%)	0.0386
232.5181663	H-3->L+6 (17%), HOMO->L+11 (13%)	0.0181
232.5486948	H-4->L+6 (19%), HOMO->L+10 (11%)	0.0162
232.6228689	H-4->L+4 (12%), H-3->L+4 (20%)	0.0321
243.2954016	H-5->L+3 (87%)	0.0544
245.443514	H-4->L+3 (75%), H-3->L+3 (12%)	0.0283
245.4580916	H-4->L+3 (12%), H-3->L+3 (75%)	0.0281
272.5807115	H-5->LUMO (19%), H-4->L+1 (16%), H-4->L+2 (12%), H-3->L+1 (12%), H-3->L+2 (17%)	1.0752
276.0522268	H-5->L+2 (50%)	0.3095
276.1260031	H-5->L+1 (51%)	0.3077
282.5122742	H-5->L+2 (39%), H-4->L+2 (22%), H-3->L+1 (22%)	0.0245
282.6410811	H-5->L+1 (38%), H-4->L+1 (23%), H-3->L+2 (22%)	0.0227
286.3621042	H-5->LUMO (70%)	0.0125
288.7698536	H-4->LUMO (80%)	0.0131
288.8169415	H-3->LUMO (80%)	0.0129
306.9122376	H-2->L+4 (11%), H-1->L+5 (10%), HOMO->L+13 (23%)	0.0322

307.026241	H-2->L+5 (12%), H-1->L+4 (10%), HOMO->L+12 (24%)	0.0305
312.0726337	H-2->L+6 (65%)	0.0583
312.3320653	H-1->L+6 (63%)	0.0598
320.2958915	HOMO->L+7 (63%), HOMO->L+8 (25%)	0.033
320.3372691	HOMO->L+7 (25%), HOMO->L+8 (62%)	0.0319
335.9526802	H-2->L+3 (98%)	0.0107
336.1986459	H-1->L+3 (98%)	0.0107
358.0953027	HOMO->L+3 (98%)	0.0117
418.0012024	H-2->LUMO (13%), H-2->L+1 (17%), H-2->L+2 (26%), H-1->L+1 (24%), H-1->L+2 (17%)	0.1312
418.1280745	H-2->L+1 (25%), H-2->L+2 (17%), H-1->LUMO (13%), H-1->L+1 (17%), H-1->L+2 (25%)	0.1303
437.8406492	H-2->LUMO (84%)	0.0207
438.1655946	H-1->LUMO (84%)	0.0214
479.3479081	HOMO->LUMO (99%)	0.0019

Table A1. Select electronic transitions for $[Ru(bpy)_3]^{2+}$ calculated by TDDFT (>10% contribution threshold excluding the HOMO→LUMO transition at 479 nm).

RuL1^{+} $[Ru(bpy)_2(OQN)]^{+}$

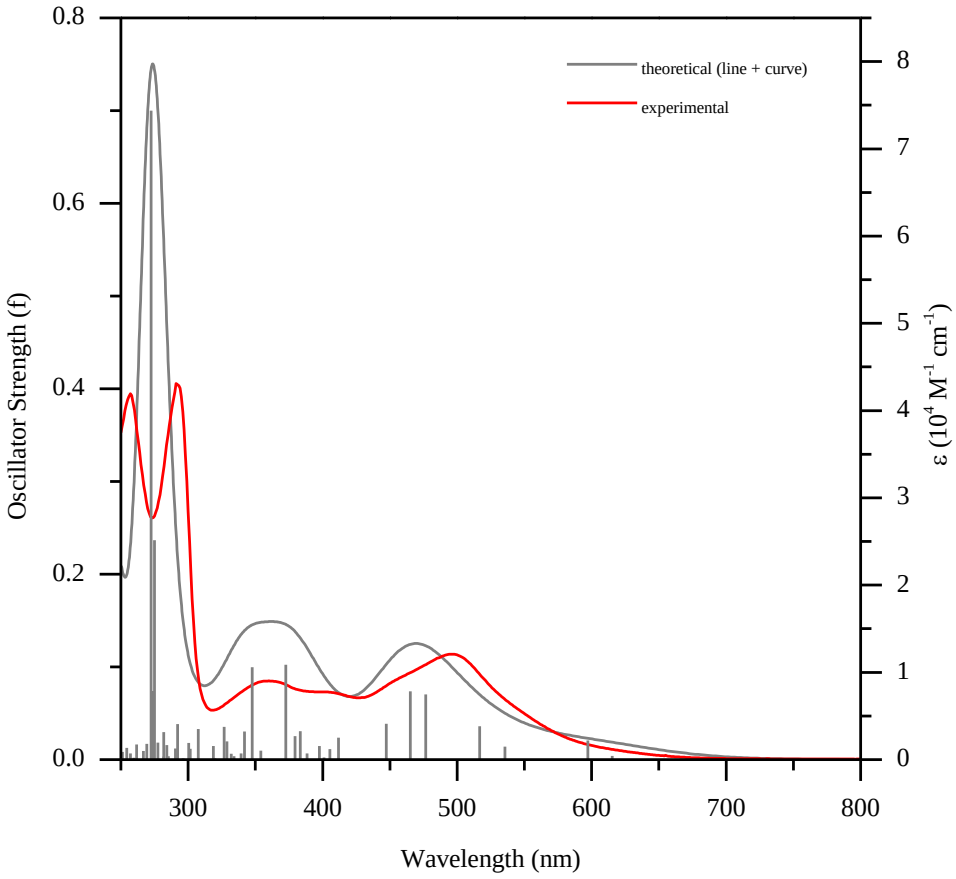

Figure A21. An overlay of experimental and theoretical spectra of **RuL1**$^{+}$.

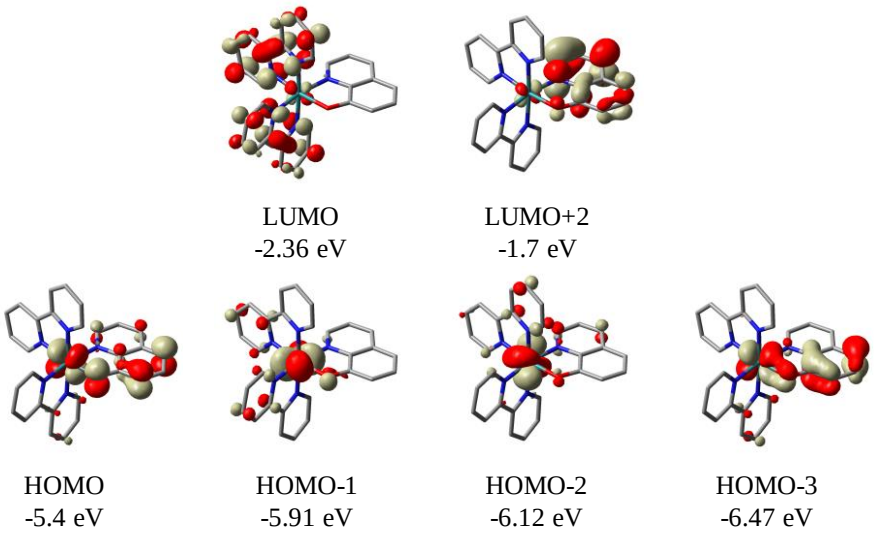

Figure A22. Selected molecular orbital surfaces (isofactor = 0.04) and energies for **RuL1**$^{+}$.

Electronic Transition (nm)	MO Contributions (%)	Oscillator Strength (f)
239.3269697	H-8->LUMO (47%), H-2->L+9 (25%)	0.0261
239.5489241	H-8->LUMO (16%), H-5->L+3 (51%)	0.0493
240.5575022	H-4->L+3 (64%)	0.0636
241.4569928	H-8->LUMO (12%), H-7->L+2 (14%), H-6->L+3 (18%), H-2->L+9 (33%)	0.0187
244.7168337	H-4->L+2 (36%), H-4->L+3 (15%), HOMO->L+13 (16%)	0.1664
246.8558221	H-6->L+2 (47%), H-5->L+2 (43%)	0.0276
254.3143597	H-7->L+1 (10%), H-1->L+8 (72%)	0.0126
261.7338751	H-4->L+2 (17%), H-3->L+7 (65%)	0.0162
269.3006726	HOMO->L+9 (89%)	0.017
272.4668966	H-6->LUMO (22%), H-5->L+1 (39%)	0.6999
273.6516137	H-2->L+11 (32%), H-1->L+12 (30%)	0.0739
274.8771459	H-6->L+1 (65%)	0.2368
277.3924661	HOMO->L+8 (83%)	0.0183
281.940504	H-6->LUMO (55%), H-6->L+1 (16%), H-5->L+1 (16%)	0.0298
284.1959763	H-5->LUMO (67%), H-5->L+1 (17%)	0.0157
290.4679426	H-4->LUMO (45%), H-3->L+6 (17%)	0.0119
292.2756639	H-4->LUMO (19%), H-3->L+5 (55%)	0.0383
300.4564077	H-3->L+4 (48%), H-2->L+12 (12%)	0.0181
301.6112502	H-3->L+4 (33%), H-2->L+12 (15%)	0.0117

307.4144867	H-3->L+3 (50%)	0.033
318.7560074	H-3->L+3 (40%), H-2->L+4 (11%), H-2->L+6 (12%)	0.0147
326.8309915	HOMO->L+7 (71%)	0.0354
328.8944389	H-2->L+5 (82%)	0.0197
341.9192428	H-3->L+2 (16%), H-2->L+4 (18%), H-1->L+6 (41%)	0.0302
347.5356318	H-2->L+3 (12%), H-1->L+5 (62%), H-1->L+6 (19%)	0.0996
372.6356595	H-2->L+2 (75%)	0.1025
379.5834328	H-1->L+3 (90%)	0.0252
383.32716	H-3->L+1 (10%), HOMO->L+6 (69%)	0.0307
397.4716656	H-3->LUMO (16%), H-3->L+1 (23%), HOMO->L+4 (29%), HOMO->L+5 (12%)	0.0148
405.2935067	H-3->LUMO (62%), H-3->L+1 (12%), HOMO->L+4 (15%)	0.0112
411.7679729	H-1->L+2 (76%)	0.0238
447.415599	H-2->LUMO (13%), H-2->L+1 (53%)	0.0387
465.1759151	HOMO->L+2 (84%)	0.0736
476.6573244	H-2->LUMO (77%), H-2->L+1 (13%)	0.0705
516.7694925	H-2->L+1 (12%), H-1->LUMO (10%), H-1->L+1 (67%)	0.036
535.4726468	H-1->LUMO (81%), H-1->L+1 (12%)	0.0139
597.2797796	HOMO->LUMO (20%), HOMO->L+1 (68%)	0.0206
615.332456398	HOMO->LUMO (72%), HOMO->L+1 (22%)	0.0041

Table A2. Select electronic transitions for **RuL1**$^{+}$ calculated by TDDFT (>10% contribution threshold except for the two lowest energy transitions).

RuL2^{2+} $[Ru(bpy)_2(P\text{-}Py\text{-}OQN)]^{2+}$

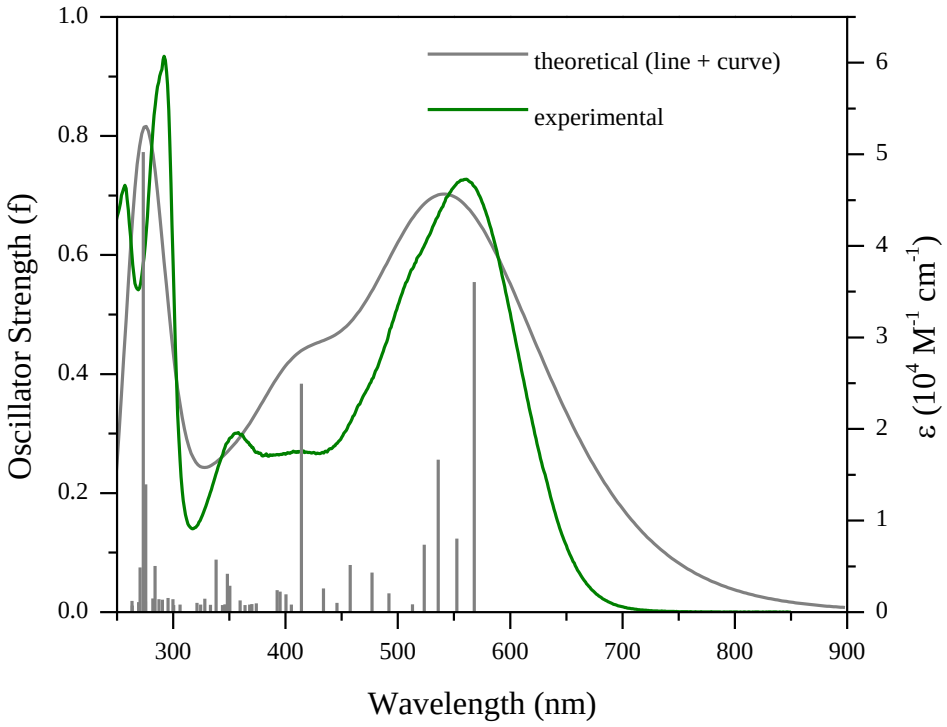

Figure A23. An overlay of experimental and theoretical spectra of **RuL2**$^{2+}$.

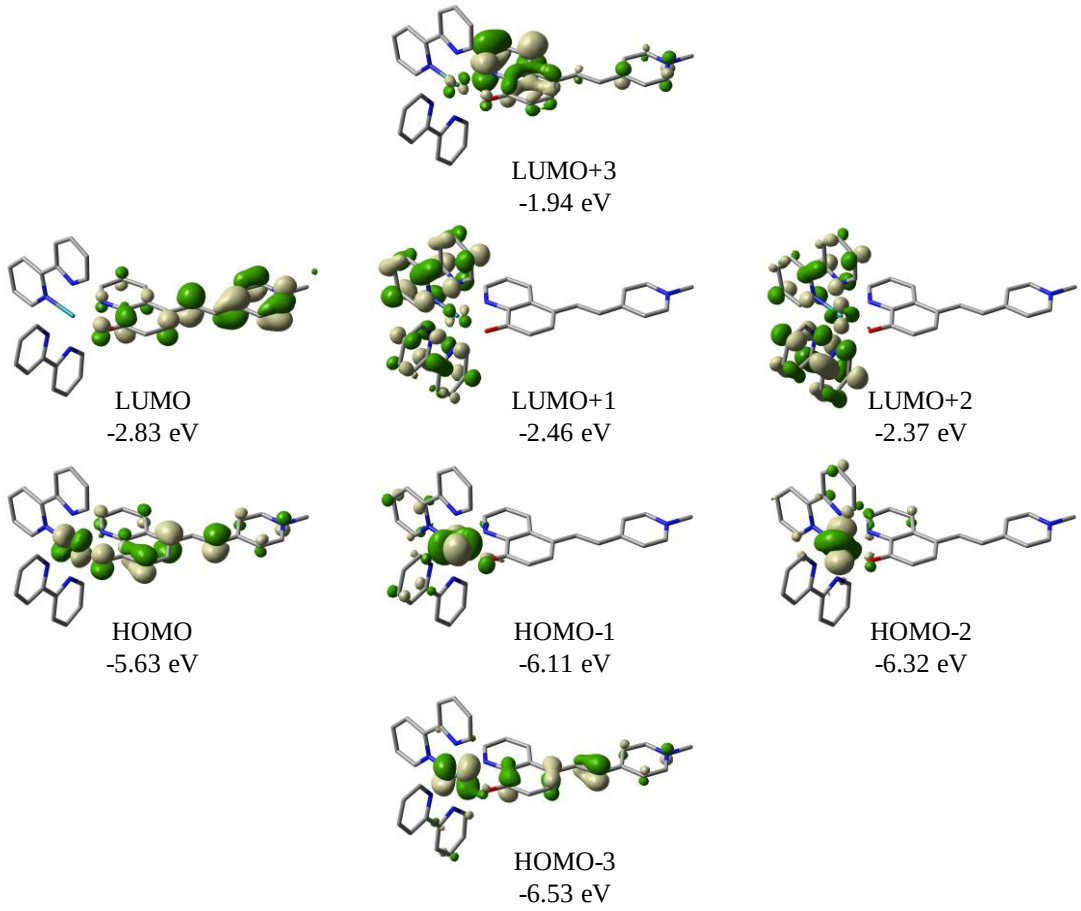

Figure A24. Selected molecular orbital surfaces (isofactor = 0.04) and energies for **RuL2**$^{2+}$.

Electronic Transition (nm)	MO Contributions (%)	Oscillator Strength
263.2286717	H-3->L+9 (21%), HOMO->L+10 (10%), HOMO->L+11 (34%)	0.0189
263.5308025	H-3->L+9 (13%), HOMO->L+11 (50%)	0.0111
269.2831255	H-6->L+1 (61%)	0.0169
270.457957	H-7->LUMO (19%), H-6->L+1 (24%), H-3->L+9 (34%)	0.0752
273.2475352	H-5->L+1 (30%), H-4->L+2 (42%)	0.7729
275.371661	H-2->L+13 (38%), H-1->L+15 (18%)	0.0182
275.5981431	H-5->L+2 (61%), H-4->L+1 (10%), H-4->L+2 (10%)	0.2145
281.8956315	H-5->L+1 (49%), H-5->L+2 (22%), H-4->L+2 (16%)	0.0229
283.7666773	H-7->LUMO (32%), H-2->L+9 (18%), HOMO->L+10 (37%)	0.0776

287.2577944	H-2->L+9 (62%), HOMO->L+10 (17%)	0.0218
290.2707294	H-3->L+6 (48%), H-3->L+7 (11%)	0.0208
295.4939145	H-6->LUMO (50%), H-1->L+8 (20%)	0.024
299.8387827	H-3->L+5 (62%)	0.0217
300.3399546	H-4->LUMO (47%), H-1->L+9 (11%)	0.0118
306.0032496	H-3->L+4 (22%), H-1->L+9 (31%)	0.0129
321.1254802	H-2->L+6 (88%)	0.0158
324.4023565	H-2->L+5 (21%), H-2->L+7 (59%)	0.0129
328.2066302	H-1->L+13 (11%), HOMO->L+9 (63%)	0.0225
333.1183982	H-2->L+5 (18%), H-1->L+7 (42%)	0.0125
338.2809109	H-2->L+4 (11%), H-1->L+6 (64%), H-1->L+7 (15%)	0.0881
343.8155809	H-2->L+4 (74%), H-1->L+6 (17%)	0.012
345.9646082	HOMO->L+8 (95%)	0.0132
348.1406695	H-3->L+3 (53%), H-1->L+5 (29%)	0.0645
350.4730231	H-3->L+3 (32%), H-1->L+5 (62%)	0.0443
359.5908717	HOMO->L+6 (11%), HOMO->L+7 (75%)	0.0197
363.9503806	HOMO->L+6 (66%), HOMO->L+7 (12%)	0.0118
368.0341268	H-1->L+4 (84%)	0.0129
370.0774182	H-2->L+3 (70%)	0.0135
373.9619251	HOMO->L+5 (83%)	0.0147
392.5386628	H-3->L+2 (28%), HOMO->L+4 (42%)	0.0368
395.2415972	H-3->L+1 (29%), H-3->L+2 (16%), HOMO->L+4 (43%)	0.0343
400.4629736	H-3->L+1 (29%), H-3->L+2 (42%), H-1->L+3 (10%)	0.0298
405.1875442	H-3->L+1 (18%), H-1->L+3 (66%)	0.0126
414.244359	H-3->LUMO (84%)	0.3839
433.690138	H-2->L+1 (16%), H-2->L+2 (51%)	0.0397
445.7587425	HOMO->L+3 (84%)	0.0155
457.621292	H-2->L+1 (71%), H-2->L+2 (12%)	0.0791
476.9507084	H-2->LUMO (89%)	0.0663
492.1340715	H-2->L+2 (14%), H-1->L+1 (10%), H-1->L+2 (49%), HOMO->L+2 (13%)	0.0316
513.112348	H-1->L+1 (72%), H-1->L+2 (17%)	0.0131
523.4235515	H-1->LUMO (87%)	0.1132
535.9124125	H-1->L+2 (14%), HOMO->LUMO (20%), HOMO->L+1 (27%), HOMO->L+2 (24%)	0.2562
552.5104128	HOMO->LUMO (11%), HOMO->L+1 (19%), HOMO->L+2 (55%)	0.1235
568.001359	HOMO->LUMO (56%), HOMO->L+1 (35%)	0.5545

Table 3.3. Select electronic transitions for **RuL2**$^{2+}$ calculated by TDDFT (>10% contribution threshold).

RuL3^{2+} $[Ru(bpy)_3(P\text{-}Qn\text{-}OQN)]^{2+}$

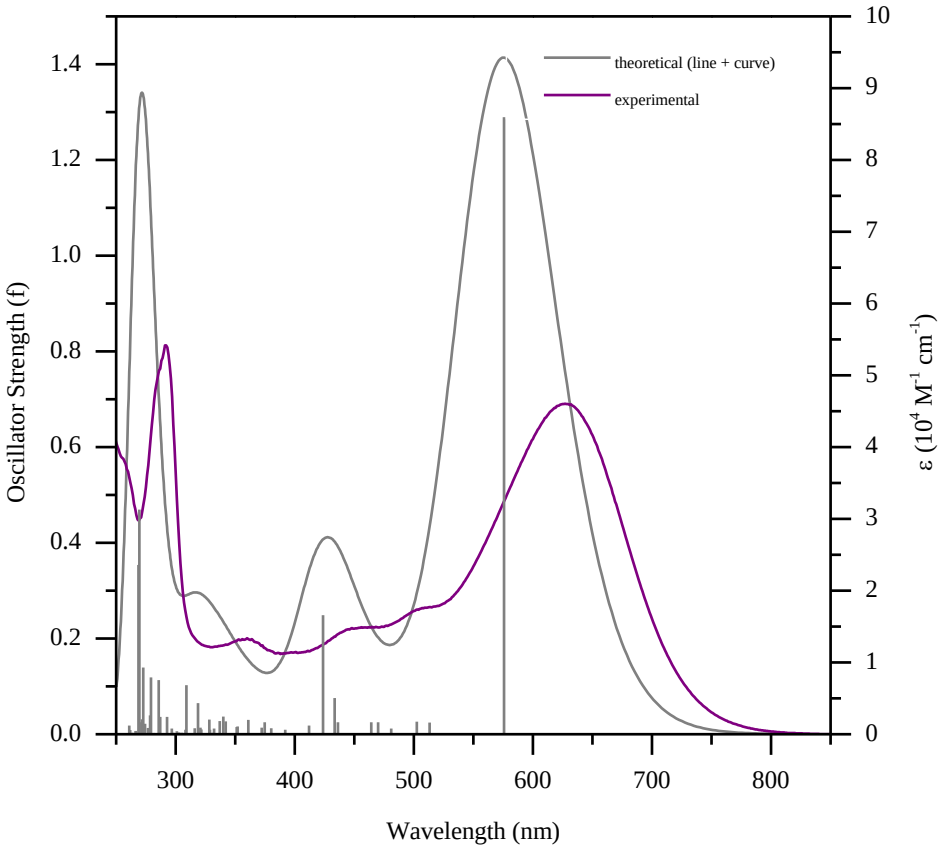

Figure A25. An overlay of experimental and theoretical spectra of **RuL3**$^{2+}$.

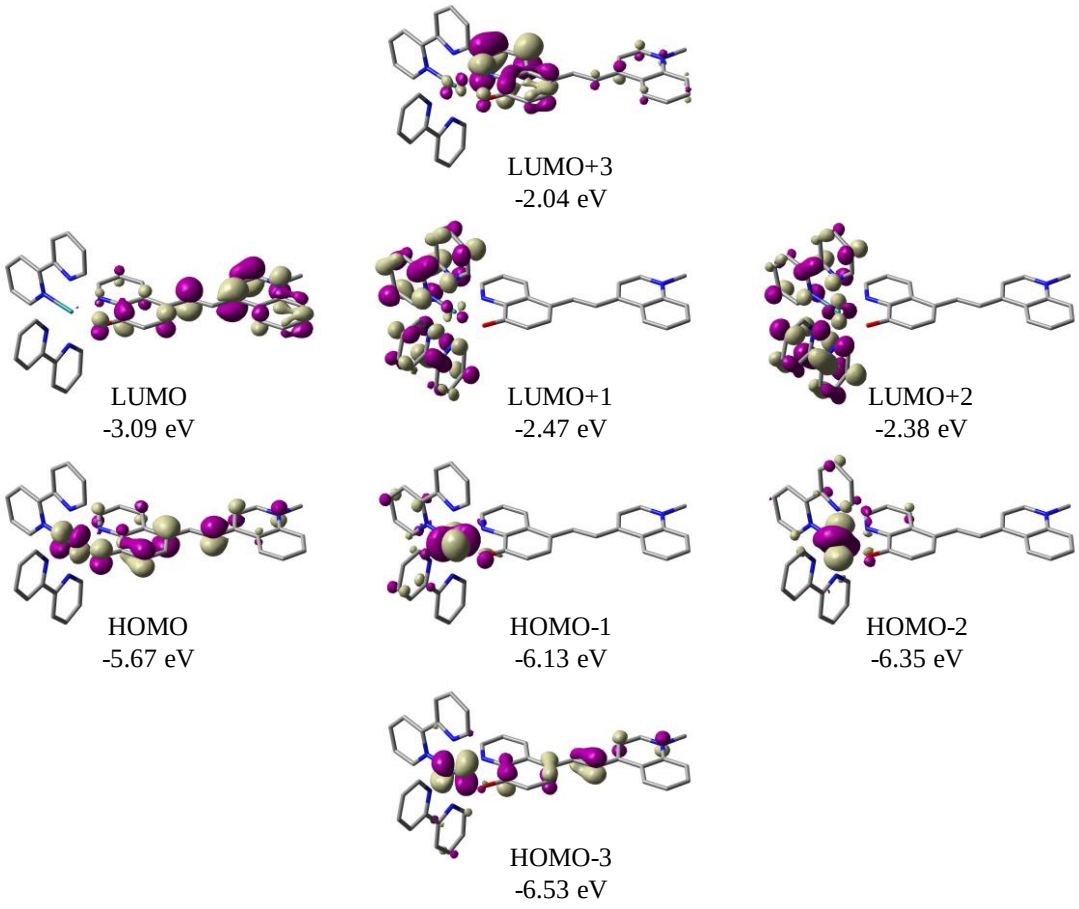

Figure A26. Selected molecular orbital surfaces (isofactor = 0.04) and energies for **RuL3**$^{2+}$.

Electronic Transition (nm)	MO Contributions (%)	Oscillator Strength (f)
270.0750139	H-3->L+8 (67%), H-3->L+9 (13%)	0.0323
271.0670033	H-3->L+10 (25%), H-2->L+9 (34%)	0.0293
273.2656028	H-6->L+1 (28%), H-5->L+2 (42%)	0.763
273.8450285	H-10->LUMO (81%)	0.0103
275.2982872	H-2->L+14 (31%), H-1->L+16 (12%)	0.03
275.7575157	H-6->L+2 (54%), H-5->L+2 (10%)	0.1847
277.808906	H-9->LUMO (13%), H-4->L+2 (55%), H-2->L+8 (19%)	0.0159
278.2453301	H-9->LUMO (11%), H-4->L+2 (29%), H-2->L+8 (38%)	0.0198
282.7442113	H-6->L+1 (32%), H-5->L+2 (17%), H-4->L+1 (36%)	0.0161
285.8141881	H-5->L+1 (33%), H-4->L+1 (14%), H-1->L+9 (10%)	0.0111

290.5428178	H-3->L+6 (37%), H-3->L+7 (30%)	0.0343
292.4549149	H-8->LUMO (71%)	0.0888
299.3176009	H-3->L+5 (76%)	0.0277
303.9626778	H-7->LUMO (23%), H-3->L+4 (20%)	0.029
316.8498253	H-5->LUMO (79%), HOMO->L+9 (12%)	0.0282
317.3689055	H-5->LUMO (12%), HOMO->L+9 (70%)	0.0733
320.0395886	H-2->L+6 (87%)	0.0159
328.0069225	HOMO->L+10 (63%)	0.0143
332.083398	H-2->L+5 (11%), H-1->L+7 (36%), H-1->L+14 (10%), HOMO->L+10 (10%)	0.0139
336.9020859	H-1->L+6 (68%), H-1->L+7 (13%)	0.0839
343.4631742	H-4->LUMO (86%)	0.0148
354.2178637	H-3->L+3 (53%), HOMO->L+7 (25%)	0.057
357.0331643	H-3->L+3 (30%), HOMO->L+7 (51%)	0.0227
360.5634172	HOMO->L+6 (71%), HOMO->L+7 (11%)	0.0114
366.727806	H-1->L+4 (91%)	0.0168
370.0995124	HOMO->L+5 (82%)	0.0111
379.3395442	H-2->L+3 (77%)	0.0283
394.7131153	H-3->L+1 (21%), H-3->L+2 (55%)	0.0274
400.7995624	H-3->L+1 (59%), H-3->L+2 (22%)	0.0162
432.0880206	H-2->L+1 (12%), H-2->L+2 (55%)	0.0157
447.2703342	H-3->LUMO (91%)	0.4158
456.2572188	H-2->L+1 (76%), H-2->L+2 (10%)	0.0852
490.4016163	H-2->L+2 (12%), H-1->L+1 (11%), H-1->L+2 (52%), HOMO->L+2 (14%)	0.0232
509.4856653	H-2->LUMO (15%), H-1->L+1 (61%), H-1->L+2 (13%)	0.019
510.8080778	H-2->LUMO (79%), H-1->L+1 (11%)	0.0239
535.7040124	H-1->L+2 (15%), HOMO->L+1 (22%), HOMO->L+2 (49%)	0.0323
547.9442111	HOMO->L+1 (55%), HOMO->L+2 (28%)	0.0133
563.9707817	H-1->LUMO (93%)	0.0707
605.2691693	HOMO->LUMO (91%)	1.0503

Table A4. Select electronic transitions for **RuL3**$^{2+}$ calculated by TDDFT (>10% contribution threshold).

RuL4^{2+} $[Ru(bpy)_2(O\text{-}Qn\_OQN)]^{2+}$

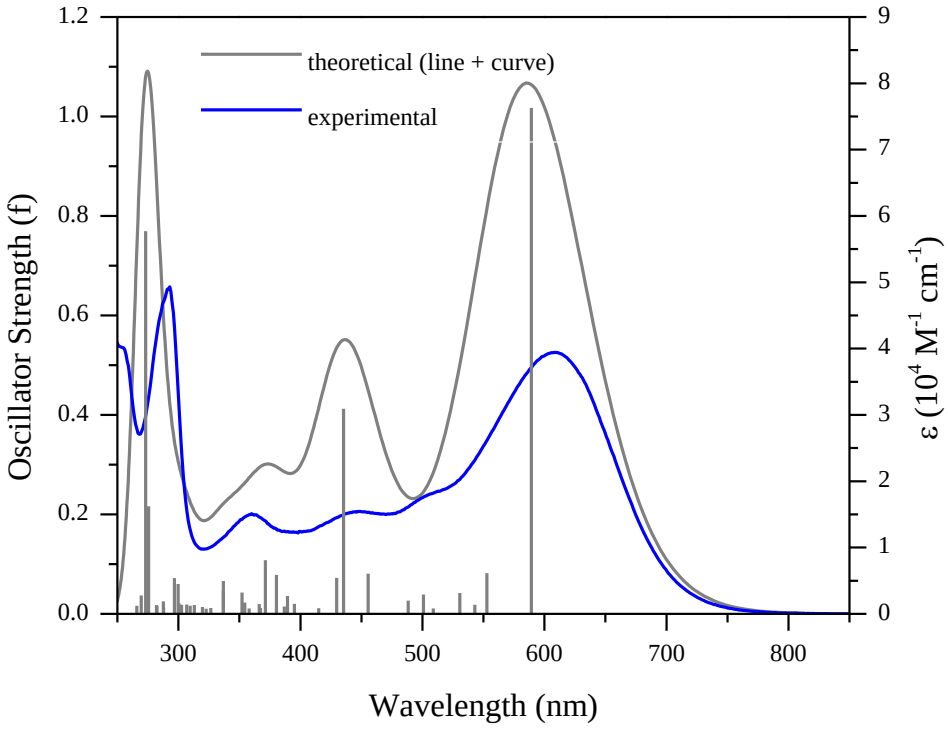

Figure A27. An overlay of experimental and theoretical spectra of **RuL4**$^{2+}$.

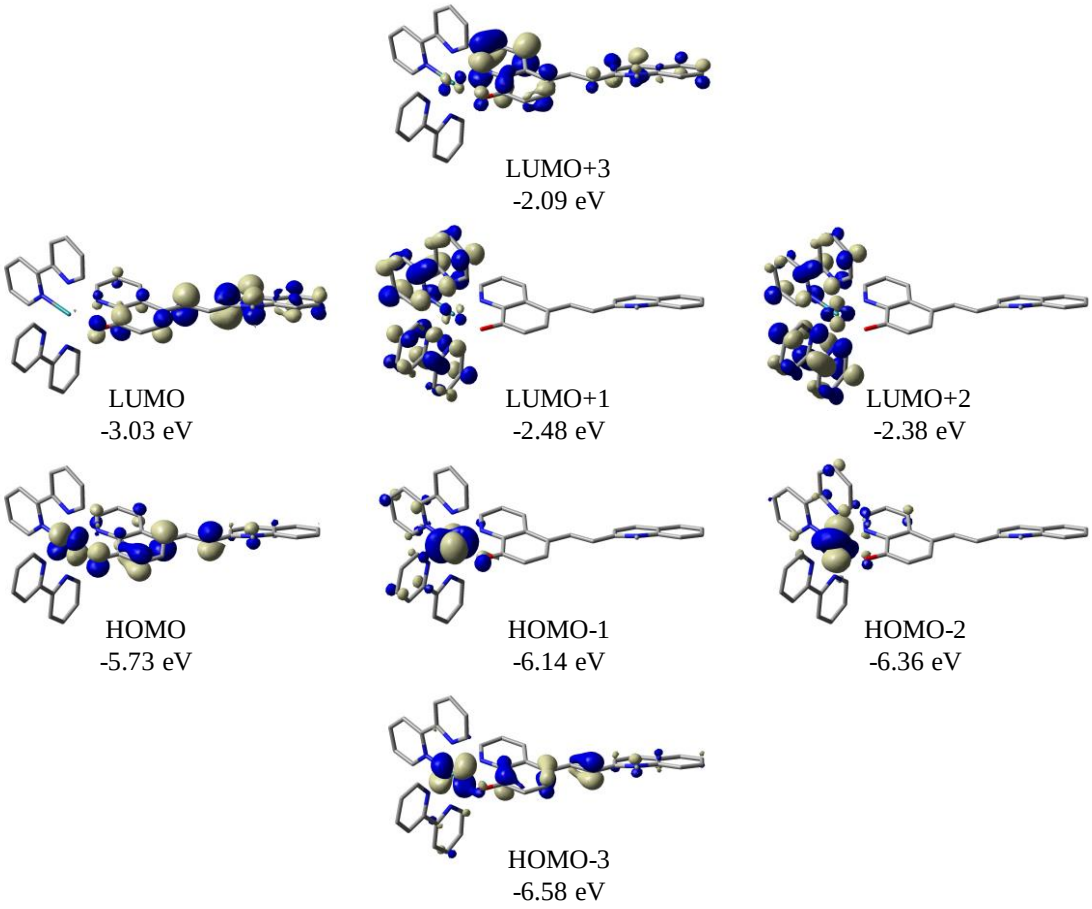

Figure A28. Selected molecular orbital surfaces (isofactor = 0.04) and energies for **RuL4**$^{2+}$.

Electronic Transition (nm)	**MO Contributions (%)**	**Oscillator Strength (f)**
265.9388186	H-8->L+1 (25%), H-7->L+1 (19%), H-3->L+9 (27%)	0.0161
269.4645555	H-7->L+1 (15%), H-4->L+2 (19%), H-3->L+9 (35%)	0.0367
273.2415133	H-6->L+1 (28%), H-5->L+2 (38%)	0.7693
275.3777772	H-6->L+2 (14%), H-2->L+14 (27%), H-1->L+16 (11%)	0.0347
275.6471612	H-6->L+2 (45%), H-5->L+2 (13%)	0.2165
281.9533274	HOMO->L+10 (73%)	0.0177

282.3707221	H-6->L+1 (49%), H-6->L+2 (21%), H-5->L+2 (13%)	0.0158
287.5842843	H-3->L+7 (15%), H-2->L+9 (48%)	0.0253
287.8246277	H-5->L+1 (10%), H-3->L+7 (32%), H-3->L+8 (23%)	0.0126
296.7386354	H-3->L+5 (28%), H-3->L+6 (47%)	0.0719
299.6793402	H-8->LUMO (57%)	0.0601
300.5219523	H-3->L+4 (11%), H-1->L+9 (17%)	0.0212
302.6789137	H-3->L+4 (12%), H-2->L+14 (11%), H-1->L+9 (19%)	0.0184
306.86666	H-8->LUMO (20%), H-7->LUMO (19%), H-1->L+9 (37%)	0.0188
309.540462	H-3->L+4 (30%), H-3->L+5 (16%), H-2->L+4 (10%), H-2->L+5 (25%)	0.0163
313.1445878	H-5->LUMO (74%)	0.0176
319.7589535	H-2->L+7 (88%)	0.0136
322.7808092	H-2->L+6 (18%), H-2->L+8 (58%)	0.0104
326.6157446	H-2->L+6 (11%), HOMO->L+9 (66%)	0.0117
336.8105638	H-4->LUMO (68%), H-1->L+7 (19%)	0.0658
336.8746241	H-4->LUMO (26%), H-1->L+7 (48%)	0.0475
352.1053523	H-3->L+3 (52%), H-1->L+6 (11%), HOMO->L+8 (22%)	0.0427
354.4609087	H-3->L+3 (28%), HOMO->L+7 (11%), HOMO->L+8 (51%)	0.0225
358.0435966	HOMO->L+7 (69%), HOMO->L+8 (12%)	0.0107
366.2511421	H-1->L+4 (45%), H-1->L+5 (34%), HOMO->L+6 (11%)	0.0197
367.173088	HOMO->L+6 (71%)	0.0116
371.2742907	HOMO->L+4 (25%), HOMO->L+5 (58%)	0.108
380.4453547	H-2->L+3 (63%)	0.0781
386.7710776	H-3->L+2 (32%), HOMO->L+4 (34%), HOMO->L+5 (17%)	0.0147
389.4315942	H-3->L+1 (18%), H-3->L+2 (39%), HOMO->L+4 (24%)	0.0359
395.0652794	H-3->L+1 (64%), H-3->L+2 (15%)	0.0204
415.0208765	H-1->L+3 (67%)	0.0114
429.6473529	H-3->LUMO (23%), H-2->L+2 (41%)	0.0726
435.4417752	H-3->LUMO (73%), H-2->L+2 (12%)	0.4123
455.5029084	H-2->L+1 (76%), H-2->L+2 (11%)	0.0807
488.2579319	H-2->L+2 (12%), H-1->L+1 (11%), H-1->L+2 (47%), HOMO->L+2 (16%)	0.0268
500.9022973	H-2->LUMO (92%)	0.0389
508.8165824	H-1->L+1 (68%), H-1->L+2 (19%)	0.0109

	H-1->L+1 (11%), H-1->L+2 (17%),	
530.7278654	HOMO->L+1 (21%), HOMO->L+2 (44%)	0.0421
542.9768619	HOMO->L+1 (52%), HOMO->L+2 (30%)	0.0183
552.8553315	H-1->LUMO (91%)	0.0816
589.3584477	HOMO->LUMO (89%)	1.0171

Table A5. Select electronic transitions for **RuL4**$^{2+}$ calculated by TDDFT (>10% contribution threshold).

RuL5^{2+} $[Ru(bpy)_2(IND\_OQN)]^{2+}$

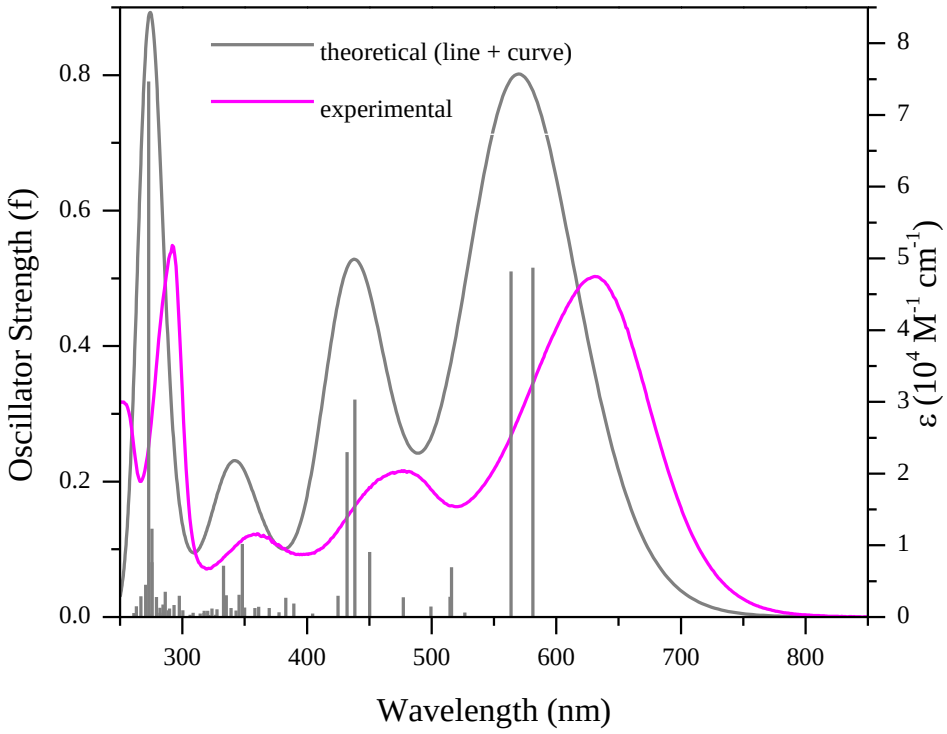

Figure A29. An overlay of experimental and theoretical spectra of **RuL5**$^{2+}$.

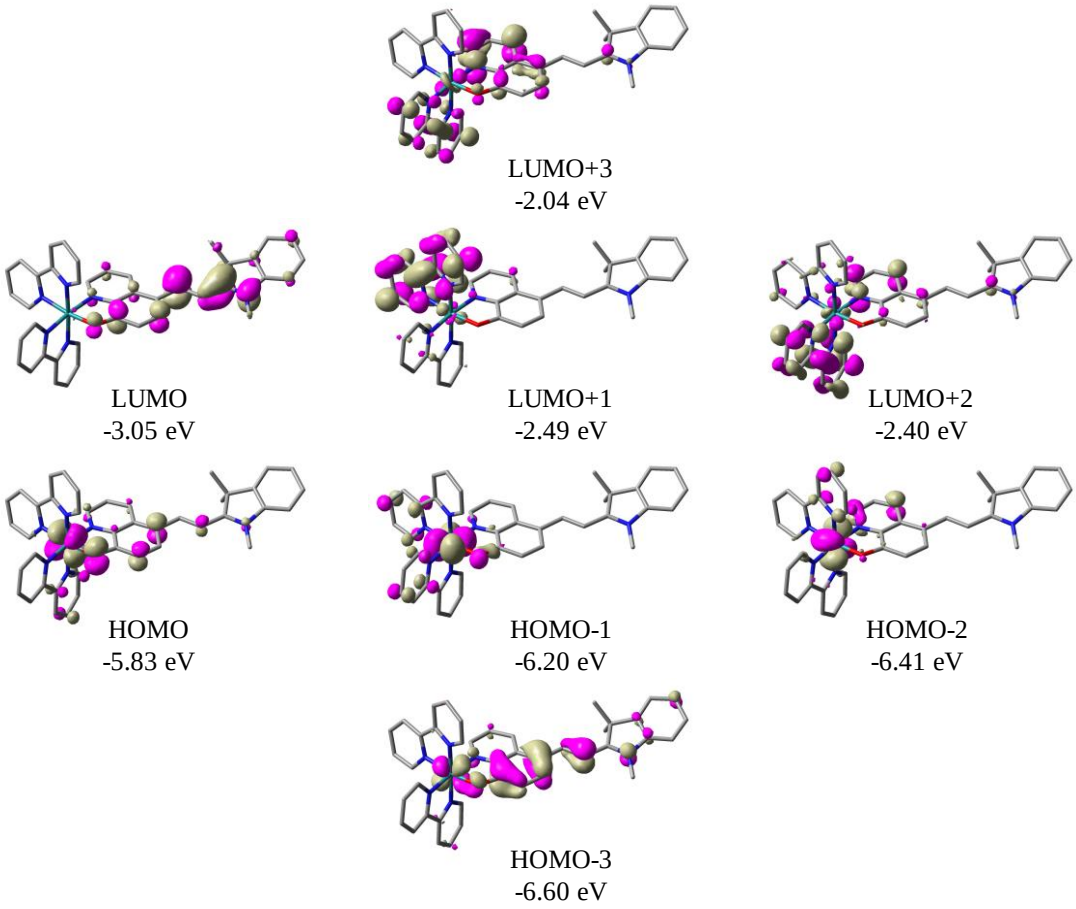

Figure A30. Selected molecular orbital surfaces (isofactor = 0.04) and energies for **RuL5**$^{2+}$.

Electronic Transition (nm)	MO Contributions (%)	Oscillator Strength (f)
263.089	HOMO->L+10 (68%)	0.0158
266.78	H-4->L+3 (22%), H-3->L+8 (51%)	0.0308
270.5465	H-4->L+3 (47%), H-3->L+8 (20%)	0.0478
273.0309	H-7->L+1 (28%), H-6->L+2 (38%)	0.7908
275.5185	H-7->L+2 (12%), H-2->L+12 (16%), H-2->L+13 (13%), H-1->L+14 (12%)	0.0836
275.5859	H-7->L+2 (46%)	0.1279
279.2606	HOMO->L+9 (91%)	0.0297

281.979	H-7->L+1 (22%), H-7->L+2 (13%), H-3->L+7 (17%)	0.0136
284.4829	H-7->L+1 (13%), H-6->L+2 (15%), H-4->L+2 (17%), H-3->L+6 (12%), H-3->L+7 (18%)	0.0185
286.3357	H-6->L+1 (44%), H-3->L+6 (35%)	0.0374
289.5927	H-4->L+1 (82%)	0.0126
293.41	H-3->L+5 (75%)	0.0178
297.5362	H-8->LUMO (21%), H-3->L+4 (25%)	0.0314
323.8347	H-2->L+5 (16%), HOMO->L+8 (61%)	0.0126
326.7104	H-5->LUMO (41%), H-4->LUMO (24%), H-2->L+5 (10%), H-1->L+7 (10%)	0.0033
327.7295	H-5->LUMO (21%), H-2->L+5 (23%), H-1->L+7 (25%)	0.0115
332.9305	H-1->L+6 (64%), H-1->L+7 (14%)	0.0755
335.1716	H-5->LUMO (29%), H-4->LUMO (64%)	0.032
339.0487	H-2->L+4 (76%), H-1->L+6 (10%)	0.0132
345.4826	H-1->L+5 (27%), HOMO->L+7 (47%)	0.033
348.1309	H-3->L+3 (76%)	0.1079
349.8796	HOMO->L+6 (60%), HOMO->L+7 (15%)	0.0141
358.2298	HOMO->L+5 (75%)	0.0134
361.2779	H-1->L+4 (85%)	0.0153
369.6802	H-2->L+3 (73%)	0.0134
382.9601	H-3->L+2 (72%)	0.0286
389.4316	H-3->L+1 (72%)	0.0199
424.8769	H-2->L+1 (12%), H-2->L+2 (55%), H-1->L+2 (10%)	0.0315
432.1784	H-3->LUMO (10%), H-1->L+3 (10%), HOMO->L+3 (70%)	0.2435
438.4135	H-3->LUMO (79%), HOMO->L+3 (14%)	0.3208
450.3408	H-2->L+1 (75%), H-2->L+2 (10%)	0.0961
477.171	H-2->L+2 (16%), H-1->L+2 (37%), HOMO->L+2 (20%)	0.0292
499.4092	H-1->L+1 (61%), H-1->L+2 (21%), HOMO->L+1 (12%)	0.0155
514.6459	H-2->LUMO (75%), HOMO->L+2 (14%)	0.0303
515.9094	H-2->LUMO (11%), H-1->L+1 (18%), H-1->L+2 (17%), HOMO->L+1 (18%), HOMO->L+2 (29%)	0.0734
563.6375	H-1->LUMO (61%), HOMO->LUMO (31%)	0.5101
581.2627	H-1->LUMO (34%), HOMO->LUMO (58%)	0.5161

Table A6. Select electronic transitions for **RuL5**$^{2+}$ calculated by TDDFT (>10% contribution threshold).

RuL6^{2+} $[Ru(bpy)_2(BIN\_OQN)]^{2+}$

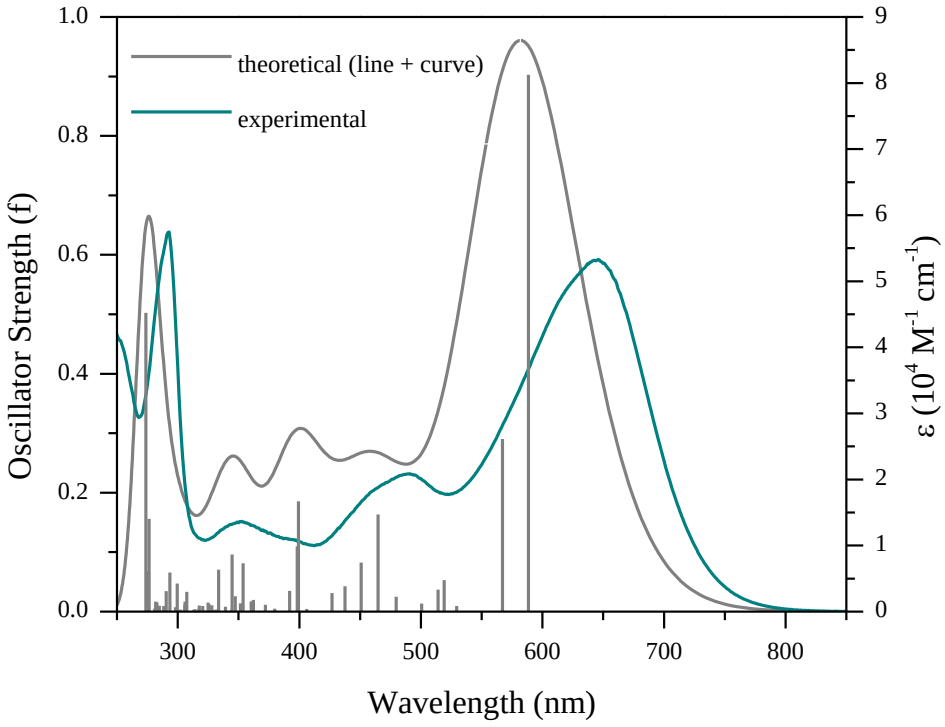

Figure A31. An overlay of experimental and theoretical spectra of **RuL6**$^{2+}$.

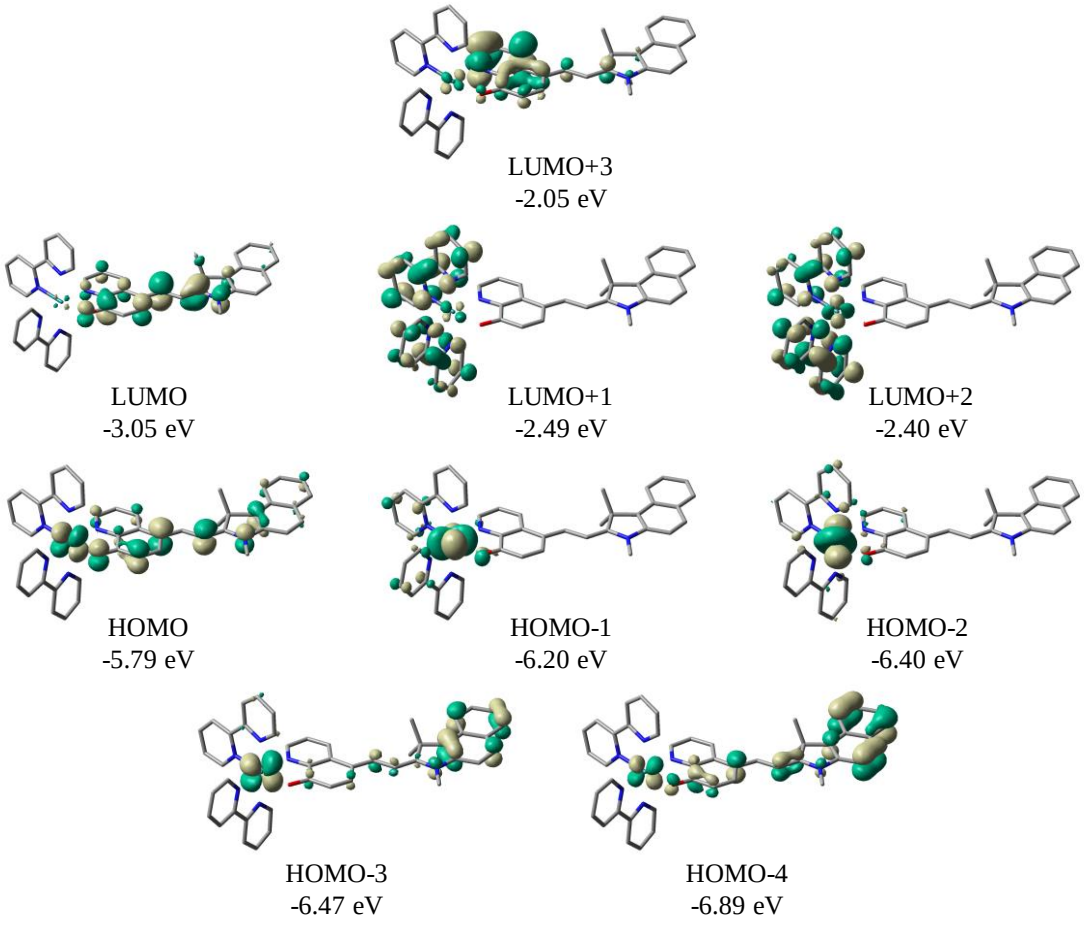

Figure A32. Selected molecular orbital surfaces (isofactor = 0.04) and energies for **RuL6**$^{2+}$.

Electronic Transition (nm)	**MO Contributions (%)**	**Oscillator Strength (f)**
273.7181	H-11->LUMO (20%), H-7->L+1 (20%), H-6->L+2 (26%)	0.5026
274.9442	H-11->LUMO (28%), H-9->LUMO (48%)	0.0269
275.9294	H-2->L+13 (13%), H-2->L+14 (15%), H-1->L+15 (13%)	0.0679
276.3045	H-7->L+2 (47%)	0.156
281.7483	H-5->L+2 (51%), HOMO->L+10 (18%)	0.017

282.8926	H-7->L+1 (28%), H-7->L+2 (13%), H-6->L+1 (11%)	0.0158
290.5224	H-3->L+7 (43%), H-2->L+5 (14%)	0.0345
293.5698	H-3->L+5 (49%), H-2->L+5 (38%)	0.0657
298.2448	H-3->L+6 (46%), H-2->L+6 (12%)	0.0073
299.5273	H-8->LUMO (41%), H-3->L+6 (15%)	0.0473
305.7316	H-4->L+3 (14%), H-1->L+5 (79%)	0.012
305.9957	H-4->L+3 (42%), H-1->L+5 (12%), H-1->L+9 (32%)	0.017
307.445	H-8->LUMO (14%), H-4->L+3 (19%), H-1->L+9 (31%)	0.0333
317.6291	H-2->L+7 (79%)	0.0103
324.9465	H-2->L+6 (10%), HOMO->L+9 (61%)	0.0152
325.6549	H-4->L+2 (75%)	0.0125
327.9028	H-2->L+6 (28%), H-1->L+8 (35%)	0.0106
333.7012	H-1->L+7 (64%)	0.0706
344.7046	HOMO->L+5 (86%)	0.096
347.2728	H-1->L+6 (11%), HOMO->L+7 (11%), HOMO->L+8 (61%)	0.0259
351.5463	HOMO->L+7 (63%), HOMO->L+8 (12%)	0.0139
353.8034	H-3->L+3 (69%)	0.0814
360.4272	HOMO->L+6 (69%)	0.0171
362.2807	H-1->L+4 (83%)	0.0199
372.1659	H-2->L+3 (77%)	0.0114
391.9926	H-3->L+2 (52%), H-2->L+2 (12%)	0.0349
398.3144	H-4->LUMO (20%), H-3->L+1 (43%), H-3->L+2 (11%)	0.1098
399.3022	H-4->LUMO (72%), H-3->L+1 (13%)	0.1855
426.8076	H-2->L+1 (14%), H-2->L+2 (51%)	0.0311
437.6243	HOMO->L+3 (84%)	0.0425
450.8977	H-2->L+1 (71%)	0.0826
464.862	H-3->LUMO (93%)	0.1634
479.6632	H-1->L+2 (40%), HOMO->L+2 (20%)	0.0252
500.6798	H-1->L+1 (61%), H-1->L+2 (19%), HOMO->L+1 (12%)	0.0136
514.219	H-2->LUMO (84%)	0.037
519.1715	H-1->L+1 (16%), H-1->L+2 (21%), HOMO->L+1 (16%), HOMO->L+2 (37%)	0.0528
567.1699	H-1->LUMO (82%), HOMO->LUMO (12%)	0.2904
588.5751	H-1->LUMO (13%), HOMO->LUMO (79%)	0.9028

Table A7. Select electronic transitions for **RuL7**$^{2+}$ calculated by TDDFT (>10% contribution threshold).

REFERENCE LIST

(1) A. Juris, V. Balzani, F. Barigelletti, S. Campagna, P. Belser and A. von Zelewsky, Coord. Chem. Rev., 1988, 84, 85–277.

(2) Agarwal, J.; Shaw, T.; Stanton, C.; Majetich, G.; Bocarsly, A.; Schaefer, H. NHC-Containing Manganese(I) Electrocatalysts for the Two-Electron Reduction of CO_2. Angew. Chem. Int. Ed. 2014, 53, 5152 –5155.

(3) Anderson, T.; Hawkins, E.; Jones, P. CO_2, the greenhouse effect and global warming: from the pioneering work of Arrhenius and Callendar to today's Earth System Models. Endeavour Vol. 40 No.3, 178-187.

(4) Andrieux, C. P.; Blocman, C.; Dumas-Bouchiat, J. M.; M'Halla, F.; Saveant, J. M. Homogeneous redox catalysis of electrochemical reactions: Part V. Cyclic voltammetry. J. Electroanal. Chem. Interfacial Electrochem. 1980, 113, 19−40.

(5) Anslyn, E.; Dougherty, D. A. Modern Physical Organic Chemistry; University Science Books, 2006, p 455.

(6) Appel, A.; Helm, M. Determining the Overpotential for a Molecular Electrocatalyst, Acs Catalysis 2014, 4 (2), 630-633.

(7) Atkins, P.; De Paula, J. Atkin's Physical Chemistry. 2006, 8th edition.

(8) Azcarate, I.; Costentin, C.; Robert, M.; Savéant, J.; Through-Space Charge Interaction Substituent Effects in Molecular Catalysis Leading to the Design of the Most Efficient Catalyst of CO_2-to-CO Electrochemical Conversion. J. Am. Chem. Soc. 2016, 138, 16639−16644.

(9) Bellinger-Buckley, S.; Chang, T.; Bag, S.; Schweinfurth, D.; Zhou, W.; Torok, B.; Sarkar, B.; Tsai, M.; Rochford, J. *Inorg. Chem.* **2014**, *53*, 5556-5567.

(10) Benson, E. E.; Kubiak, C. P.; Sathrum, A. J.; Smieja, J. M. Electrocatalytic and homogeneous approaches to conversion of CO_2 to liquid fuels. Chem. Soc. Rev. 2009, 38 (1), 89−99.

(11) Benson, E. E.; Kubiak, C. P.; Sathrum, A. J.; Smieja, J. M. Electrocatalytic and homogeneous approaches to conversion of CO2 to liquid fuels. Chem. Soc. Rev. 2009, 38,89−99.

(12) Bhugun, I.; Lexa, D.; Savéant, J.-M. Catalysis of the Electrochemical Reduction of Carbon Dioxide by Iron(0) Porphyrins. Synergistic Effect of Lewis Acid Cations. J. Phys. Chem. 1996, 100, 19981−19985.

(13) Bhugun, I.; Lexa, D.; Savéant, J.-M. Catalysis of the Electrochemical Reduction of Carbon Dioxide by Iron(0) Porphyrins: Synergystic Effect of Weak Brønsted Acids. J. Am. Chem. Soc. 1996, 118, 1769−1776.

(14) Bhugun, I.; Lexa, D.; Savéant, J.-M. Ultraefficient selective homogeneous catalysis of the electrochemical reduction of carbon dioxide by an iron(0) porphyrin associated with a weak Brønsted acid cocatalyst. J. Am. Chem. Soc. 1994, 116, 5015−5016.

(15) Boyer, J. L.; Rochford, J.; Tsai, M. K.; Muckerman, J. T.; Fujita, E. *Coord. Chem. Rev.* **2010**, *254*, 309-330.

(16) Broere, D. L. J.; Plessius, R.; van der Vlugt, J. I. *Chem. Soc. Rev.* **2015**, *44*, 6886-6915.

(17) Browne, W. R.; Passaniti, P.; Gandolfi, M. T.; Ballardini, R.; Henry, W.; Guckian, A.; O'Boyle, N.; McGarvey, J. J.; Vos, J. G. *Inorg. Chim. Acta* **2007**, *360*, 1183−1190.

(18) Caspar, J. V.; Meyer, T. J. *J. Phys. Chem.* **1983**, *87*, 952-957.

(19) Collman, J.; Brauman, J.; Halbert, T.; Suslick, K. Nature of O_2 and CO binding to metalloporphyrins and heme proteins. Proc Natl Acad Sci U S A. 1976 Oct; 73(10): 3333–3337.

(20) Cometto, C.; Chen, L.; Lo, P.; Guo, Z.; Lau, K.; Anxolabéhère-Mallart, E.; Fave, C.; Lau, T.; Robert, M. Highly Selective Molecular Catalysts for the CO2-to-CO Electrochemical Conversion at Very Low Overpotential. Contrasting Fe vs Co Quaterpyridine Complexes upon Mechanistic Studies. ACS Catal. 2018, 8, 3411−3417.

(21) Costentin, C.; Drouet, S.; Passard, G.; Robert, M.; Savéant, J. Proton-Coupled Electron Transfer Cleavage of Heavy-Atom Bonds in Electrocatalytic Processes. Cleavage of a C−O Bond in the Catalyzed Electrochemical Reduction of CO_2. J. Am. Chem. Soc. 2013, 135, 9023−9031.

(22) Costentin, C.; Drouet, S.; Robert, M.; Savéant, J.-M. A local proton source enhances CO_2 electroreduction to CO by a molecular Fe catalyst. Science 2012, 338,90−94.

(23) Costentin, C.; Passard, G.; Robert, M.; Savéant, J.-M. Pendant acid-base groups in molecular catalysts: H-bond promoters or proton relays? Mechanisms of the conversion of CO2 to CO by electro- generated iron(0)porphyrins bearing prepositioned phenol function- alities. J. Am. Chem. Soc. 2014, 136, 11821−11829.

(24) Cyrille, Costentin; J.-M. Savéant. Multielectron, Multistep Molecular Catalysis of Electrochemical Reactions: Benchmarking of Homogeneous Catalysts, ChemElectroChem 2014, 1 (7), 1226-1236.

(25) Damrauer, N. H.; Cerullo, G.; Yeh, A.; Boussie, T. R.; Shank, C. V.; McCusker, J. K. *Science* **1997**, *275*, 54-57.

(26) Daskalakis, V.; Varotsis, C. Binding and Docking Interactions of NO, CO and O_2 in Heme Proteins as Probed by Density Functional Theory. Int J Mol Sci. 2009 Sep; 10(9): 4137–4156. Published online 2009 Sep 22.

(27) Daul, C.; Baerends, E. J.; Vernooijs, P. *Inorg. Chem.* **1994**, *33*, 3538-3543.

(28) Deißler, C.; Rominger, F.; Kunz, D. Controlling the coordination modes of a new and highly flexible ligand bearing two N-heterocyclic carbene moieties at a bipyridine backbone. Dalton Trans., 2009, 7152–7167.

(29) E. S. Rountree; B. D. McCarthy; T. T. Eisenhart; J. L. Dempsey. Evaluation of Homogeneous Electrocatalysts by Cyclic Voltammetry, Inorganic Chemistry 2014, 53 (19), 9983-10002.

(30) Faller, J. W.; Mueller, A.; Phillips, J. P. *Notes* **1964**, *29*, 3450-3452.

(31) Francke, R.; Little, R. D. Redox catalysis in organic electrosynthesis: basic principles and recent developments. Chem. Soc. Rev. 2014, 43, 2492−2521.

(32) Francke, R.; Schille, B.; Roemelt, M. Homogeneously Catalyzed Electroreduction of Carbon Dioxide: Methods, Mechanisms, and Catalysts. Chem. Rev. 2018, 118, 4631−4701.

(33) Francl, M. M.; Pietro, W. J.; Hehre, W. J.; Binkley, J. S.; Gordon, M. S.; Defrees, D. J.; Pople, J. A. *J. Chem. Phys.* **1982**, *77*, 3654−3665.

(34) Fredin, L. A.; Allison, T. C. *J. Phys. Chem. A* 2016, 120, 13, 2135–2143.

(35) Frisch, M. J.; et al. *Gaussian 09, Revision A.1*; Gaussian Inc.: Wallingford, CT, 2009.

(36) Fulmer, G. R.; Miller, A. J. M.; Sherden, N. H.; Gottlieb, H. E.; Nudelman, A.; Stoltz, B. M.; Bercaw, J. E.; Goldberg, K. I. *Organometallics*, **2010**, *29*, 2176-2179.

(37) Genovese, C.; Ampelli, C.; Perathoner, S.; Centi, G. Electro- catalytic conversion of CO_2 to liquid fuels using nanocarbon-based electrodes. J. Energy Chem. 2013, 22, 202−213.

(38) Grills, D. C.; Matsubara, Y.; Kuwahara, Y.; Golisz, S. R.; Kurtz, D. A.; Mello, B. A. Electrocatalytic CO_2 Reduction with a Homogeneous Catalyst in Ionic Liquid: High Catalytic Activity at Low Overpotential. J. Phys. Chem. Lett. 2014, 5, 2033−2038.

(39) H.A. Schwarz, R.W. Dodson. Reduction potentials of CO_2^- and the alcohol radicals. J. Phys. Chem., 93 (1989), pp. 409-414.

(40) Hammouche, M.; Lexa, D.; Momenteau, M.; Savéant, J. M. Chemical catalysis of electrochemical reactions. Homogeneous catalysis of the electrochemical reduction of carbon dioxide by iron(″0″) porphyrins. Role of the addition of magnesium cations. J. Am. Chem. Soc. 1991, 113, 8455−8466.

(41) Hammouche, M.; Lexa, D.; Savéant, J. M.; Momenteau, M. Catalysis of the electrochemical reduction of carbon dioxide by iron("0") porphyrins. J. Electroanal. Chem. Interfacial Electrochem. 1988, 249, 347−351.

(42) Hansch, C.; Leo, A.; Taft, W. A Survey of Hammett Substituent Constants and Resonance and Field Parameters. Chem. Rev. 1991 (2): 165–195.

(43) Harihara, Pc; Pople, J. A. *Theor. Chim. Acta* **1973**, *28*, 213−222.

(44) Hu, K.; Severin, H. A.; Koivisto, B. D.; Robson, K. C. D.; Schott, E.; Arratia-Perez, R.; Meyer, G. J.; Berlinguette, C. P. *J. Phys. Chem. C* **2014**, *118*, 17079−17089.

(45) Ingram, J. D.; Costa, P. J.; Adams, H.; Ward, M. D.; Felix, V.; Thomas, J. A. *Inorg. Chem.* **2012**, *51*, 10483-10494.

(46) Ito, M.; Matsumura, K. *Notes* **1958**, *23*, 86-88.

(47) Juris, A.; Balzani, V.; Barigelletti, F.; Campagna, S.; Belser, P.; Vonzelewsky, A. *Coord. Chem. Rev.* **1988**, *84*, 85-277.

(48) K. Aasberg-Petersen, I. Dybkjaer, C.V. Ovesen, N.C. Schjodt, J. Sehested, S.G. Thomsen. Natural gas to synthesis gas - Catalysts and catalytic processes. J. Nat. Gas Sci. Eng., 3 (2011), pp. 423-459.

(49) Kaim, W. *Eur. J. Inorg. Chem.* **2012**, *2012*, 343-348.

(50) Kaim, W. *Inorg. Chem.* **2011**, *50*, 9752-9765.

(51) Kober, E. M.; Meyer, T. J. *Inorg. Chem.* **1982**, *21*, 3967-3977.

(52) Kovtun, Y. P.; Prostota, Y. O.; Tolmachev, A. I. *Dyes and Pigments* **2003**, *58*, 83-91.

(53) Laine, T. M.; Karkas, M. D.; Liao, R.-Z.; Siegbahn, P. E. M.; Akermark, B. *Chem. - Eur. J.* **2015**, *21*, 10039−10048.

(54) Li, Y.; Chan, S. H.; Sun, Q. Heterogeneous catalytic conversion of CO_2: a comprehensive theoretical review. Nanoscale 2015, 7, 8663− 8683.

(55) Luca, O. R.; Crabtree, R. H. *Chem. Soc. Rev.* **2013**, *42*, 1440-1459.

(56) Mandal, A.; Grupp, A.; Schwederski, B.; Kaim, W.; Lahiri, G. K. *Inorg. Chem*. **2015**, *54*, 10049−10057.

(57) Matsubara, Y.; Grills, D.; Kuwahara Y. Thermodynamic Aspects of Electrocatalytic CO_2 Reduction in Acetonitrile and with an Ionic Liquid as Solvent or Electrolyte. ACS Catal. 2015, 5, 6440−6452.

(58) Ngo, K. T.; Lee, N. A.; Pinnace, S. D.; Szalda, D. J.; Weber, R. T.; Rochford, J. *Inorg. Chem.* **2016**, *55*, 2460-2472.

(59) Ngo, K.; McKinnon, M.; Mahanti, B.; Narayanan, R.; Grills, D.; Ertem, M.; Rochford, J. Turning on the Protonation-First Pathway for Electrocatalytic CO_2 Reduction by Manganese Bipyridyl Tricarbonyl Complexes. J. Am. Chem. Soc. 2017, 139, 2604−2618.

(60) O'Donnell, R. M.; Johannson, P. G.; Abrahamsson, M.; Meyer, G. J. *Inorg. Chem.* **2013**, *52*, 6839-6848.

(61) P. Lahijani, Z.A. Zainal, M. Mohammadi, A.R. Mohamed. Conversion of the greenhouse gas CO_2 to the fuel gas CO via the Boudouard reaction: A review. Renew. Sus. Energ. Rev., 41 (2015), pp. 615-632.

(62) Philips, J. J.; Hudspeth, M. A.; Browne, P. M., Jr.; Peralta, J. E. *Chem. Phys. Lett.* **2010**, *495*, 146−150.

(63) Q.H. Zhang, J.C. Kang, Y. Wang. Development of Novel Catalysts for Fischer-Tropsch Synthesis: Tuning the Product Selectivity. Chem. Cat. Chem., 2 (2010), pp. 1030-1058.

(64) Qiao, J.; Liu, Y.; Hong, F.; Zhang, J. A review of catalysts for the electroreduction of carbon dioxide to produce low-carbon fuels. Chem. Soc. Rev. 2014, 43, 631−675.

(65) Riplinger, C.; Carter, E. Influence of Weak Brønsted Acids on Electrocatalytic CO_2 Reduction by Manganese and Rhenium Bipyridine Catalysts. ACS Catal. 2015, 5, 2, 900-908.

(66) Rountree, E. S.; McCarthy, B. D.; Eisenhart, T. T.; Dempsey, J. L. Evaluation of homogeneous electrocatalysts by cyclic voltammetry. Inorg. Chem. 2014, 53, 9983−10002.

(67) Sampson, M.; Nguyen, A.; Grice, K.; Moore, C.; Rheingold, A.; Kubiak, C. Manganese Catalysts with Bulky Bipyridine Ligands for the Electrocatalytic Reduction of Carbon Dioxide: Eliminating Dimerization and Altering Catalysis. J. Am. Chem. Soc. 2014, 136, 14, 5460-5471.

(68) Scalmani, G.; Frisch, M. J.; Mennucci, B.; Tomasi, J.; Cammi, R.; Barone, V. *J. Chem. Phys*. **2006**, *124*, 94107.

(69) Senftle, T. P.; Carter, E. A. The Holy Grail: Chemistry Enabling an Economically Viable CO_2 Capture, Utilization, and Storage Strategy. Acc. Chem. Res. 2017, 50 (3), 472−475.

(70) Stanton, C.; Vandezande, J.; Majetich, G.; Schaefer, H.; Agarwal, J. Mn-NHC Electrocatalysts: Increasing π Acidity Lowers the Reduction Potential and Increases the Turnover Frequency for CO_2 Reduction. Inorg. Chem. 2016, 55, 9509−9512.

(71) Sullivan, B. P.; Salmon, D. J.; Meyer, T. J. *Inorg. Chem.* **1978**, *17*, 3334−3341.

(72) Tomasi, J.; Mennucci, B.; Cammi, R. *Chem. Rev*. **2005**, *105*, 2999−3093.

(73) Tomasulo, M.; Sortino, S.; Raymo, M. *J. Org. Chem.* **2008**, *73*, 118-126.

(74) Weisser, F.; Plebst, S.; Hohloch, S.; van der Meer, M.; Manck, S.; Führer, F.; Radtke, V.; Leichnitz, D.; Sarkar, B. *Inorg. Chem*. **2015**, *54*, 4621−4635.

(75) Whipple, D. T.; Kenis, P. J. A. Prospects of CO_2 Utilization via Direct Heterogeneous Electrochemical Reduction. J. Phys. Chem. Lett. 2010, 1, 3451−3458.

(76) Y. Matsubara; D. C. Grills; Y. Kuwahara. Thermodynamic Aspects of Electrocatalytic CO2 Reduction in Acetonitrile and with an Ionic Liquid as Solvent or Electrolyte, Acs Catalysis 2015, 6440-6452.

(77) Zhang, Y.; Zhou, Q.; Tian, N.; Li, C.; Wang, X. *Inorg. Chem.* **2017**, *56*, 4, 1865-1873.

(78) Zhao, H. C.; Fu, B.-L.; Schweinfurth, D.; Harney, J. P.; Sarkar, B.; Tsai, M.-K.; Rochford, J. *Eur. J. Inorg. Chem.* **2013**, *2013*, 4410−4420.